NASA CR-54182
HRL-5249-S

ELECTRODE SURFACE PHYSICS RESEARCH

by

R. G. Wilson

prepared for

NATIONAL AERONAUTICS AND SPACE ADMINISTRATION

CONTRACT NAS 3-5249

HUGHES RESEARCH LABORATORIES

Requests for copies of this report should be referred to

National Aeronautics and Space Administration
Office of Scientific and Technical Information
Attention: AFSS-A
Washington, D.C. 20546

CASE FILE
COPY

SUMMARY REPORT

ELECTRODE SURFACE PHYSICS RESEARCH

by

R. G. Wilson

prepared for

NATIONAL AERONAUTICS AND SPACE ADMINISTRATION

Date submitted 12 January 1965

Date approved 28 June 1965

CONTRACT NAS 3-5249

Technical Management
NASA-Lewis Research Center
Cleveland, Ohio
Spacecraft Technology Division
Y. E. Strausser

HUGHES RESEARCH LABORATORIES
a division of hughes aircraft company
3011 Malibu Canyon Road
Malibu, California

TABLE OF CONTENTS

LIST OF ILLUSTRATIONS

vi

ABSTRACT

The metallic elements are analyzed by certain criteria to deter-
mine their relative potentials as electrode materials in a device subject
to an arrival flux of cesium atoms, high surface electric fields, moder-
ately high temperatures, and energetic cesium ion bombardment. Ana-
lytical digital computer calculations are used to determine equilibrium
surface coverages as a function of temperature, arrival flux, and ad-
sorbate and substrate species; of composite surface work function and
atom and ion desorption energies as functions of surface coverage and
adsorbate and substrate species combination; of cesium ion critical
temperatures; and of cesium surface ionization efficiencies (neutral
fractions). An experimental tube design, a vacuum system, and ex-
perimental techniques for studying electron and ion emission from cesi-
ated nonrefractory and refractory metals, semiconductors, and insula-
tors are described. The techniques include fast automated data
collection of electron and ion emission currents versus surface tem-
perature. Emitters and collectors are fabricated from the same high
purity materials. Normal electric and magnetic fields are applied.
Very low background currents are obtained. A bakeable, all glass,
sorption roughed and ion pumped vacuum system was employed, result-
ing in a clean vacuum environment of 10^{-9} Torr, exclusive of cesium
and the vapor pressure of the heated emitters. Experimental measure-
ments of effective vacuum work functions, cesium surface ionization
current densities and critical temperatures, cesium ion desorption
energies (at low coverage), cesiated electron emission S curves and
cesiated work functions, the influence of applied surface electric fields,
contamination, and temperature, and time hystereses effects were made
for molybdenum, molybdenum silicide, copper, iron, chromium, alu-
minum oxide, and tantalum boride.

SECTION I

INTRODUCTION

A major goal of this research contact was to provide information necessary for the proper choice of materials from which to fabricate electrodes for long-life, efficient cesium contact ion engines. The analytical and experimental data obtained in this research program concerning the electron and ion emission characteristics of cesiated metals, semiconductors, and insulators yield data of fundamental value to other scientific and engineering fields; for example, in thermionic energy conversion. The particular problem, as applied to the cesium contact ion thrustor, involves essentially a plane parallel diode with high surface electric fields in the presence of a low pressure cesium environment. The cathode corresponds to the thrustor accelerating electrodes, and the anode to the thrustor focusing electrodes and ionizers. The focusing electrodes may be independent structures or may be portions of a large continuous ionizer. The focus electrodes should be poor cesium ionizers; the ionizer should be a good cesium ionizer. This geometry is illustrated in the simplified schematic sketch of Fig. 1. A cesium pressure of 10^{-5} to 10^{-4} Torr results from evaporation of neutral cesium from the porous ionizers. Electron emission from the accel electrodes can cause local heating of the focus and ionizer electrodes and a wasted power drain. Ion emission from the focus electrodes causes serious erosion of the accel electrodes and power drains. Complete erosion or associated melting of the accel electrodes (or runaway interelectrode drain currents) is the life-limiting factor in long term operation of cesium contact ion thrustors.

Charge-exchange ions from the ion beam and ionization on the focus electrode surfaces cause the accel electrode material to sputter back onto the focus electrodes and ionizers; therefore, the

CESIUM ION BEAMS

DECEL

−ACCEL

E

+FOCUS

POROUS TUNGSTEN IONIZERS
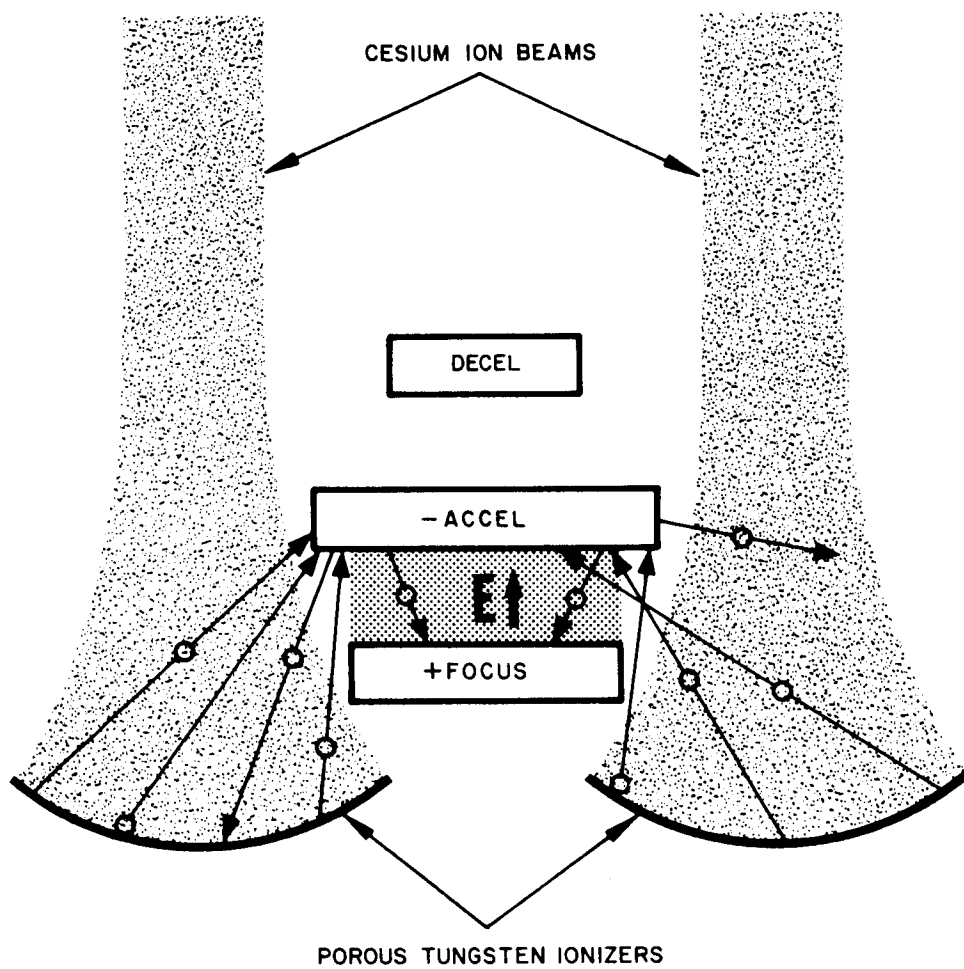
Fig. 1. Ion thrustor electrode schematic.

possibility of a composite or changing focus electrode (and ionizer) surface must be considered. An experimental tube which simulates the plane parallel electrode geometry of the thrustor was designed for these studies. For high-energy cesium ion emission studies, the collector surfaces were made of the same material as the emitter, so that the nature and composition of the emitter could not change because of the sputtering of the collector surface back onto the emitter. The sputtering of the accel electrode material back onto the ionizer results in the requirement of a low desorption energy for the electrode material from the ionizer. Therefore, the refractory materials are not good candidates. This introduces the problem of studying electron and ion emission from nonrefractory cesiated metals, which is a new area of experimental investigation. Somewhat different techniques were developed for these studies with low-melting-point materials. The surfaces for which experimental information is reported are copper, beryllium, molybdenum, chromium, iron, molybdenum silicide, tantalum boride, and aluminum oxide. Cesiated emission data are reported for all but beryllium and tantalum boride, for which difficulty in fabricating experimental tubes was encountered.

Preliminary to obtaining any experimental data, a number of analytical calculations were performed to predict the influence of cesium adsorbed on a variety of metallic substrates, and to determine the influence of the various substrates as adsorbates on a tungsten substrate. An analysis of several other properties of the metals, which are pertinent to their application as cesium contact ion thrustor electrode surfaces, is included.

SECTION II

PRELIMINARY ANALYSES OF ELECTRODE CANDIDATE MATERIALS

The selection of the best materials from which to fabricate cesium ion thrustor electrodes must be based on a weighted intercomparison of a number of characteristics and properties of the total group of candidate materials for each electrode type. Known characteristics and those predictable by analytical techniques have been analyzed in order to aid in the selection of materials from which to fabricate three cesium ion thrustor electrode types — accelerating electrodes, focusing electrodes, and the cesium ionizer.

A.   ACCEL ELECTRODE

A large portion of this accel electrode section was done under Hughes Aircraft Company funding and has been previously reported.[1]

The accel electrode selection criteria can be divided into two general groups — basic physical characteristics and engineering properties. The major elements of these two groups are listed below:

Basic Physical Characteristics

a.   sputtering ratio for 5- to 10-kV cesium ions

b.   desorption energy from ionizer surface and influence on ionizer work function

c.   cesiated electron emission properties

d.   melting point temperature and evaporation rate

Engineering Properties

a.   structural strength

b.   machinability

c.   cesium compatibility

d. ionizer compatibility (alloying and sintering rate effects)

e. availability

f. cost

g. hazard.

Because of the basic role of the accel electrode in the cesium ion thrustor, the fundamental list of candidate materials to which these selection criteria are to be applied is assumed to comprise only the conductors. The following detailed analysis of the selection criteria will be limited to the conducting elements (the metals plus carbon and silicon) because (1) the gross conductor category includes a nearly inexhaustible number of metal alloys, (2) the alloys are all basically composed of the metals, and (3) the alloys should have the basic physical properties of their elemental constituents.

The purpose of this analysis is to examine the four basic physical characteristics of the metals to determine which may serve as candidate electrode materials; after passing these fundamental physical requirements, the metals can then be examined from the considerations of the engineering properties listed above. In this analysis, most of the elements are eliminated as acceptable candidates in several categories. The merits of the most promising candidates are discussed individually in the Conclusions.

1.   Melting Point Temperature and Evaporation Rate

The accel electrodes of an ion thrustor absorb the radiant energy emitted by the ionizers, which raises their temperature considerably. Energetic ion impingement causes further localized heating. Forced cooling of the numerous long thin pieces which comprise the accel electrode structure of a large ion thrustor is impractical where remote heat rejection is required.

The melting point temperatures[2-4] and vapor pressures at 1000K[5] of about 50 elements are tabulated in columns three and four of Table I. Many of the elements are eliminated by the melting point

TABLE I

Characteristics of the Metallic and Conducting Elements

Element	Z	Melting Point, °C	Vapor Pressure at 1000K, Torr	Atom Desorption Energy from Tungsten at Low Coverage and 1400K, eV/atom	Change in Work Function of Tungsten Caused by Coverage of 0.05, eV	Sputtering Ratio for 5-kV Cesium Ions	Atom Desorption Energy for Cesium at Low Coverage and 1000K, eV/atom	Vacuum Work Function, eV	Cesiated Work Function at $\theta = 0.05$, eV	Cesiated Work Function for $\mu_{Cs} = 5 \times 10^{15}$ atoms/cm²-sec T = 1000K, eV	Ion Desorption Energy for Cesium at Low Coverage and 1400K, eV/atom	Difference Between Atom and Ion Desorption Energies at Low Coverage, eV/atom
Lithium	3	181	7 (-1)	3.37	-0.69	—	1.26	2.49	2.41	2.49	2.64	+1.38
Beryllium	4	1283	3 (-8)	2.98	-0.36	~1.1	2.23	3.92	3.72	3.84	2.18	-0.05
(Boron)	5	2027	< (-15)	5.11	-0.02	~1.2	2.85	4.50	4.24	3.45	2.22	-0.63
(Carbon)	6	~3550	< (-17)	7.56	(+0.04)	1.2	2.94	4.60	4.27	2.99	2.21	-0.73
Sodium	11	98	1 (+2)	2.93	-0.59	—	1.01	2.28	2.22	2.28	2.60	+1.59
Magnesium	12	650	1 (+1)	3.27	-0.26	~2.0	1.57	3.68	3.50	3.68	1.76	+0.19
Aluminum	13	660	5 (-8)	3.72	-0.16	~3.0	2.26	4.08	3.86	3.94	2.05	-0.21
(Silicon)	14	1423	2 (-13)	4.89	(-0.13)	~1.2	2.28	4.15	3.92	4.01	2.00	-0.28
Potassium	19	63	6 (+2)	2.69	-0.38	—	0.90	2.24	2.20	2.24	2.53	+1.63
Calcium	20	850	2 (-1)	3.79	-0.36	—	1.33	2.70	2.62	2.70	2.49	+1.16
Scandium	21	1423	2 (-9)	3.98	-0.24	—	1.97	3.60	3.43	3.60	2.24	+0.27
Titanium	22	1677	6 (-14)	5.44	-0.19	0.8	1.92	3.95	3.74	3.95	1.84	-0.08
Vanadium	23	1917	< (-14)	5.57	-0.15	0.7	2.06	4.12	3.89	4.10	1.81	-0.25
Chromium	24	1900	8 (-11)	5.04	-0.25	0.7	1.91	3.90	3.64	3.79	1.89	-0.02
Manganese	25	1244	5 (-5)	4.34	-0.28	1.0	1.59	3.83	3.63	3.83	1.63	+0.04
Iron	26	1539	1 (-11)	4.47	-0.02	1.7	2.11	4.48	4.22	4.45	1.50	-0.61
Cobalt	27	1495	6 (-12)	4.56	-0.06	2.4	2.08	4.40	4.15	3.38	1.55	-0.53
Nickel	28	1455	2 (-12)	4.07	+0.20	2.7	2.41	5.03	4.72	4.72	1.25	-1.16
Copper	29	1083	1 (-8)	3.22	-0.03	6.8	2.46	4.46	4.20	4.13	1.87	-0.59
Zinc	30	420	9 (+1)	3.00	-0.23	~20	1.60	3.90	3.70	3.90	1.57	-0.03
Gallium	31	30	6 (-7)	3.36	-0.14	~15	2.03	4.12	3.89	4.12	1.78	-0.25
Germanium	32	960	3 (-10)	4.57	-0.01	—	2.16	4.50	4.24	4.46	1.53	-0.63
Rubidium	37	39	1 (+3)	2.61	-0.35	—	0.84	2.09	2.06	2.09	2.62	+1.78
Strontium	38	770	7 (-1)	3.63	-0.29	—	1.29	2.74	2.65	2.74	2.42	+1.13
Yttrium	39	1500	4 (-12)	4.38	-0.18	—	2.15	3.60	3.47	3.56	2.37	+0.22
Zirconium	40	1852	< (-15)	4.74	-0.11	1.1	2.20	4.21	3.98	4.15	1.86	-0.34
Niobium	41	2487	< (-19)	6.65	-0.14	1.0	2.27	4.01	3.79	3.88	2.13	-0.14
Moybdenum	42	2610	< (-18)	6.16	-0.10	1.4	2.41	4.21	3.97	3.97	2.08	-0.33
Technetium	43	2127	< (-16)	5.58	-0.04	1.6	2.49	4.40	4.15	3.95	1.96	-0.53
Ruthenium	44	2427	< (-17)	5.32	-0.01	1.7	2.49	4.52	4.26	4.05	1.84	-0.65
Rhodium	45	1966	< (-15)	4.88	+0.08	2.1	2.57	4.80	4.51	4.21	1.64	-0.93
Palladium	46	1550	1 (-10)	3.97	+0.15	5.2	2.33	4.98	4.67	4.67	1.22	-1.11
Silver	47	961	4 (-6)	2.53	-0.06	13	2.31	4.35	4.10	4.11	1.83	-0.48
Cadmium	48	321	5 (+2)	2.69	-0.13	~30	1.59	4.07	3.85	4.07	1.39	-0.20
Indium	49	156	8 (-5)	3.41	-0.08	6.1	1.97	4.20	3.97	4.20	1.64	-0.33
Tin	50	232	6 (-8)	4.15	-0.05	4.3	1.95	4.38	4.13	4.38	1.44	-0.55
Antimony	51	631	8 (-1)	3.97	-0.11	9.7	1.77	4.15	3.92	4.15	1.49	-0.28
Cesium	55	29	1 (+3)	2.60	-0.34	—	0.77	1.81	1.81	1.81	2.84	+2.07
Barium	56	725	1 (-1)	3.84	-0.37	—	1.18	2.11	2.08	2.11	2.94	+1.76
Lanthanum	57	920	7 (-13)	4.72	-0.23	—	2.00	3.30	3.16	3.30	2.57	+0.57
Hafnium	72	2222	< (-15)	6.23	-0.24	1.5	2.03	3.53	3.36	3.53	2.37	+0.34
Tantalum	73	2997	< (-20)	6.74	-0.09	1.4	2.39	4.19	3.96	3.97	2.07	-0.32
Tungsten	74	3380	< (-21)	6.80	0.00	1.8	2.61	4.54	4.27	3.93	1.94	-0.67
Rhenium	75	3180	< (-19)	5.75	+0.16	2.5	2.85	5.10	4.78	3.79	1.62	-1.23
Osmium	76	2727	< (-19)	5.64	0.00	3.5	2.45	4.60	4.28	4.24	1.77	-0.68
Iridium	77	2454	< (-16)	4.92	+0.23	4.7	2.81	5.30	4.96	4.17	1.38	-1.43
Platinum	78	1769	< (-15)	4.51	+0.26	5.8	2.87	5.32	4.98	3.84	1.42	-1.45
Gold	79	1063	5 (-10)	3.70	-0.06	14	2.32	4.35	4.10	4.10	1.84	-0.48
Mercury	80	-39	2 (+4)	1.21	0.00	~30	1.60	4.53	4.26	4.53	0.93	-0.67
Thallium	81	304	2 (-1)	—	—	~20	—	3.68	—	—	—	—
Lead	82	327	1 (-2)	2.97	0.00	16	1.80	3.94	3.73	3.94	1.14	-0.66
Bismuth	83	271	4 (-2)	—	—	13	—	4.20	—	—	—	—
Radium	88	700	4 (-1)	—	—	—	—	4.25	—	—	—	—
Thorium	90	1845	< (-16)	5.74	-0.21	—	1.75	3.35	3.20	3.35	2.27	+0.52
Uranium	92	1133	2 (-14)	—	—	—	—	3.60	—	—	—	—

consideration, regardless of all other considerations. None of the elements with melting temperatures below about 900C are of interest and are eliminated; all with higher melting points are given further consideration.

Some elements, while having relatively high melting temperatures, also have relatively high evaporation rates (e.g., chromium). Evaporation of electrode structures during long term thrustor operation must be considered because of the resulting loss of structure thickness and because of the deleterious effects of increases in the atom density in the ion beam formation region. Evaporation rates can be calculated from experimental vapor pressure data, and their ordering is approximately the same. Materials with vapor pressures above about 10^{-7} Torr at 1000K probably should not be considered further. While some materials are satisfactory for testing and for short duration missions, careful consideration should be given to evaporation rates for materials for very long mission applications. As an example, for copper, about 0.001 and 0.5 in. of electrode thickness would be lost each 10,000 hours of operation at 1000 and 1200K, respectively. Clearly, local (small area) electrode temperatures must not be allowed to increase above certain limits.

2.   Desorption Energy from the Ionizer Surface and Influence on the Ionizer Work Function

The generally used porous ionizer material in cesium ion thrustors is tungsten. The desorption energies for the elements from a tungsten surface are significant because this quantity determines the mean residence times for atoms sputtered from the accel electrode surfaces onto the ionizer surfaces by energetic cesium ions. The mean residence time then determines the value of equilibrium surface coverage of the ionizer by accel electrode atoms for a given arrival rate. The equilibrium surface coverage, in turn, determines the change in the ionizer surface work function caused by the presence of these foreign atoms.

Foreign atoms incident on the porous ionizer surface, especially those with long residence time, i.e., those with high desorption energies, also may tend to clog the ionizer pores and thereby reduce the cesium flow and the extractable cesium ion current density.

The quantities sought here are the desorption energy for isolated atoms of the accel electrode material adsorbed on a tungsten lattice at high temperature (for low values of equilibrium surface coverage), and the change in work function of the ionizer surface for the corresponding equilibrium surface coverage. Experimental values for these two quantities are not known for the elements of interest. Therefore, they must be calculated from known basic properties and characteristics of the elements. A separate analytical study of this problem was carried out and is included in the Appendix. The values of atom desorption energy at low coverage from a tungsten lattice and the change in tungsten work function caused by a coverage of 0.05 of electrode atoms, as calculated with a 7094 computer using the theoretical approaches described in the Appendix, are tabulated in columns five and six of Table I. The calculations include the influence of the ionizer temperature on the desorption energy. The refractory or high melting temperature metals (defined here as metals with a melting point temperature well above the ionizer temperature) have been corrected for the crystallographic factor described in the Appendix. All values of desorption energy up to 3.5 eV are designated as satisfactory, those in the range 3.5 to 4.3 eV as questionable, and those above 4.5 eV as eliminated. This is a rather severe limitation which eliminates a great many of the metals.

The analytical expressions, including the modifications to account for crystallographic structure and temperature, were used in a digital computer calculation to compute the surface coverages and the resulting changes in the work function of a tungsten surface (at 1400K) as a function of the arrival rate of atoms of all of the metallic elements. The data are plotted in Fig. 2 for some high-vaporization-rate accel electrode candidates. These plots predict that copper produces the lowest coverage and changes the work function the least of the accel electrode
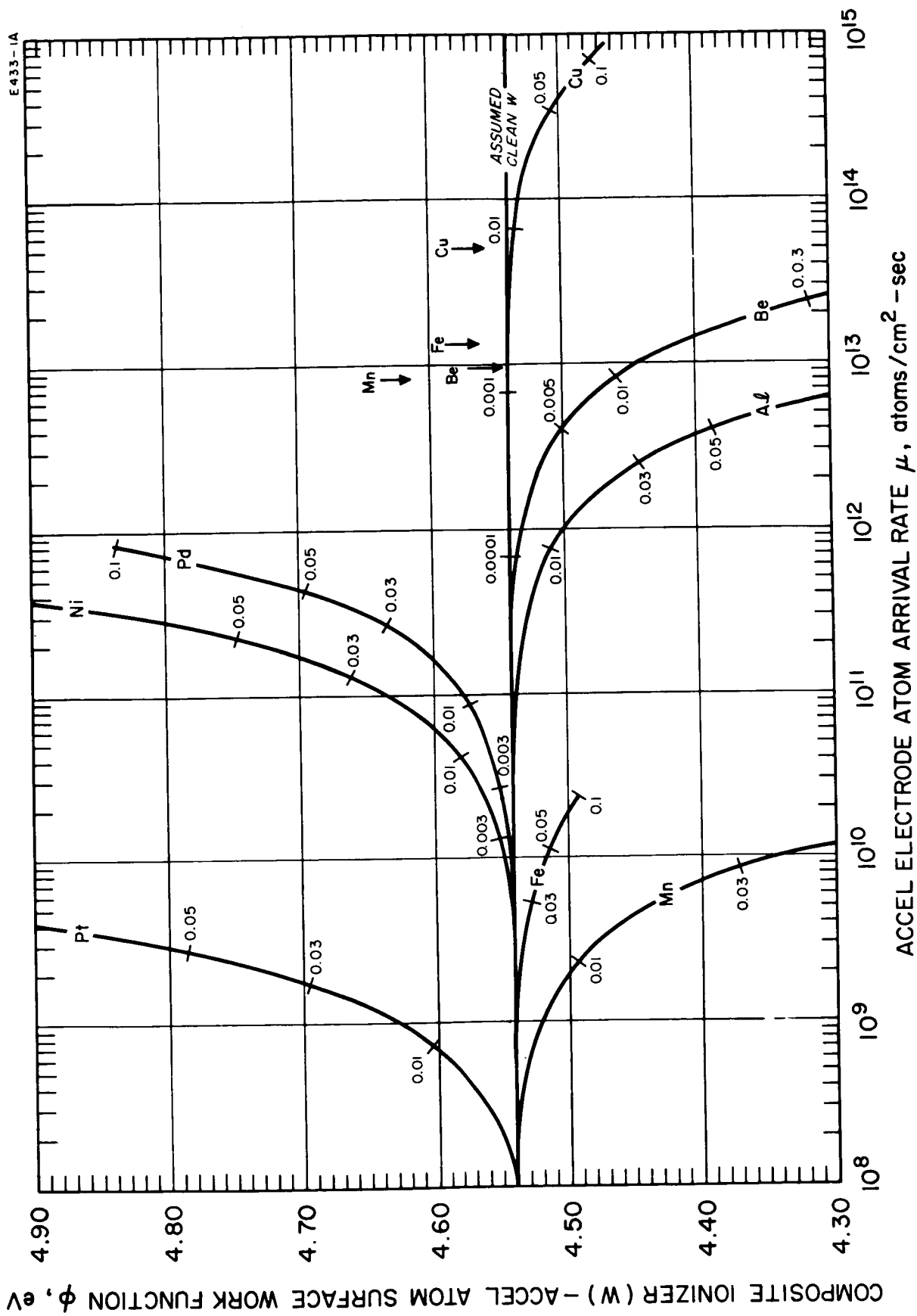
Fig. 2.   Influence of accel electrode atoms on ionizer work function.   The arrows indicate calculated arrival rates expected in ion thrustors.

candidates at high arrival rates, and that it is suitable for all arrival rates below about 10^{15} atoms/cm^2-sec. Beryllium is second; it reduces the work function more than copper at equivalent coverages (assuming a vacuum work function of 3.9 eV) and is probably suitable for arrival rates below about 10^{13}. However, this is not so unfavorable a comparison with copper as might first be thought, because the sputtering rate (yield) of copper is almost an order of magnitude greater than that of beryllium. This implies that for equivalent ion current densities the arrival rate of sputtered beryllium should be an order of magnitude less than that of copper. For lower arrival rates, other metals, viz., nickel, iron, chromium, and manganese, become candidates. Nickel is the best of these because equivalent coverages are reached for an order of magnitude higher arrival rates than for the others, and because nickel raises the surface work function. Nickel, however, is known to increase the sintering rate of porous tungsten.

These calculations predict that all of the high work function elements can increase a composite ionizer surface work function. Therefore, there is an advantage to having the accel electrode be of a high work function element because any resulting increase in ionizer work function will reduce the neutral cesium fraction emitted from the ionizer surface (as calculated from the Saha-Langmuir equation), which will, in turn, reduce the rate of charge exchange by reducing the neutral cesium density, in turn reducing the rate of sputtering of the accel electrodes. The calculations made here show, however, that three of the six high work function elements (iridium, rhenium, and rhodium) are probably unsuitable because of their high binding energies to tungsten, resulting in high coverages for very low arrival rates (less than 10^8). Platinum is found to be better — in the range up to the mid-10^9 arrival rate. Nickel and palladium are seen (Fig. 2) to be the best, although both may have the disadvantage of increasing the sintering rate of tungsten. For already very slow sintering rates, this may not be a problem.

3.   Sputtering Ratio for 5- to 10-kV Cesium Ions

The sputtering ratio (i.e., the number of neutral atoms sputtered from a surface per incident ion) of the accel electrode material is significant in determining the erosion rate, and therefore the life expectancy, of the accel electrodes. The sputtering ratio also determines the rate of arrival of accel electrode atoms on the ionizer surface, and therefore the equilibrium ionizer surface coverage and the altered work function of the ionizer. An independent survey of the literature concerning sputtering and secondary emission was carried out. Plots of experimentally measured sputtering ratio S versus energy, incident ion species (atomic number), and atomic weight of the substrate surface have been made from several references.[6-8][*] Values of S for 5-kV cesium ions obtained from this analysis for the elements for which sputtering data were analyzed are tabulated in column five of Table I. Values of S over 8 have been eliminated, those between 2 and 8 are questionable, and those lower than 2 are satisfactory. Higher values of S can be tolerated for elements having lower values of desorption energy on tungsten.

4.   Cesiated Electron Emission Properties

An accel electrode material with low electron emission properties in the presence of an equilibrium surface coverage of cesium is desirable to prevent large wasted drain currents of energetic electrons from leaving the accel electrodes and terminating on the ionizer and focus electrodes, where they cause undesirable local heating as well as power losses. Thermionic emission from cesiated refractory metal surfaces in the presence of small electric fields is known to exhibit maxima and minima (known as S curves) as the surface temperature is varied. This analysis has shown, from other considerations, that the refractory metals are not candidates for accel electrodes. It is also to be realized that the present electrode geometry in the ion thrustor is plane parallel, with a spacing and applied potential difference

---

[*]Note added in proof: Prof. H. Smith is currently measuring these sputtering yields for appropriate metals at the University of California, Berkeley, on Contract NAS 3-5743.

resulting in an electric field at the accel electrode surface of 10^5 V/cm. Therefore, the thermionic emission under discussion here is from non-refractory as well as refractory metal surfaces, in the presence of high electric fields.

Thermionic electron emission from cesiated metal surfaces has been studied primarily for the refractory metals, and those data are not entirely consistent. The published data are for zero field (applied surface electric field) conditions, while in an ion thrustor the surface fields are of the order of 10^5 V/cm. One of the major goals of this experimental program was to determine the cesiated electron emission properties of some candidate surfaces and to study the influence of applied electric fields up to 10^5 V/cm.

Because the experimental data were not available at the beginning of this program, a method for determining the expected cesiated electron emission properties by combining known properties with calculated ones to allow a preliminary relative evaluation was desired. Quantities important for determining the cesiated electron emission properties are the vacuum work function, the variation of surface work function with cesium coverage, and the desorption or binding energy for cesium on the electrode surface as a function of surface coverage. Calculations of these quantities were performed with the 7094 computer program using the expressions resulting from the analytical treatment of the Appendix. Vacuum work functions and calculated zero-coverage atomic desorption energies for cesium on the metals at 1000K, and calculated cesiated work functions at a coverage of 0.05, are tabulated in columns eight, nine, and ten of Table I. As the cesium surface coverage increases, the cesiated work function of all surfaces will approach the work function of bulk cesium (~ 1.8 eV), and copious electron emission will result. The quantity which determines the equilibrium cesium surface coverage for a given arrival rate is the desorption energy for cesium adsorbed on the electrode surface. The dependence is exponential. As the cesium equilibrium surface coverage at a given arrival rate decreases, the reduction in the surface work function decreases,

14

resulting in smaller thermionic electron emission. If the surface coverage is low, the electron emission decreases with higher uncesiated surface work function. However, as the uncesiated surface work function increases, the cesium desorption energy increases. Calculated values of cesiated work function of the metals for an arrival rate of 5×10^{15} atoms/cm^2-sec and a surface temperature of 1000K are listed in column eleven of Table I. These values are calculated using the curves of desorption energy and composite surface work function versus surface coverage generated by the 7094 computer program.

Surfaces with low uncesiated work function will always have low cesiated work function regardless of the magnitude of the coverage, and therefore will always have high electron emission. Surfaces with high uncesiated work function probably have high cesium desorption energy, low cesiated work function, and high electron emission. The surfaces with moderate, uncesiated work functions probably have the highest cesiated work functions, and they are therefore desirable for accel electrode surfaces.

B. FOCUS ELECTRODE

The focus electrodes may be a series of structures, close to but independent of the cesium ionizers, or they may be eliminated as independent structures by any of several integral focus electrode concepts. In the latter case, however, some areas between the adjacent ionizer surfaces which face the accel electrodes become possible sources of unfocused cesium ions, being a sharp edge in the limit. The criteria for focus electrode material selection are almost diametrically opposed to those for accel electrodes. The sign of the surface electric field is opposite, preventing electron emission, but allowing cesium ion emission. The competing processes of atom and ion desorption become important. The closer proximity of the focus electrode to the ionizer (or inclusion as part of the ionizer structure) increases the melting temperature and evaporation rate requirements. If an independent structure

15

concept is employed, structural strength at high temperatures may be required, raising the lower limit on melting temperatures still higher. Sputtering ratio is of no concern. The problem is essentially one of finding a high melting point material with a low cesiated work function.

A basic problem of interaction between the focus electrode and the accel electrode must be considered prior to further discussion of the basic focus electrode material. The accel electrode material is not only sputtered back onto the ionizer, but also onto the focus electrode surfaces. The same arguments apply to the desorption energy of the accel electrode material from the focus electrode material, the equilibrium surface coverage of accel material on the focus electrode, and resulting changes in the work function and critical temperature of the composite focus electrode surface, as for the ionizer. Therefore, there are two concepts of focus electrode operation. (1) The focus electrode can be operated at a temperature of the order of that of the ionizer, to minimize the equilibrium surface coverage of the accel electrode material on the focus electrode. (2) The focus electrode can be cooled[*] to a temperature enough below the critical temperature of the accel electrode material to reduce the ionization efficiency of the surface of the focus electrode, which will then be composed of the accel electrode material to a low enough value that the resulting emitted cesium ion flux will cause less sputtering of the accel electrode than sputtering from other sources. In this latter case, the composition of the focus electrode substrate material has no bearing on the problem of cesium ionization and can be chosen by entirely different criteria. In this case, the only important surface physics characteristic for the focus electrode analysis is the critical temperature for cesium ionization of the <u>accel</u> electrode material. Other problems exist, such as cooling the focus electrode and the effect of increasing thickness of the focus electrode. In the former case of a "clean" focus electrode, the additional analysis made below is required.

A material with a low vacuum work function will always have a low cesiated work function because the presence of any equilibrium cesium coverage can only further reduce the composite surface work

---

[*]This concept is probably impractical in an operating ion engine.

function. A significant favorable characteristic is to have the greatest possible energy difference between the cesium atom and ion desorption energies, with the atom energy lower. For this reason, the zero-coverage cesium ion desorption energies and the differences between them and the cesium atom desorption energies as calculated in the analytical computer program are included as columns twelve and thirteen in Table I. The selection criteria become simpler in this case. A refractory material with a low bare work function or low cesiated work function, and an ion desorption energy as much higher than the corresponding atom desorption energy as possible, is required. A survey of the significant characteristics of the pure elements quickly indicates two far superior materials: thorium and hafnium. The nearest competition is a group of three (titanium, niobium, and vanadium), all poor seconds. The availability and cost of both of the superior metals are a consideration, with hafnium having a probable advantage. In recent years, the availability of hafnium has been greatly aided by the nuclear reactor program. The combination of the large difference between the ion and atom desorption energies and the low bare or cesiated work function for both metals virtually insures negligible cesium ion emission.

Nonelemental refractory materials can be considered for focus electrode materials — those possibly having low work functions. Of greatest consideration have been the silicides, carbides, and borides of the refractory metals (e.g., $MoSi_2$, ZrC, and TaB_2). Some indication exists in the literature that these materials have low vacuum work functions, at least initially, but that their work functions may increase with time, possibly because of diffusion of the surface layer inward, resulting in a change in the surface stoichiometry. Another possibility is a changing condition of contamination in the experiments. Other possible poor cesium ionizing refractory materials are some of the metal oxides (e.g., alumina and beryllia), provided they are sufficiently conducting at high temperatures to maintain a surface equipotential. Two refractory metal compounds, $MoSi_2$ and TaB_2, and one oxide, Al_2O_3, were investigated under this contract. The results are discussed in Section IV.

C.   IONIZER

The foregoing analysis of focus electrode materials can be easily extended to a quick comparison of the metals for cesium ionizers. Criteria apply which are opposite to those discussed for the "clean" focus electrode analysis.   A refractory material with a maximum difference between the ion and atom desorption energies (atom energy higher), combined with a maximum (cesiated) work function, is the desirable material. For a high current density ionizer, a high operating temperature is required.   Structural strength requirements at high temperatures push the limit still higher.

Using the expression

$$J_+ = \left(\frac{e\theta'\sigma(1)\omega}{2} \right) \left[\frac{NF}{2(1-NF)} \right]^K \tag{1}$$

where

$$K = \left[\frac{\lambda_+(\theta) - e\sqrt{eE}}{\phi(\theta) + e\sqrt{eE} - V_i} \right] .$$

From the Appendix, and using values of $\lambda_+(\theta)$ and $\phi(\theta)$ calculated in the computer program, curves can be obtained for neutral fraction (NF) versus cesium ion current density which include the influence of cesium coverage.   This has been done for the pure metals with melting points high enough to be of interest for ionizers; the results are shown in Fig. 3.   The value of θ' (the cesium coverage where NF is a minimum) is taken as 0.02 in the calculations. If the value of θ' should be slightly different, it will probably be less than 0.02, and the influence on the curve is minor because θ' is not in the exponential.   The value of θ for which $\lambda_+(\theta)$ and $\phi(\theta)$ are evaluated is crucial and has a much greater influence on the curves, as has been shown in Fig. 3 for tungsten.   Values for θ of 0.00, 0.01, 0.02, and 0.03 were used to obtain four corresponding curves for tungsten.   This influence can be

18
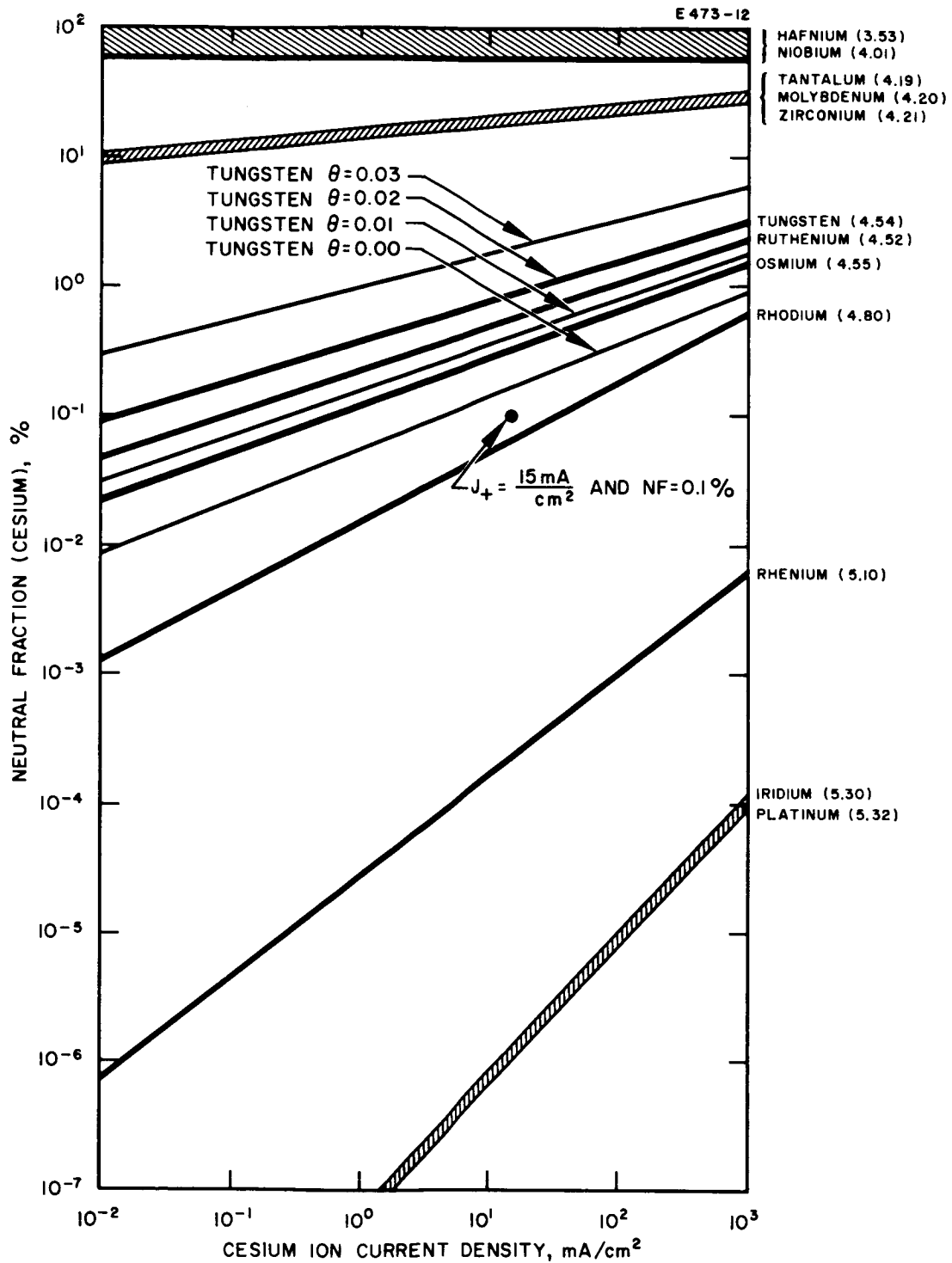
Fig. 3. Neutral franctions versus cesium ion current density for the refractory metals. The numbers in parentheses are the asuumed vacuum work functions of the metals.

extrapolated to the other metals. The calculation also assumes a constant value of $\sigma(1)$, the cesium atom concentration at $\theta = 1$, for all metals. This is not strictly true, but the value cannot vary greatly and will not have an important influence because $\sigma(1)$ is also in the pre-exponential term.

If the point 0.1% NF at 15 mA/cm^2 is taken as a minimum tolerable condition for long life thrustors, Fig. 3 shows that hafnium, niobium, tantalum, molybdenum, and zirconium would be very poor cesium ionizers under all circumstances; tungsten, ruthenium, and osmium are fair, but unsuitable for long life; rhodium is barely satisfactory; only rhenium and iridium are satisfactory. (Platinum has a questionably low melting temperature, and its cesium compatibility is questionable.)

SECTION III

EXPERIMENTAL DESIGN AND TECHNIQUES

This work has required studying the influence of fractions of a monolayer of a specific adsorbate (cesium) on the electron and ion emission characteristics of a number of nonrefractory and refractory surfaces, including metals, semiconductors, and insulators. Therefore, an ultraclean, ultrahigh vacuum environment was essential, and a method was required for quickly and efficiently studying electron and ion emission versus surface temperature so that data could be obtained quickly, i.e., after the emitter surface was cleaned and before any small partial pressures of any ambient gases could contaminate the emitter surfaces. Such a system was placed in operation, and techniques were developed for automating emission measurements with nonrefractory as well as refractory surfaces. The vacuum system, the experimental techniques, and the experimental tube were designed with certain specific goals or conditions in mind; some of these are discussed below.

A. TUBE DESIGN

To simulate cesium ion thrustor electrode conditions as closely as possible, a plane parallel electrode geometry was chosen, with about 1 mm spacing and with the capability of applying high electric fields of either polarity. For the same reason, all of the materials studied were required to be polycrystalline "as received" or machined surfaces. Figure 4 is a schematic diagram of the experimental tube.

In the study of energetic cesium ion emission, the closely spaced planar collector surface material is sputtered back onto the emitter surface, especially at high ion current densities (high accelerating potential). Therefore, to maintain the basic nature and characteristics of the emitting surface during all emission measurements, the collector
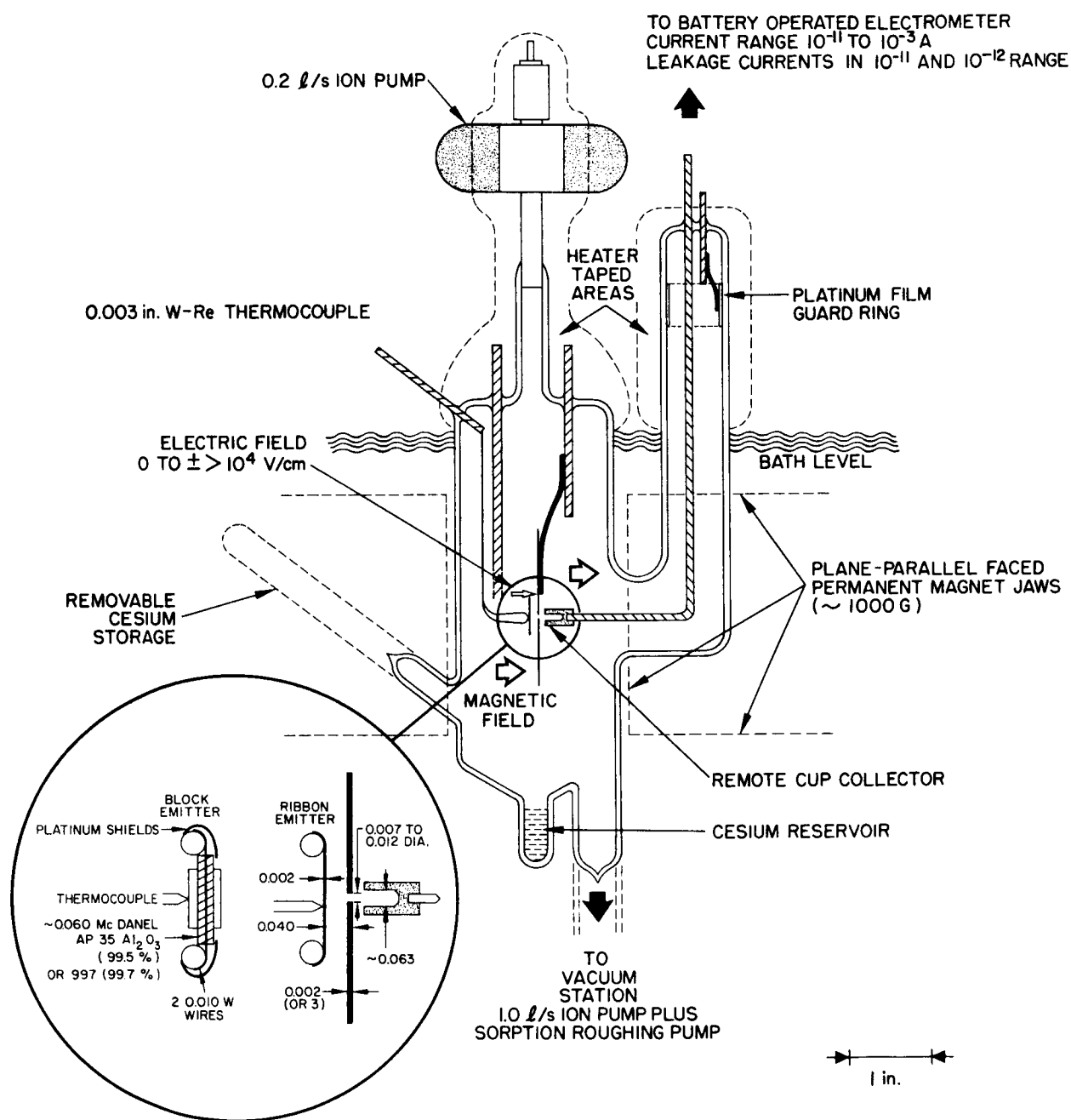
Fig. 4. Experimental tube schematic.

surfaces were also fabricated from the emitter material under study (unless this was electrically infeasible), so that the results are known to be characteristic of the pure material under study and not influenced by a partial or complete layer of a dissimilar collector material.

For the refractory materials, a ribbon emitter 0.001 or 0.002 in. thick and about 0.10 in. wide was heated directly by ac current. A uniform temperature was created in the critical central region of the collector aperture and the thermocouple so that the cooling toward the ribbon ends was unimportant. The nonrefractory materials were heated indirectly by insulated central tungsten wires. The emitters were machined from square or round rods of high purity material. A high purity alumina insulator (AP 35 and McDanel 997) housing two 0.010-in. tungsten heater wires was fixed in the center of the emitter. These indirectly heated emitters assumed a very uniform temperature distribution over their entire surface. The alumina insulator protruded from each end, and it and the tungsten heater wires were shielded from the collectors by cool platinum foils mounted remotely.

In order to measure as accurately as possible the electron and ion current densities and the associated emission surface temperatures, a double collector system (see Fig. 4) was employed which consisted of a large area ($\sim$ 1-1/2 by 1-1/2 in.), very thin (0.002 in.) planar collector parallel to the emitter face, in which was machined a small aperture (0.007 to 0.012 in. diameter) which was located opposite the center of the emitter face. Behind the aperture was positioned a Faraday cup collector with an internal diameter several times the diaphragm aperture diameter ($\sim$ 0.060 in.). A potential difference applied between the emitter and diaphragm collector created a normal electric field in the region of the aperture and over most of the emitter face. To insure additionally that the area from which the emitted electron current, passing through the diaphragm aperture and collected by the Faraday cup, is just the projected known area of the aperture, a normal magnetic field was always superimposed on the normal electric field by a permanent magnet with a field strength of about 1000 G (see Fig. 4). The area of the aperture was measured with an optical comparator at 100x.

23

The cup collector which monitored the small aperture currents was mounted remotely on a special side arm of the tube which extended out of the temperature bath (see Fig. 4). The leakage currents through the cesium layer adsorbed on the glass envelope walls were minimized by two methods. The glass walls of the collector arm were heated by tapes during measurements to reduce the cesium coverage, thereby increasing the leakage resistance. In addition, a platinum guard-ring film was deposited on the inside arm walls. The film was grounded through an independent lead through the tube envelope (see Fig. 4). The background currents in this circuit were generally on the 10^{-11} A scale, and sometimes on the 10^{-12} A scale, allowing emission currents to be measured through seven or eight orders of magnitude.

Two limiting factors in these measurements were the cesium film leakage currents and photoelectric emission currents from the collectors. To minimize photoelectric emission, the tubes were operated in the absence of external light. Nothing could conveniently be done to prevent the ultimate limitation of photoelectric emission resulting from radiation from the hot emitter which was incident on the collectors. (Magnetic deflection of the beam into a shadowed region and collector biasing could influence the small emission currents, thereby defeating the original purpose.) The influence of external light was observed to be very severe, and care was taken to shield against it. However, photoemission from the collector may still have ultimately been the limiting factor in the background currents in these experiments.

B. EXPERIMENTAL TECHNIQUES

The temperature of the emitter was measured by 0.003-in. tungsten-rhenium thermocouple wires spot welded to the emitter, close together on the directly heated ribbon emitters and spaced to span the emitter area opposite the aperture on the indirectly heated emitters, so that they did not influence the emission from the small critical emitting area and yet accurately measured the temperature of it.

To provide the capability for controlling and varying the cesium arrival flux over a wide range of values, the experimental tubes were submerged in a large volume of liquid in a magnetic thermostatically controlled temperature bath. The bath was capable of maintaining a temperature to within 0.05C in the range from ambient to 300C. By using ice and water or dry ice and alcohol, the range was extended to -30C with an accuracy of about 0.5C.

The cesiated electron emission S curves and the ion emission (critical temperature) curves were quickly and efficiently measured and recorded by feeding the dc millivolt output of the emitter thermocouple to the independent variable axis of an X-Y recorder, and each of the two collector current outputs, in turn, through battery-operated electrometers to the dependent variable axis of the X-Y recorder. This technique allowed electron S curves and cesium ion emission (critical temperature) curves to be measured and recorded continuously as the surface temperature was varied in either direction and at various rates of temperature change.

The electronics of the experiment are shown in the block diagram of Fig. 5. The main units are (1) the temperature bath, experimental tube, and magnet; (2) the regulated and isolated emitter heater circuit to which the electric field producing voltage was applied from a well-regulated dc power supply; (3) the two shielded electrometer collector circuits, each of which could be fed to the X-Y recorder; (4) the thermocouple-potentiometer circuit; (5) the X-Y recorder; and (6) the ion pump and control circuit.

Calibrations of the X-Y recorder traces were performed during each temperature sweep. Temperature and current level axis calibrations were never made independently of the data curves. The temperature axis was calibrated at appropriate points by a calibrated potentiometer through a switch, as shown in Fig. 5. The current level axis was frequently calibrated by having the recorder pen lift momentarily as it passed the major scale divisions on the electrometer scale. The electrometers used in this work were capable of measuring currents in the
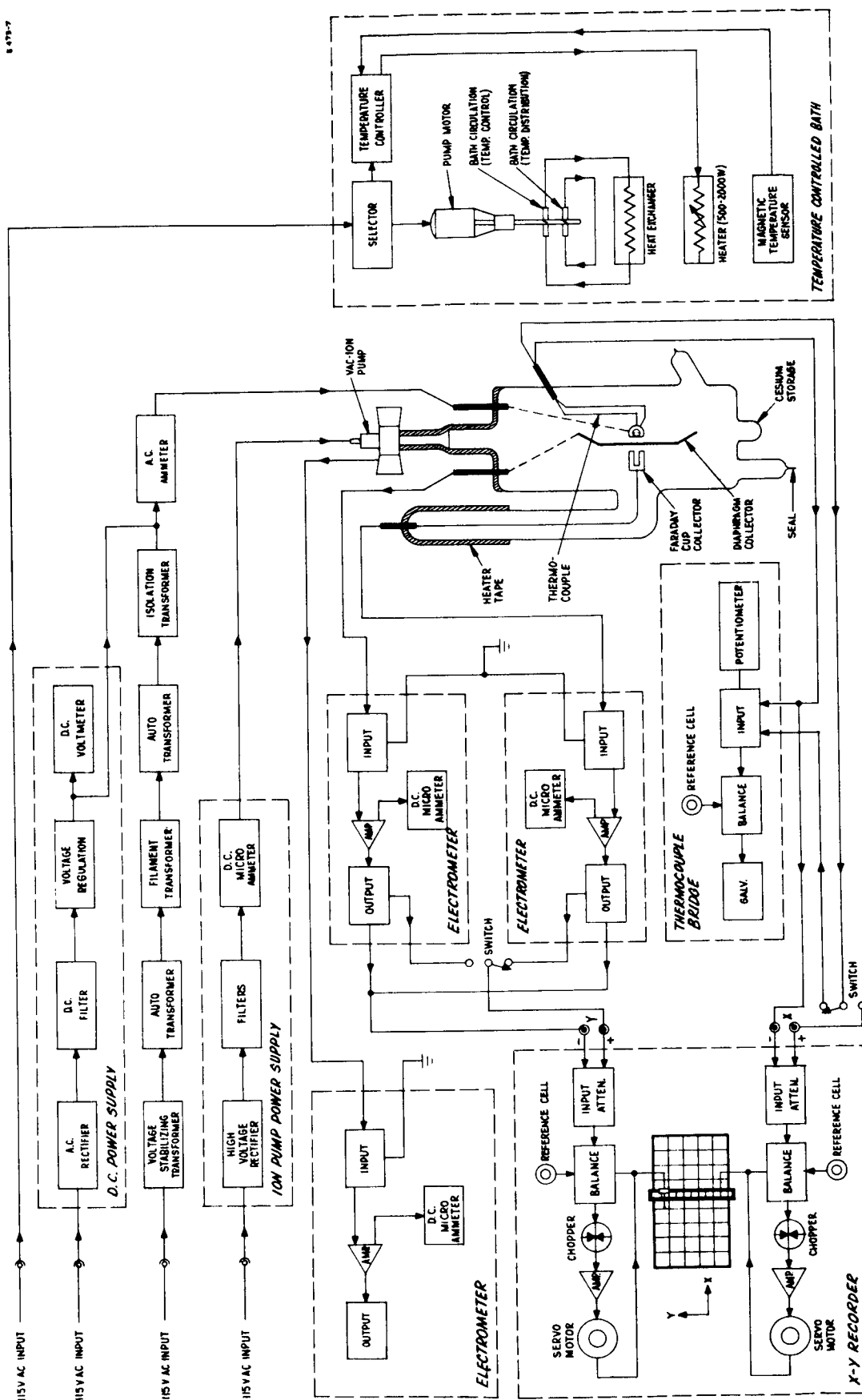
Fig. 5. Experimental electronics block diagram.

10^{-14} A range. Currents down to the 10^{-12} A range were monitored in the cesiated emission measurements, and currents down to the 10^{-13} and 10^{-14} A range were recorded in the vacuum emission measurements.

The rate of change of emitter temperature was controlled by controlling the rate of change of the emitter heater current. It was therefore possible, by driving only the emitter heater current, to record a well-calibrated continuous plot of emission current versus surface temperature for temperature variation in either direction, to check reproducibility quickly and accurately, and to check for effects caused by variation of the rate of change of surface temperature. An important advantage of this technique was that electron emission curves were recorded graphically as continuous S curves with frequent calibration. Another important advantage was that the rapid automatic procedure made it possible to obtain emission data immediately following cleaning of the emitter surface, before any low partial pressures of ambient gases could significantly contaminate the surface. For example, at a pressure of 10^{-8} Torr of gases other than cesium vapor, a monolayer is not formed for 100 sec; which is longer than the time required to obtain a complete current versus temperature plot from 500 to 2000K. The only restriction on this technique was that only 500 V could be applied to the floating X-Y recorder input terminals. This corresponded to an upper limit on the applied electric field of 5000 V/cm because the thermocouple output was at high voltage. Therefore, data could not be obtained by this technique for applied voltages in the kilovolt range.

Two techniques were employed in this work to determine the purity and/or composition of the emitter materials studied. One was spectrographic chemical analysis and the other was x-ray diffraction. X-ray diffraction was especially used to make stoichiometric determinations in the fabrication of suitable high purity refractory compound emitters ($MoSi_2$, TaB_2, and Al_2O_3) and was performed in this laboratory. It was also used to check the purity of emitters after high temperature operation, such as for the alumina, chromium, $MoSi_2$, and TaB_2 emitters. An example of the results of such measurements is reported in Section IV-A (discussion for chromium).

The vacuum work function measurements were made by recording the cup and diaphragm collector currents at a series of values of applied electric field at each of a series of emitter surface temperatures between the lower temperature limit, at which measurable currents were first observed, and the upper limit of either the melting point temperature or the temperature at which vaporization of the emitter became a serious problem. The emitter temperature was first raised to the upper limit where thermal cleaning occurred — thermal flash desorption for the refractories and vaporization of the outer emitter surface for the nonrefractories. The temperature was then lowered in a series of steps, at each of which a thermal equilibration time was allowed. Generally a second series of measurements was made for increasing temperature steps following the high temperature cleaning and an immediate decrease to the lower temperature limit. At each temperature step, the applied field was varied from a few thousand volts per centimeter to zero in all cases, and in a few cases from between 10^4 and 10^5 V/cm to zero and back up (to check for high field effects). Usually the data were so flat (small field dependence) that zero-field extrapolation could be accurately accomplished on a linear field plot, especially for the aperture-cup collector system. Occasionally, the data were transferred to a $\sqrt{E}$ plot for greater accuracy in the zero-field extrapolation in the Schottky emission region. All vacuum work function values quoted in Section IV are zero-field-extrapolated effective thermionic work functions. That is, A was always used as 120.4 $A/cm^2\text{-}K^2$ and any resulting work function variation is given as a temperature dependence.

The study of thermionic emission (S curves) from cesiated non-refractory metals, a major portion of this program, is a new field involving some special problems and techniques. Refractory metals can be thoroughly internally degassed by high temperature processing, and surface contamination incident from the ambient pressure (vacuum) can be removed prior to measurements by thermal flashing. Neither of these techniques can be applied to metals which melt at temperatures below the degassing and flashing temperatures. Sputtering of the

surfaces by ion bombardment can be utilized to clean the surfaces prior to short duration measurements, but when the surfaces are subsequently raised to high temperatures to desorb cesium, the dissolved or adsorbed impurities readily diffuse onto the surface, resulting in surface contamination which influences the emission measurements. Oxygen is probably the contaminant species exerting the major influence because it is difficult to drive from the metals in this category, and because even a few atoms of an electronegative gas, such as oxygen, diffusing onto a surface, can act as adsorption centers for a number of cesium atoms which, in turn, reduce the surface work function and increase the electron emission.

In this work, very high vacuums (10^{-9} and 10^{-10} Torr) and very clean (fluidless) ion pumping techniques were combined with a tube design employing emitters and collectors of the same very pure material (5 N's) and fast automatic data collecting techniques, to aid in minimizing the influence of contamination for the nonrefractory metals. However, two problems were still encountered and the following two conclusions result. Some of the nonrefractory metals cannot be degassed enough at temperatures below the limit imposed by complete evaporation of the emitter, to prevent continual diffusion of small amounts of contaminants (probably primarily oxygen) onto the surface at the maximum emission temperatures, which then influence the emission data unless the data are obtained very rapidly. The high vapor pressure of these metals at these maximum emission temperatures and the resulting high atom density in the interelectrode region increase the electrical breakdown voltage threshold and result in discharges in the presence of high applied fields. Both of these problems are practical ones in terms of application to electrodes in cesium contact ion thrustors because high applied fields are essential, and because the electrodes are subject to the same contamination problems encountered in this work. That is, the electrode surfaces cannot be atomically clean either.

C.   VACUUM SYSTEM AND PROCESSING PROCEDURE

Two requirements on the vacuum environment were considered essential for this work. These were an ambient background pressure of 10^{-9} Torr, and a pumping system free from any fluids (vapors). These conditions were achieved with a bakeable ultrahigh vacuum system composed of ion pumps and a chilled molecular sieve sorption pump. It is believed that any influence contaminants may have had on the surfaces studied in this work did not result from adsorption of ambient gases in the vacuum environment, but rather resulted from diffusion onto the surface of internally held gases from within the bulk of the emitter materials during high temperature operation.

Referring to the schematic sketch in Fig. 6, the vacuum system consisted basically of a chilled molecular sieve sorption pump A, a high vacuum valve B, a bakeable ultrahigh vacuum valve C, a 1-liter/sec ion pump D, and a bakeout oven E. The oven was two stainless steel shells filled with Fiberfrax insulation. Three 220-V, 1600-W quartz infrared lamps served as clean heating elements. The power output of the three lamps was found to be sufficient at 110 V and 400 W per element. The oven was light enough that one man could conveniently place and remove it by hand. The experimental tube F was sealed onto a glass manifold. Each tube included a 0.2-liter/sec appendage ion pump G.

The pressure in the system was measured by monitoring the current in the 1.0- and 0.2-liter/sec ion pumps. In order to measure the currents which went below 10^{-7} A, a battery-operated electrometer was placed in the ground side of the ion pump circuit. This lowers the background current by eliminating the leakage current in the control unit (power supply). To this end, the ion pumps were electrically isolated by insulating mounts. Even with this arrangement, it was difficult to obtain accurate measurements of pressures below about 1×10^{-9} Torr because of leakage currents across the ion pump itself. For this reason,

30
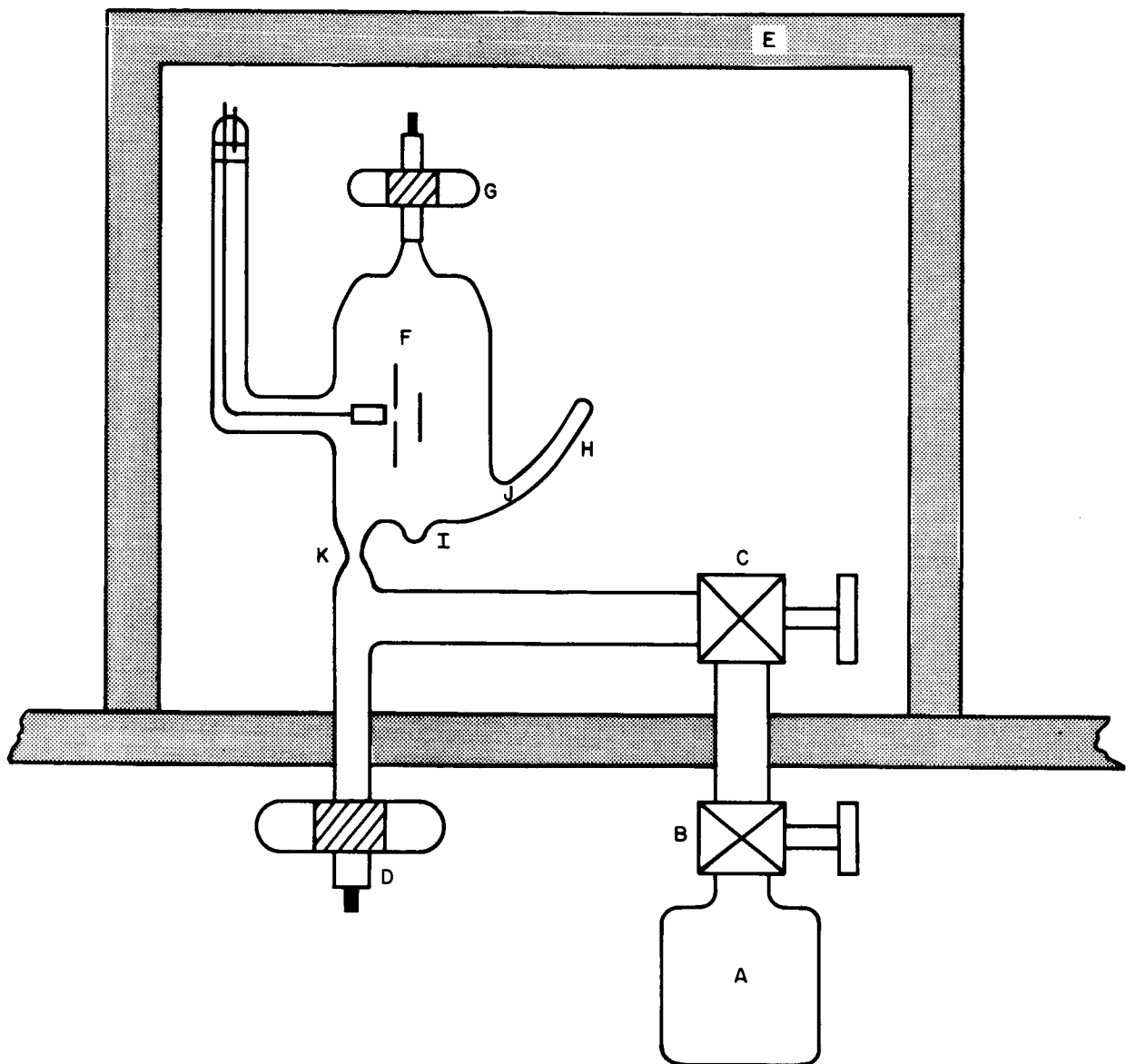
Fig. 6. Vacuum system schematic.

pressures below 1×10^{-9} Torr are generally not quoted; it is noted only that the pressure was at or below 1×10^{-9} Torr. Higher pressures are quoted from ion pump current calibration curves.

After a newly fabricated tube was sealed on the station, valve C was placed in the open, bakeable condition and valve B was opened. The sorption pump was chilled, and in a few minutes the system pressure was in the low 10^{-3} Torr range. The ion pump D was then baked with heater tape at between 300 and 400C, and the oven system was held at over 100C for about 2 hours while the sorption pump was held at 77K. The ion pump was cooled and valve B was closed. Ion pump D was ignited and the oven temperature was raised. A thermocouple controller and a timing unit maintained a 400C environment for the desired time, usually overnight (including cooling). The system was then cooled and pumped by ion pump D to ultimate pressure.

Once a satisfactory ultimate pressure was attained, the experimental tube was heater-taped and, with the tube walls hot, the emitter (and the diaphragm collector, when possible) was gradually heated during pumping with ion pump D. The rate of temperature increase was controlled, keeping the tube pressure on the 10^{-7} or 10^{-6} Torr scale. Both the collector and the emitter were thoroughly outgassed, and the emitter was finally raised to a temperature at which a thin film of the emitter material was vaporized onto the tube walls if it was a low-melting-point material (nonrefractory) or, if it was a refractory material, to a temperature equal to or greater than any anticipated for the electron and ion emission measurements. The entire system was baked at 300C with the emitter hot for 1 hour. The emitter, collector, and tube walls were then cooled, the bakeable valve C was closed, and the system was pumped to ultimate pressure, which was usually $\leq 10^{-9}$ Torr. At this point, vacuum work function thermionic emission measurements were made.

Following the completion of vacuum work function measurements, the cesium was released by rf heating of cesium chromate pellets in arm H. The cesium was distilled into the reservoir I and the arm H

was pinched off at J. The system was pumped to ultimate pressure by ion pump D. The tube was pinched off from the vacuum station at K. The cesium reservoir nipple was placed in an ice bath, and the remainder of the tube was heater-taped and baked at about 150C until all of the cesium had condensed in the ice bath. The ion pump was then untaped and ignited while the remainder of the tube was kept heated and the cesium reservoir was kept cooled. When ultimate pressure was reached, the remainder of the tube was cooled to room temperature. With the cesium reservoir still at 0C, ion pumping was continued until ultimate pressure was achieved, which was usually in the upper 10^{-9} Torr range, in the presence of cesium.

The emitter was then heated slowly to maximum operating temperature with the ion pump operating. The emitter was kept hot until ultimate pressure was reached, and cooling followed. Ultimate pressure was again attained, and the tube was immediately mounted in the temperature bath for cesiated emission measurements. Prior to the cesiated emission measurements, the tube was pumped with the cesium reservoir between room and ice bath temperature. For the iron tube the pressure fell quickly to the 10^{-8} Torr scale and pumped within a few minutes to an ultimate pressure between 7 and 8 x 10^{-9} Torr. The iron tube was typical of the average tube, although it was not the cleanest nor the lowest pressure tube. For example, the corresponding pressure in the chromium tube was 3 x 10^{-10} Torr. The ion pump was ignited between data runs with the emitter hot and cold. It was found that the ion pump could be operated during emission measurements at the lower bath temperatures (4, 15, and 30C) with no influence on the data.

SECTION IV

EXPERIMENTAL RESULTS

The materials for which one or more experimental tubes were fabricated and for which measurements were performed under this contract were (1) iron (Fe), (2) chromium (Cr), (3) molybdenum (Mo), (4) molybdenum disilicide ($MoSi_2$), (5) alumina (Al_2O_3), (6) tantalum diboride (TaB_2), and (7) beryllium (Be). Complete data were obtained for the first five of these, and only partial success was attained for (6) and (7), for reasons described below.

Prior to the initiation of this contract, some preliminary results were obtained for copper, tungsten, platinum, and stainless steel; these were partially reported in Progress Report No. 1. These four materials will all be studied more thoroughly under the superior vacuum conditions described in this report, and will be reported under Contract NAS 3-6278. Some of the preliminary data for copper will be included here to aid in comparisons among materials. The data for copper are to be considered preliminary and subject to change.

The experimental data obtained in this research program are described below by material, in sections broken down by the type of measurement.

A. VACUUM WORK FUNCTIONS AND DESCRIPTIONS OF EMITTERS

All of the data presented below for effective vacuum work functions and the cesiated electron emission S curves are for the condition of zero applied electric field, unless otherwise specified, as in the section on the effects of applied field. "Effective thermionic work function" means that the value of A in the Richardson equation is always taken as 120.4 A/cm^2-K^2, and any observed variation in the measured work function is reported as a temperature dependence in the work function,

by a positive or a negative temperature coefficient. This is in contrast to quoting a Richardson work function and a Richardson A value either greater than or less than 120.4 (corresponding to positive and negative temperature coefficients).

The effective vacuum work function data were obtained by measuring and plotting the electron current density from zero to at least 3000 V/cm, and sometimes to almost 10^5 V/cm, and extrapolating the data to zero applied field through the Schottky region. The influence of the applied field is discussed in more detail in a later section.

Copper

A copper emitter was investigated prior to the start of this contract. The vacuum conditions were inferior to those used for the contract work, and the techniques for obtaining data had not been developed to the degree used on the contract. The results are reported here for completeness, but should be treated as tentative and subject to change when results for copper are obtained under Contract NAS 3-6278.

A high purity, oxygen-free, indirectly heated copper emitter, a 0.002-in. copper aperture collector, and a copper cup were used in the fabrication of an experimental tube. Prior to enveloping, the emitter was processed at about 840C for 20 min. After being sealed onto the vacuum station, the emitter was held at each of a series of successively increasing temperatures from 800 to 960C in the absence of cesium. During this time, a thin film of copper was vaporized onto the glass walls under high vacuum, probably guaranteeing an initially clean surface. Electron emission curves were obtained at a series of surface temperatures between the lower limit, where steady emission currents could be measured, and the upper limit of 100C below the melting point of the copper emitter. The tube pressure at surface temperatures of 800, 850, 900, and 950C were 5×10^{-8}, 7×10^{-8}, 2×10^{-7}, and 9×10^{-7} Torr, respectively. These pressures are to be expected when the vapor pressure of copper at these temperatures is considered. The emission

currents were so low at temperatures up to 100C below the melting point that the current in the cup collector circuit could not be accurately measured (less than 10^{-13} A). However, the current in the diaphragm circuit could be read in the temperature range from 750 to 960C for higher applied voltages. Zero-field current extrapolations could be made only in the temperature range 850 to 960C, corresponding to a total collected current in the range 10^{-13} to 10^{-10} A. Five zero-field extrapolation data points for the first copper tube studied, and four for a second tube, were obtained in this range and are shown plotted in Fig. 7. An effective vacuum work function of 4.49 ±0.02 eV for copper between 1100 and 1250K is indicated, with the possibility of a small positive temperature coefficient. This value is in agreement with published values for copper.

Molybdenum

The effective vacuum work functions of four different 0.002-in. thick polycrystalline molybdenum ribbon emitters which were subjected to rigorous processing, including multiple bakeouts before and after degassing of the emitter, were measured carefully and found to have reproducible negative temperature coefficients. Three were processed at 2250K and one at 2050K. Those processed at the higher temperature exhibited a tendency to become brittle and crack through the point where the thermocouple was spot welded. Evidence of significant grain (or single crystal) growth was apparent in these three. The fourth ribbon retained its strength and was used to obtain the electron S curves. The diaphragm collector was degassed by electron bombardment heating by a 100 mA/cm^2 current of 1500 V electrons. The collector was held at about 1200C for several minutes and up to nearly 2000C for a few seconds. This was followed by another thorough overnight bakeout of the tube and system at 350C. The final ambient background pressure (emitter cold) was below 1 x 10^{-9} Torr. The tube was pumped during the bare work function measurements by both the main 1-liter/sec and the 0.2-liter/sec appendage ion pumps. The working pressure remained on

o TANTALUM DIBORIDE (Ta B$_2$): 5.16 ± 0.07

● ALUMINA (Aℓ_2O$_3$): 4.91 ± 0.02

□ MOLYBDENUM SILICIDE (MoSi$_2$ + POSSIBLY SOME Mo$_5$Si$_3$)

■ COPPER: 4.485 ± 0.02

△ MOLYBDENUM (PROCESSED AT 2050 °K) 4.61 − 2.21 × 10^{-4} T

▲ MOLYBDENUM (PROCESSED AT 2250 °K) 4.33 − 1.52 × 10^{-4} T ± 0.04

x TANTALUM CARBIDE AND POSSIBLY TANTALUM: 3.32 + 5.2 × 10^{-4} T ± 0.02

● CHROMIUM: 3.90 ± 0.03
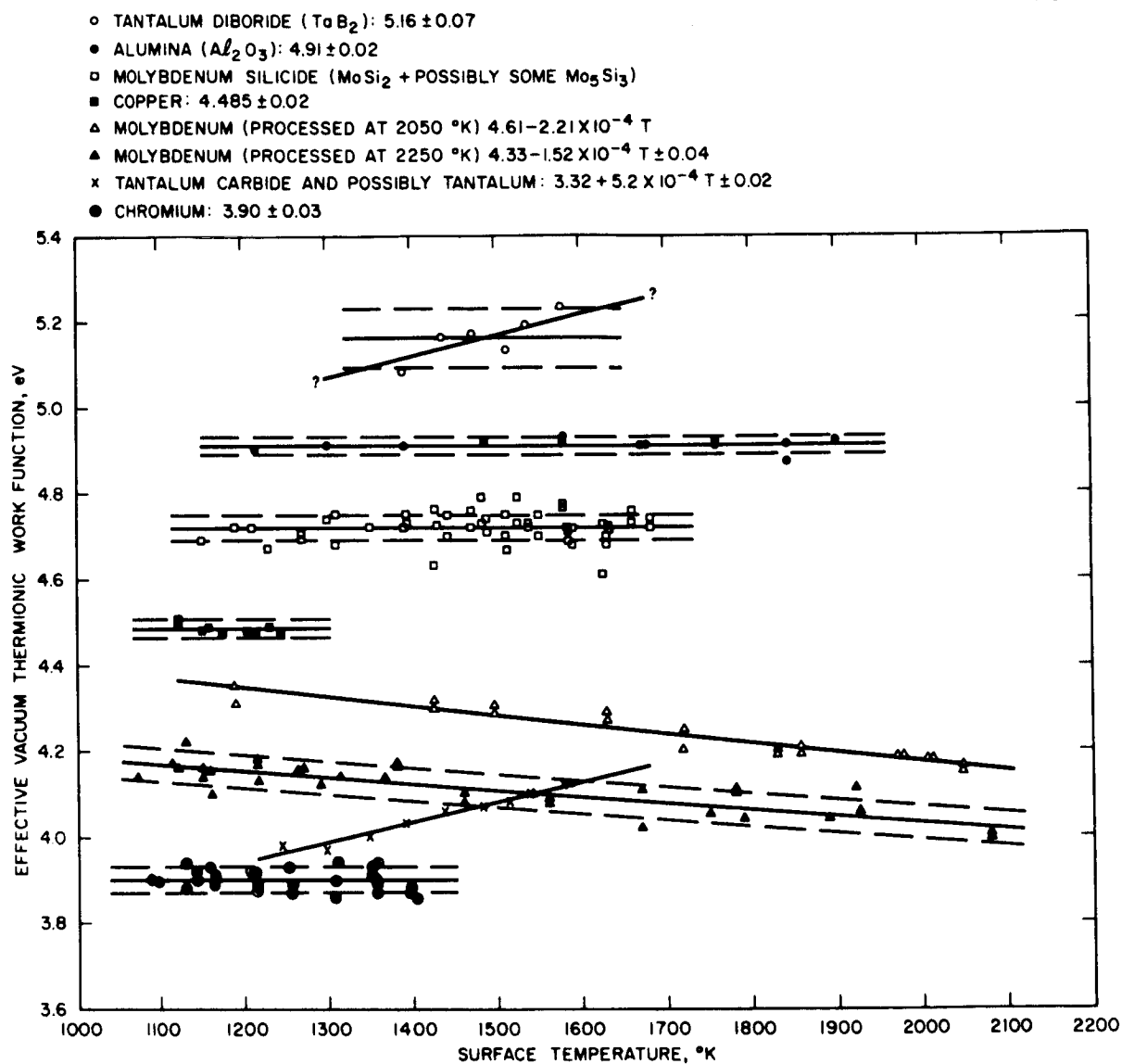
Fig. 7. Zero-field extrapolated vacuum thermionic work function data for various polycrystalline surfaces.

the 10^{-9} Torr scale until the emitter reached elevated temperatures, when it was observed to lag the vapor pressure, corresponding to the measured emitter temperature, by one or two orders of magnitude. A total of about 40 zero-field extrapolated effective work function measurements were obtained for the three molybdenum emitters processed at 2250K and are plotted as a function of temperature in Fig. 7. The measurements were made in the temperature range 1050 to 2100K. Ninety percent of the 40 data points fall within about 0.04 eV of the straight line expressed by the equation

$$\phi(T) = 4.33 - 1.52 \times 10^{-4} \, T(K) \text{ eV},$$

which gives 4.12 eV at 1400K and 4.03 at 2000K. Twenty data points for the fourth ribbon processed at only 2050K are also plotted in Fig. 7. A higher work function is observed, again with a negative temperature coefficient, expressed by the equation

$$\phi(T) = 4.61 - 2.21 \times 10^{-4} \, T(K) \text{ eV},$$

which gives 4.30 eV at 1400K and 4.17 eV at 2000K. These values are all in satisfactory agreement with values for polycrystalline molybdenum reported in the literature. The negative temperature coefficient was reproducible for individual ribbons and among all four different emitters. The difference in the work functions observed between the two differently processed molybdenum ribbons is postulated to be caused by the preferential growth of a lower work function crystal face in the ribbons processed at the higher temperature (crystal growth was evident).

Chromium

An experimental tube was fabricated with an indirectly heated chromium emitter and a chromium collector. The emitter was formed by machining two opposing flat surfaces on a 99.99% pure polycrystalline chromium tubule. The diaphragm collector was constructed by plating a

0.010-in. copper foil with about 0.003 in. of chromium on the side facing
the emitter. A 0.010-in. diameter hole was then drilled for the collector
cup aperture, and the copper was removed in the vicinity of the hole edge.
The emitter face and the large planar chromium collector were separated
by 1 mm. The 0.003-in. tungsten-rhenium thermocouple was spot welded
on the identical rear surface of the emitter in line with the aperture in
the diaphragm collector. The temperature of this indirectly heated emit-
ter was observed to be very uniform over the entire surface.

The tube was processed by baking overnight at 400C, followed by
degassing of the emitter to a temperature ($\sim$ 1500K) at which a film of
chromium was deposited on the tube wall. The diaphragm collector sur-
face could not be degassed because the copper backing would not allow
heating by passing current through it, and the emitter could not be heated
sufficiently (because of vaporization) to allow a sufficient current density
of high energy electrons for bombardment of the collector. Its surface
did appear visually to be a bright plated chromium surface. Emitter de-
gassing was followed by another overnight bakeout at 400C. The pres-
sure, as measured by either of the two ion pump currents, was the low-
est observed with the system, so low that the current was very near the
background current measured with the pump magnet removed. Back-
ground and pump currents were carefully measured with the battery-
operated electrometer, and the difference in the readings (with and
without the magnet) corresponded to 3×10^{-10} Torr in the system. Be-
cause of the high vapor pressure of chromium (1100K $\sim 6 \times 10^{-9}$,
1300K $\sim 4 \times 10^{-6}$, and 1500K $\sim 5 \times 10^{-4}$ Torr), an upper limit of about
1400K (5×10^{-5} Torr) was placed on the emitter temperature.

An interesting pressure phenomenon which was not noticed for
any other surface studied was observed with the chromium tube. For
most materials (molybdenum serving as a good example), the pressure,
measured by the ion pumps, increased monotonically with increasing
emitter temperature to the limit imposed by vaporization, or the arbi-
trary limit of about 2000C. Several other materials have been observed
to vaporize and deposit on the tube walls, but always with increasing

pressure. For chromium, a different effect was noted; the pressure rose slightly but consistently with increasing emitter temperature only up to about the temperature at which a noticeable film of chromium was evaporated onto the tube walls. With further temperature increase the pressure was observed to decrease substantially; the lowest pressure corresponded to the highest emitter temperature. This effect accounts for the unusually low pressures observed for chromium; it is inferred that a freshly or continuously deposited film of chromium is an excellent getter, at least in a glass ion-pumped vacuum chamber. Pressure which was several orders of magnitude better was obtained in this case while the emitter surface was hot. The maximum chromium temperature was only 1100C, of course, compared with 2000C for molybdenum, but the corresponding chromium vapor pressure is greater than that for molybdenum, and the pressure did decrease substantially.

The effective vacuum work function was measured for the first chromium tube at seven temperatures between 1100 and 1400K. The result was an unexpected 3.90 ±0.03 eV, independent of temperature in this range, as shown in Fig. 7. This value is termed "unexpected" because the values quoted in the Handbook of Physics and Chemistry[2] and the American Institute of Physics Handbook[3] are much higher — in the range 4.4 to 4.7 eV, with 4.6 the preferred value. Because of this substantial disagreement, the measurements were repeated under several different conditions and for more than one experimental tube.

A second series of measurements was made later with the first chromium tube; immediately preceding the measurements the emitter temperature was raised to a value at which a substantial layer of chromium was evaporated (at 10^{-9} Torr), thereby insuring a fresh, clean chromium surface. The first few measurements were then actually made at temperatures at which chromium was being vaporized, and the results were identical to those reported above.

Just as these measurements were completed, one of the thermocouple wires changed its position enough to contact the diaphragm collector, thereby shorting out the emitter and preventing the application of

a potential difference. Consequently, a second experimental tube was fabricated. This second tube was carefully processed like the first one, including vaporization of the emitter surface. The work function was measured at eight temperatures between 1080 and 1420K (also plotted in Fig. 7). The results were in agreement with those of the first tube, 3.90 ± 0.03 eV, with no significant temperature coefficient. It is noted that the values obtained from both the gross emitter-diaphragm current and the limited-area emitter diaphragm aperture-cup collector (normal electric and magnetic field) currents were essentially the same. It is emphasized that the only electrons which reach the collector cup should originate from the projection of the aperture onto the center of the emitter surface. Following these measurements, the tube was maintained overnight at this ultrahigh vacuum, and a single measurement was made on the following day, not preceded by any vaporization. The value obtained was 3.89 eV. This measurement included varying the applied surface electric field from small positive values to negative values above 10^4 V/cm. (These data are discussed later in the report.)

In order to aid in the substantiation of a pure chromium specimen, the emitter was removed from the first tube and was subjected to an x-ray diffraction measurement. The results of this measurement prove that the emitter was essentially randomly oriented pure chromium — to within the detection sensitivity of the instrument. The results are typical of the x-ray diffraction technique (which is used in this program enough to be discussed further) and are included here as an illustration. The d values of all of the experimentally observed diffraction lines for the first emitter are listed in Table II, together with their relative intensities. Also tabulated are the data for a powder sample of chromium, taken from a reference card file. The agreement is conclusive. All of the listed lines for random polycrystalline chromium are observed and are in very good intensity agreement. Two lines are observed which are not listed, one very weak, and one of moderate intensity. The latter line, with a d value of 0.763 and relative intensity of 17, is attributed to chromium for the following three reasons: (1) the card file tabulations generally do not list lines with d values below about 0.8; (2) the

42

TABLE II

X-Ray Diffraction Data for Chromium Emitter

Experimentally Observed Lines for First Emitter		Reference Book Listings for Chromium			Experimentally Observed Lines for Second Emitter	
d Value	Relative Intensity	d Value	Intensity	Crystal Face	d Value	Relative Intensity
(nothing greater than 2.04)						
2.04	100	2.039	100	110	2.04	100
1.44	11	1.442	16	200	1.44	1
1.18	33	1.177	29	211	1.18	3
1.02	15	1.020	17	220	1.02	1
0.91	21	0.912	21	310	0.91	20
0.868	4	-(unidentified — very weak)-				
0.83	8	0.833	6	222	0.83	1
0.763	17	-(probably chromium)-				
(no other lines with relative intensity greater than 3)						

intensity of the line dictates that it would have to be the strongest line of a different material, and it is too low to be typically a most prominent line; and (3) no material is listed in the reference card file (by d value ordering) with a most prominent d value of 0.76. The line with d value 0.860 remains unidentified; however, its intensity is so low that it may also belong to chromium, but may be unlisted in the card file because of the many stronger lines. The significant fact is that there are no higher d-value lines which do not correspond to chromium, to combine with these two lines to form a line series of a different material.

Following the cesiated emission measurements (reported later), another x-ray diffraction run was made on the chromium emitter face. The results are also included in Table III. The emitter surface is seen to have become oriented strongly in the 110 direction during the extended cesiated measurements (the 310 face also reflects the 110 orientation).

The values of the work functions reported in the literature[2,3] for the light transition metals (Groups I and II), which include chromium, are listed in Table III.

TABLE III

Transition Metal Work Functions[2,3]

Metal (Z)	Work Function, eV
Titanium (22)	4.0
Vanadium (23)	3.8 to 4.1
Chromium (24)	4.4 to 4.7
Manganese (25)	3.8
Zirconium (40)	3.7 to 4.2
Niobium (41)	3.9 to 4.0
Molybdenum (42)	4.0 to 4.2
Technetium (43)	—

The following facts are noted. The transition metals adjacent to and similar to chromium have lower work functions (3.8 to 4.1 eV); that is, the listed values for chromium are anomalously high in comparison. The work function which we measured for a polycrystalline molybdenum ribbon varies with temperature in the range from 4.0 to 4.2 eV, in good agreement with the literature. Most of the values for chromium reported in the two handbooks[2,3] were measured between 15 and 35 years ago, possibly before very pure chromium samples were available, while the sample used here is known to be of high purity (99.99% as purchased).

All of the evidence which can be offered to substantiate the claim that the work function of chromium is 3.9 eV rather than 4.6 eV is summarized below. This is a very significant difference because the results of the computer calculations performed for chromium, and for any other material, depend very strongly on this input parameter — the effective vacuum work function.

1. The original metal specimen from which the emitter was fabricated was quoted by the supplier to be 99.99% pure chromium.

2. An x-ray diffraction spectrum made on an actual machined emitter verified high purity chromium.

3. The initial pressure in the experimental tube was below 10^{-9} Torr before and during most of the vacuum work function measurements.

4. Periodically, during vacuum work function measurements (and cesiated electron and ion emission measurements), a layer of chromium was evaporated from the emitter surface.

5. Both the diaphragm and cup collectors gave the same work function value (within about 0.03 eV) over a fair range of temperature, including some while chromium was noticeably vaporizing. The same value was obtained with two experimental tubes.

6. The collector opposing the emitter surface in this investigation was also chromium, thereby guaranteeing that no material other than chromium from such a source, especially during high-energy ion emission, could form a partial monolayer on the emitter surface. The material adjacent to the chromium emitter was platinum, a high work function material.

7. The other transition metals similar to chromium (titanium, vanadium, manganese, zirconium, niobium, and molybdenum) have, without exception, low work functions (3.8 to 4.1 eV); the previously reported work function for chromium, about 4.6 eV, is not typical.

8. The values for the work function of chromium listed in the handbooks were all measured quite a number of years ago (from 15 to 35 years), possibly with specimens that were less pure than ours and under inferior vacuum conditions.

This result indicates a change in a fundamental property of a metal listed in the handbooks, and therefore has been discussed more carefully.

45

Iron

The upper limit on the temperature of the iron emitter, 1500K, was dictated by vaporization onto the glass tube walls. The vacuum work function of indirectly heated 99.99% pure iron emitters was measured in the range 1100 to 1500K on each of four different experimental emitters (sometimes twice). The results were not completely reproducible among the several measurements, and the values obtained with the diaphragm and cup collectors did not always agree within any one set of measurements. More trouble was encountered for iron in this regard than for any other material studied. All of the results are described below.

The results from the first tube gave 4.47 ± 0.05 between 1200 and 1550K, with an indication of a positive temperature coefficient or $\phi(T) = 4.05 + 3.1 \times 10^{-4} T$. For the second tube, a work function curve with a negative temperature coefficient described by the equation $\phi(T) = 4.94 - 3.1 \times 10^{-4} T$ in the range 1300K to 1500K resulted, giving 4.54 eV at 1300K, 4.50 at 1400K, and 4.47 at 1500K. These are the data combined from two separate measurements from both diaphragm and cup collectors. The best single value is 4.50 eV, independent of temperature. With the third tube, data obtained at nine temperatures from 1100K to 1500K with the diaphragm collector gave $\phi = 4.33$ eV with no observable temperature dependence. Cup collector data at the four highest temperatures gave 4.33 eV at 1500K, 4.54 eV at 1400K, and 4.60 eV at a lower temperature. A value obtained from an early S curve measurement in cesium (second tube) gave about 4.45 eV at high temperatures. Data were obtained for the fourth iron emitter at various temperatures during a processing procedure which involved heating to vaporization temperatures and subsequent cooling. The values exhibited a rather wide range from a minimum of 4.2 to a maximum of 4.6 eV, depending on the temperature history and direction of change of temperature. The cup collector tended to give higher work function values than the diaphragm collector.

The data from all four emitters fall within the range 4.2 to 4.6 eV, with about 4.47 being a favored value. Nine values are reported

in the Handbook of Chemistry and Physics[2]: 4.04, 4.23, 4.48, 4.77, 3.91, 3.92, 4.72, 4.77, and 4.40 eV (which is an even greater span). Different values were obtained in this work, depending on whether the data were obtained for increasing temperature (from 1000K) or for decreasing temperature, starting from 1500K. The possible explanation suggested to account for the unusual variations observed in this work is based on the knowledge that three stable crystallographic structures exist in pure iron: α-Fe from 300K to 1185K, γ-Fe from 1185K to 1675K, and δ-Fe above 1675K. The α and δ structures are body-centered cubic; γ is face-centered cubic. While the temperature of the samples never reached the transition point between the fcc γ and bcc δ structures, the reversible bcc α-fcc γ transition was crossed during every temperature scan. Because of the structure change between bcc α and fcc γ in the temperature range of measurement and because of the polycrystallinity of the specimen, the atom arrangement and crystal faces were changing. It is therefore postulated that the measured effective vacuum work function actually varied with temperature and with the heat treatment history of each emitter because the crystal structure and the areal percentages of the various crystal faces, each with its own work function, varied. This could account for the two unusual effects observed for iron and not for the other surfaces studied: (1) variation among samples with different heat treating histories, and (2) variation of the measured effective work function with temperature and direction of temperature change (bcc α to fcc γ versus fcc γ to bcc α) for any one sample.

Other metals studied so far (chromium, copper, molybdenum, beryllium, and tungsten) do not have these reversible structure transitions.

Beryllium

A tube base was fabricated with a beryllium emitter and diaphragm collector, both of 0.002-in. thick foil. The directly heatable,

high-purity beryllium ribbon emitter was spot welded to Kovar posts, and the 0.003-in tungsten-rhenium thermocouple was successfully spot welded to the ribbon. As the emitter was heated during the preliminary tube processing, it was evident that the 2-mil beryllium foil was sufficiently irregular in structure to cause an irregular heating pattern. Associated hot and cold spots were evident; accelerated vaporization at the hot spots during stabilization of the average temperature at a value satisfactory for the required studies resulted in thinning in the hot regions, further local heating, and finally disintegration of the ribbon after only a short test time. It was concluded that it would be necessary to fabricate an indirectly heated, machined bulk beryllium emitter to use with the same apertured beryllium foil collector. Two such emitters have been machined and will be studied under Contract NAS 3-6278.

Molybdenum Silicide

Information in the literature concerning the refractory metal compound molybdenum disilicide is somewhat contradictory and inconclusive. A predicted high work function is mentioned; experimental results show a low but time-varying work function. An activation-deactivation process is discussed which is claimed to cause the time variations in work function. A significant negative temperature coefficient for $MoSi_2$ was measured. Two facts reported in Ref. 9 should be noted. The vacuum conditions were poor, no better than 10^{-6} Torr, easily subjecting the results to question from our experience; the means of producing the specimen surface could be the cause of the activation and deactivation and time varying observations.

Molybdenum disilicide surfaces were prepared in this laboratory by W. E. McKee after a series of experiments to develop a technique which would produce a uniform surface reliably known to be pure $MoSi_2$. This was accomplished by checking the surfaces produced by x-ray diffraction in each test run; this gave the composition of the surface in terms of the various silicides of molybdenum, as well as pure molybdenum.

48

The specimens used in our experimental measurements were originally 0.002-in. thick ribbons of molybdenum, silicided to the extent that the total thickness became 0.003 in. with about 0.001 in. of pure $MoSi_2$ on each face, as measured by x-ray diffraction. These emitter specimens and larger foils of $MoSi_2$ for the diaphragm collector were used to fabricate several experimental tubes. The work function of one specimen of $MoSi_2$ was measured from the very first heating in the tube for purposes of degassing and then for several subsequent runs in which the temperature was raised briefly to 1650K and then lowered to room temperature, and finally measured periodically throughout a 10-hour run during which the specimen was maintained at 1500K. From the very first heating, through the 10-hour high temperature run, this specimen exhibited a constant effective work function of 4.72 ± 0.02 eV. The work function was measured every 2 hours (six measurements) during the 10-hour run at 1500K and found to vary no more than the 0.02 eV limit. The data from these measurements and those from two more subsequently built $MoSi_2$ tubes are all plotted in Fig. 7. The results are consistent; when combined, the measured values of effective vacuum work function fall within 4.72 ± 0.03 eV. No significant temperature coefficient is observed.

Cesium ion emission measurements were run on two different molybdenum silicide tubes and were similar to other surfaces studied. However, the electron emission measurements produced results showing some unusual effects, including temperature hysteresis. At the conclusion of the cesiated measurements, the ribbon was removed from the tube and submitted for x-ray diffraction analysis. The results were very clear; the ribbon was no longer $MoSi_2$ but almost entirely Mo_5Si_3; a trace of Mo_5Si was distinguishable among the approximately 25 Mo_5Si_3 lines. No free molybdenum and no $MoSi_2$ lines could be observed. Therefore, between the time the vacuum work function measurements were begun and the cesiated emission measurements were completed, the ribbon changed from pure $MoSi_2$ to essentially pure Mo_5Si_3. The first vacuum data are certainly for pure $MoSi_2$, and probably all vacuum

data are representative of $MoSi_2$ because only short times were spent at temperatures high enough to initiate the silicon evaporation (>~1500K) during these measurements. The silicon evaporation and subsequent stoichiometric change from $MoSi_2$ to Mo_5Si_3 should have occurred during the many high temperature (~1700K), short-duration emitter cleanings prior to each electron emission data run (increasing and decreasing temperature). As will be mentioned in the section on electron emission, the evidence indicates that the emitter surface was largely diffusing and evaporating silicon, at the high temperatures.

Tantalum Diboride

Several tantalum diboride ribbon emitters were fabricated by W. E. McKee of this laboratory, starting with a 0.005-in. tantalum ribbon. The ribbons were first carbided; a layer of tantalum was deposited and was then borided. The carbide layer under the boride surface layer prevented diffusion of the boron from the surface layer to the interior metallic tantalum, a process which was found to occur readily at a temperature too low for the desired measurements. X-ray diffraction measurements on these ribbons showed them to be of large TaB_2 stoichiometry with some small amounts of lower boron tantalum borides. However, these ribbons were observed to be extremely brittle and fragile, and it was impossible to successfully fabricate even one ribbon emitter tube from them. Consequently, a block emitter of tantalum was machined and successfully subjected to the same boriding process. Even in this case, however, the TaB_2 layer was found to be very brittle and easily flaked off from the TaC sublayer, if subjected to any mechanical strain or shock. When the experimental tube was fabricated with this emitter, some of the TaB_2 layer fell off. The diaphragm aperture was therefore off-centered (toward one end of the emitter) to be directly over an intact TaB_2 portion of the surface, and the tube was successfully completed. Thus, the aperture-cup collector faced a TaB_2 surface while the larger diaphragm collector faced a large fraction (~ 1/2) of the emitter surface which was probably tantalum carbide and tantalum.

50

The vacuum thermionic emission measurements with the two collector systems exhibited different effective work function values after emitter degassing. The data from each collector are plotted in Fig. 7. For the diaphragm collector (TaC and/or tantalum), a value varying from about 3.96 to 4.13 eV (positive temperature coefficient) over the temperature range 1250 to 1600K is indicated. For the cup collector, supposedly facing a TaB_2 surface, a general value of 5.16 ± 0.07 eV in the temperature range 1400 to 1600K is observed, with an indication again of a positive temperature coefficient. These values correspond to about four orders of magnitude difference in the electron current density from the two regions of the emitter. This tube was lost in the process of cesium release and pinchoff. Because of the poor condition of the emitter face, it was decided to rebuild the tube with a newly fabricated TaB_2 emitter and repeat the measurements. It was not possible to do this before the end of the contract period, but it is hoped that it can be done under Contract NAS 3-6278.

The original reason for studying TaB_2 was that it might be a low work function surface, and therefore may be a poor cesium-ionizing refractory surface. The preliminary vacuum thermionic work function measurements reported above indicate that it probably has a relatively high work function and therefore is probably an excellent cesium ionizer, which tentatively answers the fundamental question regarding its potential as a focus electrode candidate.

Aluminum Oxide

Pure alumina is an insulator. By pure alumina is meant thin films of aluminum oxide deposited to give a surface with a high degree of purity. Such a structure lacks the conduction electrons which are characteristic of a conductor. However, it is not necessarily a poor electron emitter, although it may have a high apparent zero-field work function. Aluminum oxide, like magnesium and beryllium oxides, is termed a hot-electron emitter (rather than thermal). These materials

are known to give self-sustained electron emission currents even at room temperature, without requiring field-emission-magnitude surface electric fields. Electrons can gain sufficient energy from internal fields, so that when they reach the surface they have sufficient energy to overcome the surface potential barrier and be emitted. They will not necessarily have the low energy characteristic of thermal electrons, but may have high energies characteristic of the internal accelerating fields. An apparent effective thermionic work function will be exhibited for an insulator if the zero-field extrapolated electron emission currents are greater than zero and increase with temperature.

For the emitter geometry used here, the accelerating potential was applied between the collector and the tungsten heater wires passing through the alumina emitter. The tungsten wires, of course, were sources of thermionic electrons. If the surface of the alumina was not contaminated and was truly an insulator, the electric field lines penetrated the emitter and terminated on the surface of the central conductor, the tungsten wire. If the surface of bulk alumina loses its properties as an insulator and becomes a semiconductor at the elevated temperatures characteristic of thermionic emission, the field lines may have terminated there. Also, if sufficient impurities or surface contamination existed in the bulk alumina, the same may have occurred.

Unfortunately, bulk alumina available commercially in specific forms commonly used for electrical insulators is probably not pure enough to be the perfect insulator described above. Binders used in fabrication are probably the primary source of impurities. The purest material is probably sapphire rod, but it is difficult to fabricate into delicate electrode shapes. The emitter used in these measurements was a high purity (> 99%) machined alumina piece (AP 35) degassed at 2000K for a long time, sufficient to drive off bulk impurities and result in an ambient pressure in the 10^{-9} Torr range. Previous measurements made by H. L. Garvin of this laboratory in another vacuum environment indicated that an apparent thermionic work function of about 5 eV would be observed. The dependence of the emission on the applied field was not

previously known, but it was not necessarily expected to be similar to that for a conductor; in fact, it was not for the large diaphragm collector, although it was for the aperture-cup collector.

The thin diaphragm collector with aperture could not be fabricated from the nonconducting alumina. Therefore, a 2-mil copper foil was used with the standard 10-mil aperture. Copper was selected because any copper sputtered back onto the hot alumina emitter should quickly evaporate and not contaminate the surface. It is possible that, at lower surface temperatures, as in cesiated electron emission measurements, the surface might be influenced by the presence of sputtered copper.

A round hole was drilled in the rear face of the emitter, and a 3-mil tungsten-rhenium thermocouple was pushed flush against the hole bottom by a second smaller alumina rod. The alumina emitter was cleaned by a high-velocity spray of fine alumina powder just prior to tube enveloping.

The tube was vacuum processed and the emitter degassed at a temperature of about 1800C. A series of temperature measurements was performed employing an optical pyrometer and the imbedded thermo-couple because it was expected that the thermocouple would register lower than the true surface temperature, because it could not be welded to the emitter, as in the standard procedure. In addition, alumina is not totally opaque and was expected to transmit some radiation from the central hotter tungsten wires. Therefore, a careful series of compara-tive measurements was made in which the thermocouple readings and pyrometer readings (at the center of the alumina emitter, at the edge of the emitter where the tungsten wire could not be "seen" by the instru-ment, and at the center of the emitter as the tungsten wire was abruptly cooled by stopping the heating current) were taken at a series of tem-perature from 750 to 1800C. The pyrometer brightness temperatures were corrected for the glass and for emissivity from a curve in the literature, which includes a significant variation with temperature.

As was expected, the thermocouple indicated temperatures lower than the corrected pyrometer readings. The central reading with the pyrometer was only slightly higher than the edge reading, and the central-heater-out readings agreed reasonably well with the edge readings, although the accuracy of this technique was low because of the over-all cooling. A curve of corrected true temperature read with the pyrometer at the edge of the emitter versus the thermocouple readings was plotted and used to correct the thermocouple readings, which were then used in all subsequent experiments to drive one axis of the X-Y recorder in making the continuous temperature electron and ion emission plots.

Vacuum electron emission currents were easily observed, and measurements were made at nine temperatures between 1200 and 2000K. The currents collected by the diaphragm collector were found to be more field dependent than those for the metal emitters. That is, they increased more rapidly with increasing field. The currents passing through the aperture and collected by the cup collector did not increase with increasing field, not unlike most metal emitters. The cup currents were easily extrapolated to zero field. The diaphragm currents were plotted on Schottky plots and found to exhibit a very complex structure, which is described here in some detail because it is not fully understood; no attempt is made to interpret this structure.

In all nine cases, data were obtained to 10^4 V/cm. On the Schottky plots, all curves exhibited two straight line segments which have virtual extrapolations (i.e., they intersected the electric field axis at zero current rather than vice versa). The "zero-current-density" extrapolations had two values of electric field; one between 90 and 160 V/cm, and one spread around 1000 V/cm. In the region between about 100 V/cm and zero applied field, one of two characteristic dependences was observed; either a segment of constant current with varying field occurred, or a curve of decreasing current with decreasing field but which was not a good straight line on the Schottky plot exhibited a greater-than-zero-field-extrapolation on the current density axis.

If the current density value in the flat portion of the curve, when it occurred, or the zero-field extrapolation when a flat portion did not occur, was plotted on the work function plot, it was found that these points fell on the same work function line as the zero-field extrapolated values for the cup collector which are assumed, as usual, to give the most accurate value.

The work function as measured at nine temperatures between 1200 and 2000K was a constant 4.91 ± 0.02 eV, independent of temperature. While the work function corresponding to actual electron emission current densities measured at large applied electric fields did not decrease for the cup collector, it did decrease significantly for the large planar diaphragm collector. This observation is unexplained, but the magnitude can be reported. The work function corresponding to actual emission at 10^3 V/cm was a bit under 4.5 eV, corresponding to a decrease of over 0.4 eV.

At these temperatures, the surface of the alumina should be clean. Any impurities which were once present as a result of any binder should be gone. Even if some surface contamination were present, it would have to receive its electron supply from or through the alumina. It is assumed that the emitted electrons have their origin within the alumina, or even from the tungsten heater wire. They must escape the potential barrier at the alumina surface, however. The resulting apparent work function is high, but not as high as that of some metals. The possibility of some surface contamination cannot be ruled out, although it seems unlikely.

A better basic measurement would require heating by some means which cannot supply electrons to the alumina. However, the heating technique used here and the measurements made are practical because any application of alumina as an ion engine focus electrode would probably have the alumina in contact with the tungsten emitter, but in the presence of an applied field which would prevent any electron emission in any case.

After the cesiated emission measurements were completed on the alumina tube, it was broken open and the emitter and collector surfaces were examined. The emitter surface exhibited the same clean bright chalk white color as when enveloped, following the final cleaning by a blast of high velocity alumina dust. An x-ray diffraction analysis showed the sample to be pure alpha alumina. Examination of both collector surfaces (apertured diaphragm and cup) under a microscope revealed similar irregular surfaces best described as having the appearance of a rough sea observed from a high altitude. This roughness is assumed to be caused by cesium ion sputtering. The cup collector was very shiny, but the diaphragm had some darkened flakes in the region around the aperture. Some deposits of alumina also were clearly observable directly opposite the emitter on the diaphragm collector. The emitter temperature was frequently taken to 2000K during emission measurements, and on several occasions it probably reached 2100K or more.

B.   CESIUM ION EMISSION AND CRITICAL TEMPERATURES

Figures 8 through 13 (and Figs. 14 and 22 through 24) show cesium ion emission data for molybdenum, molybdenum silicide, copper, iron, chromium, and aluminum oxide, plotted as ion current density versus reciprocal absolute temperature. The critical temperature envelopes are obtained by drawing a curve through the saturation current density knees of such plots. In some figures, the ion current densities corresponding to the cesium arrival fluxes associated with the particular bath temperatures are indicated along the ordinate. Data are shown in general for cesium arrival fluxes in the range of 10^{13} to 10^{17} atoms/cm^2-sec. The upper limit is imposed by the initiation of cesium discharge conditions above about 6×10^{16} atoms/cm^2-sec in the presence of the high applied potentials. In order to obtain data for higher cesium pressures, a different experimental technique (such as the plasma anode technique employed by J. M. Houston) is required. However, 6×10^{16}

atoms/cm^2-sec is sufficiently higher than the actual cesium fluxes incident on the electrodes in a cesium ion thrustor that data at higher arrival fluxes are unnecessary for this specific application.

Data for molybdenum are given in Fig. 8. Those data obtained in this work are shown as solid lines. The dashed lines are data obtained by H. L. Garvin of this laboratory in a similar measurement, but with slightly different techniques. Figure 9 is a plot of the critical temperature envelope points taken from Fig. 8. Temperature hysteresis and adsorption structure are shown in the solid line recorder traces in Fig. 8.

Figure 10 shows the cesium ion critical temperature data for molybdenum silicide, including one typical full curve to show the shape of the ion current trace, the temperature hysteresis, and the adsorption structure. For molybdenum silicide, the temperature hysteresis[*] is observed to decrease with increasing current density until it disappears at about 10 mA/cm^2. The temperature hysteresis is about 110K at a current density of 1 μA/cm^2. The slopes of the ascending and descending critical temperature envelopes, as drawn, yield 2.62 and 1.79 eV/atom,[*] respectively, for the ion desorption energies at the respective critical coverages. The critical coverage for descending temperature is assumed to be slightly larger than for ascending temperature.

Curves of cesium ion current density versus surface temperature for copper were obtained for a series of cesium arrival fluxes from 9 x 10^{12} to 6 x 10^{15} atoms/cm^2-sec. Higher arrival flux measurements could not be safely made because of the nearness of the copper melting point. A critical temperature envelope drawn through the critical point is included in a later figure (Fig. 14). A data curve for one arrival flux can be seen in another later figure (Fig. 24). The ionization efficiency for cesium on copper was essentially unity up to the highest arrival flux measured, within the accuracy of the measurements. A successful special effort was made to obtain a low flux measurement at a cesium vapor temperature of -11C by the use of alcohol and solid CO_2. A similar

---

[*]Note added in proof: Data discussed elsewhere in this report indicate the possibility that the data for decreasing temperature are actually the critical temperature envelope and ion desorption energy for silicon.
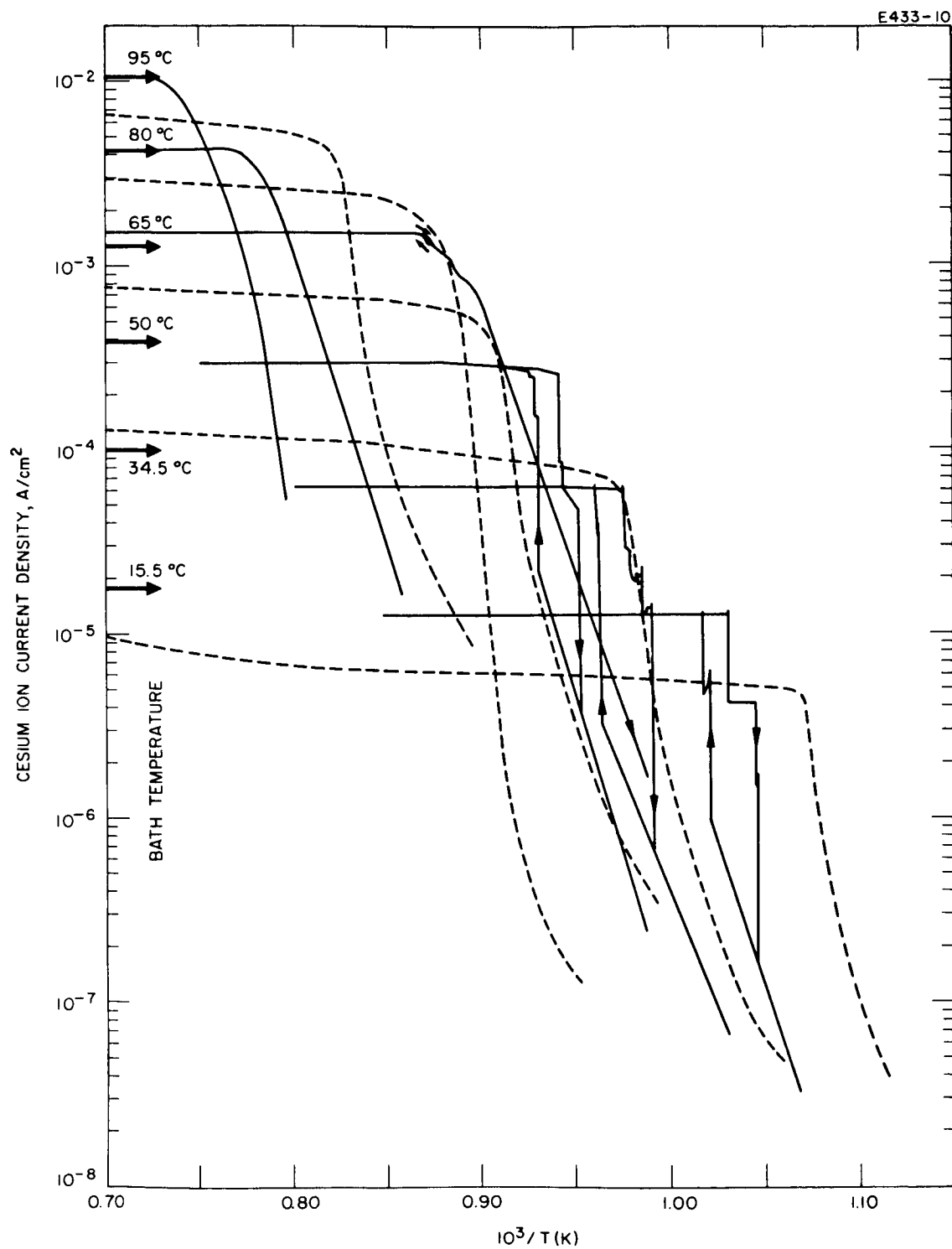
E433-10

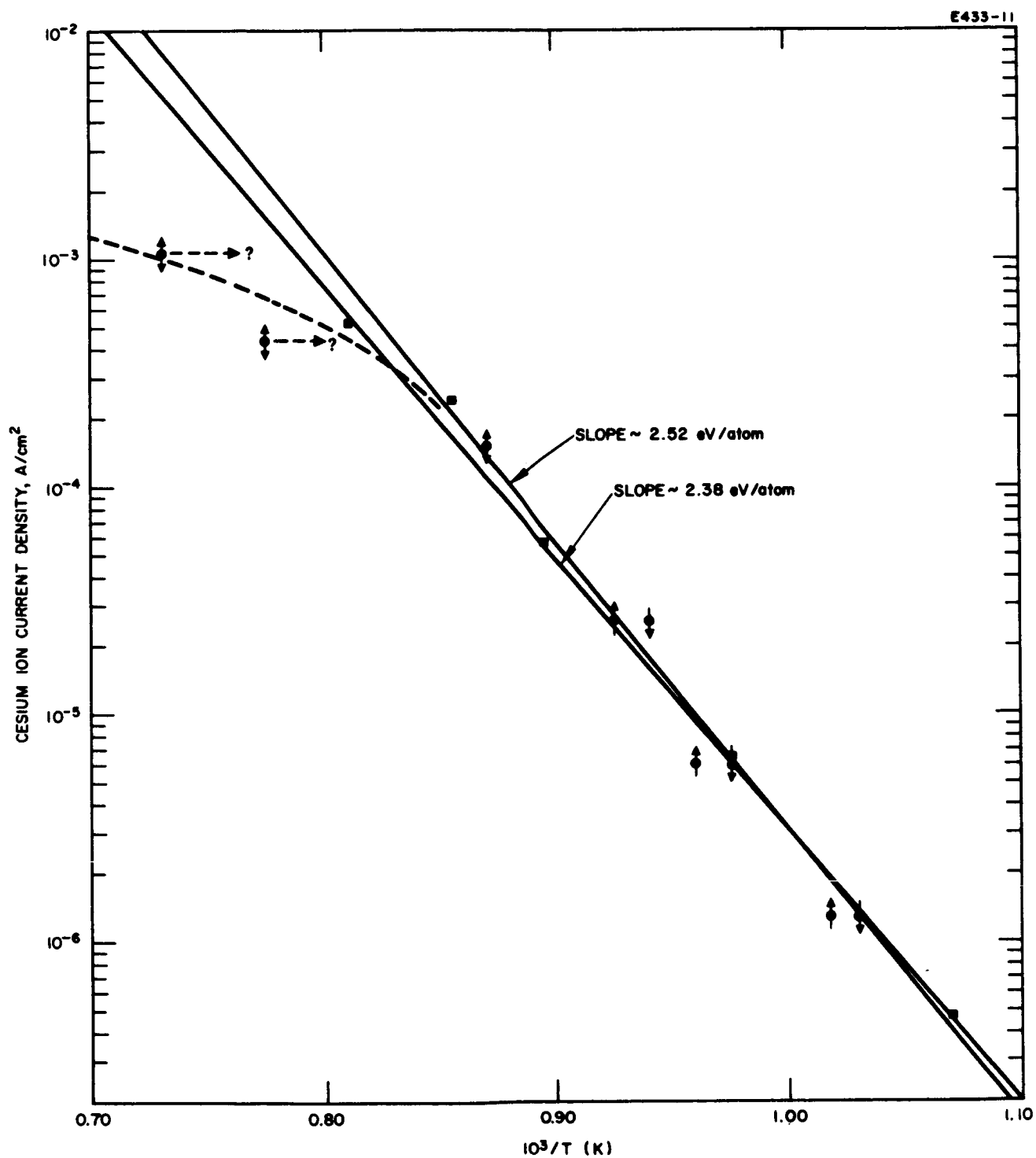Fig. 8. Cesium ion emission data for molybdenum.

58

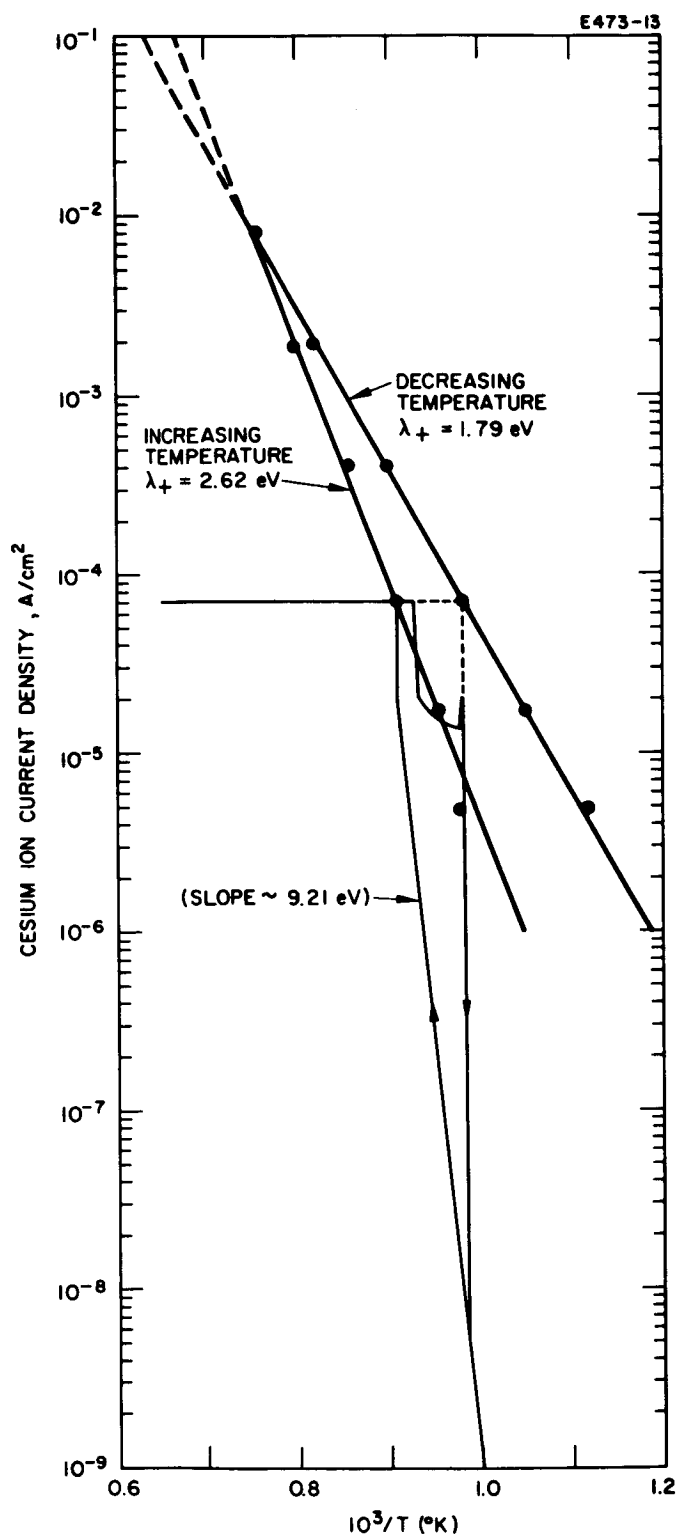Fig. 9.   Cesium ionization critical temperature envelope for molybdenum.

Fig. 10.
Cesium ion emission data
for molybdenum silicide.

attempt at -20C failed to produce current emission greater than leakage or background currents.

Cesium ion emission data for three different iron emitters are combined in Fig. 11. The data for all cesium arrival fluxes on all three experimental tubes fell close together and have been averaged into the single curve A of Fig. 11. Only one exception was observed (shown as curve B in Fig. 11); it was the first cesiated data curve obtained for one of the three tubes. It displays more "normal" emission characteristics — an exponential region at more usual current densities, followed by a saturation current density at about the correct value calculated from the cesium arrival flux (5.0×10^{14} atoms/cm^2-sec), following a small characteristic sharp rise to saturation. Such a curve was never again obtainable after the iron emitter was raised to high temperature in the presence of cesium, even immediately following vaporization of the iron surface at high temperature. There are a large number of data, over three orders of magnitude in cesium arrival flux, on three different iron tubes to substantiate curve A of Fig. 11, which indicates that iron, once heated in a cesium atmosphere, is an extremely poor cesium ionizer. An x-ray diffraction analysis, made on the iron emitter after the cesiated measurements were completed, indicated pure iron.

The ion emission data of curve A (Fig. 11) are consistent with the electron emission data for iron described in a later section. There, the cesiated electron emission data for temperatures above those for which all adsorbed cesium should be desorbed and the work function of "clean" iron should be exhibited, correspond, rather, to a work function of 3.5 eV for all three iron emitters. The vacuum work functions measured for all three iron emitters were about 4.5 eV. A work function of 3.5 eV is below the ionization potential of cesium. Therefore, a low ionization efficiency and low cesium ion current density would be expected, at best. Even when maximum ionization efficiency is attained and saturation ion current density exhibited, the cesium coverage may be 0.02 or 0.03, resulting in a work function depression of several tenths of an electron volt. For a 3.5 eV clean surface plus a cesium coverage which depresses the work function 0.3 eV, the ionization efficiency,
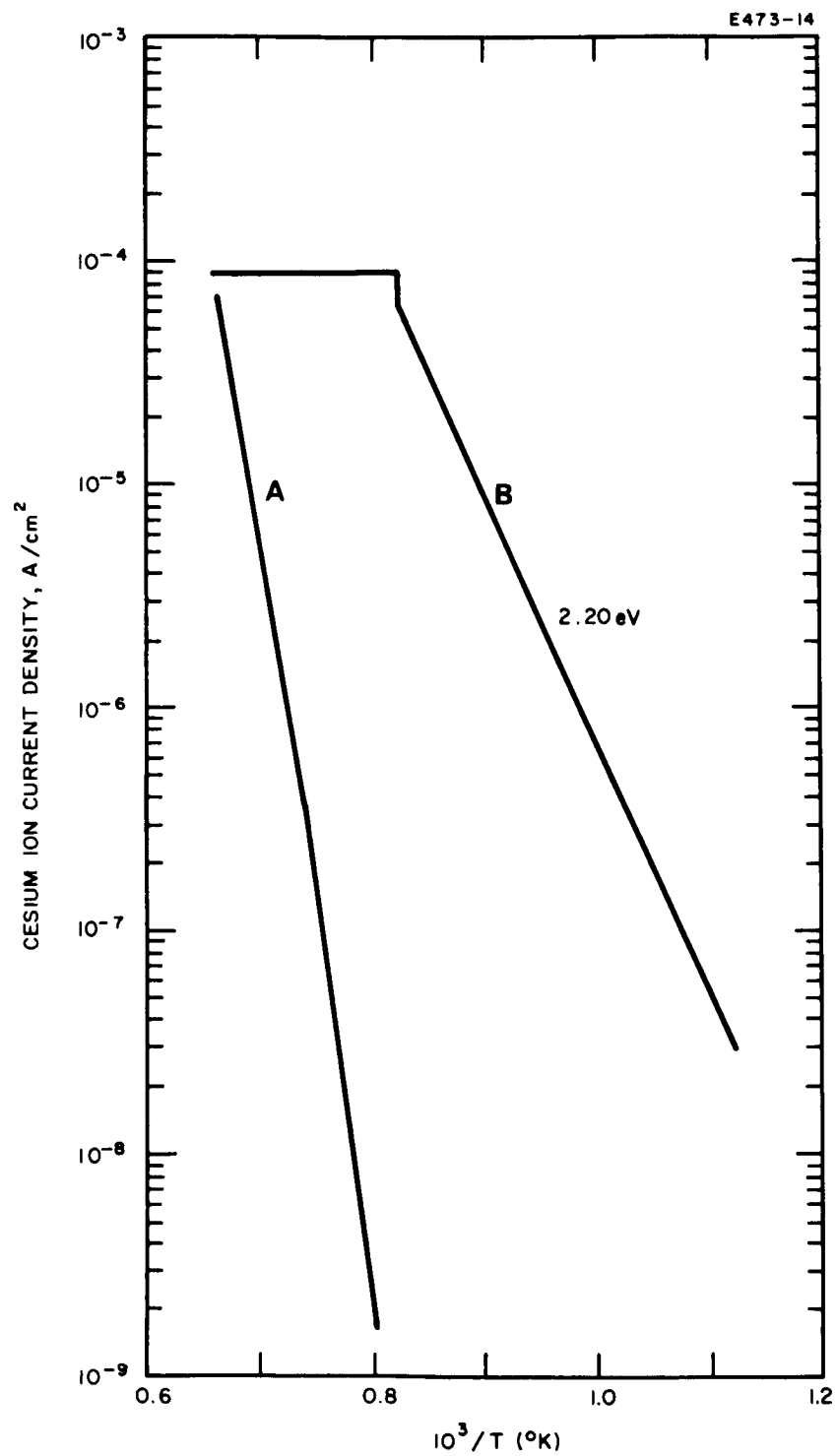
Fig. 11. Cesium ion emission data for iron.

from the Saha equation, is 5×10^{-4}. Higher coverages must exist before saturation and minimum coverage are reached; therefore, the ionization efficiency for the iron surfaces studied is below 5×10^{-4}, possibly a great deal, resulting in the very low ion current densities observed.

No cesium-iron chemical combinations or alloys are known to exist. The solubility of cesium in iron is known to be extremely low, if not zero. The only explanation for the observation of the 3.5 eV work function of "clean" iron in the presence of cesium (for three tubes and for both electron and ion emission) is the possibility that oxygen atoms diffuse onto the iron surface from the bulk iron at elevated temperatures each time the iron is heated and act as binding centers for cesium atoms, which then reduce the composite surface work function. The oxygen atoms may exist in the originally 99.999% pure iron emitter or may be adsorbed and dissolved during tube fabrication, but cannot be driven out by the processing temperature which is limited to about 1550K. Substantiating this hypothesis is the experimental information that the desorption energy for cesium ions, obtained from the slope of curve A in Fig. 11, is about 6 eV. A reversible crystallographic structure change occurs in iron in the temperature range dealt with here (see discussion of iron in Section IV-A).

The cesium ion emission curves for chromium are shown in Fig. 12. The solid lines comprise a complete set of data for one emitter. The two dashed curves were obtained with a different chromium emitter and experimental tube. Rather short critical temperature breaks are characteristic of chromium. The critical temperatures are slightly higher than the corresponding ones for tungsten. The cesium ion desorption energy obtained from the slope of the critical temperature envelope is 3.28 eV. There is some rather unusually high ion emission at low temperatures (seen in Fig. 12) for the higher arrival fluxes, which increases with increasing arrival flux.
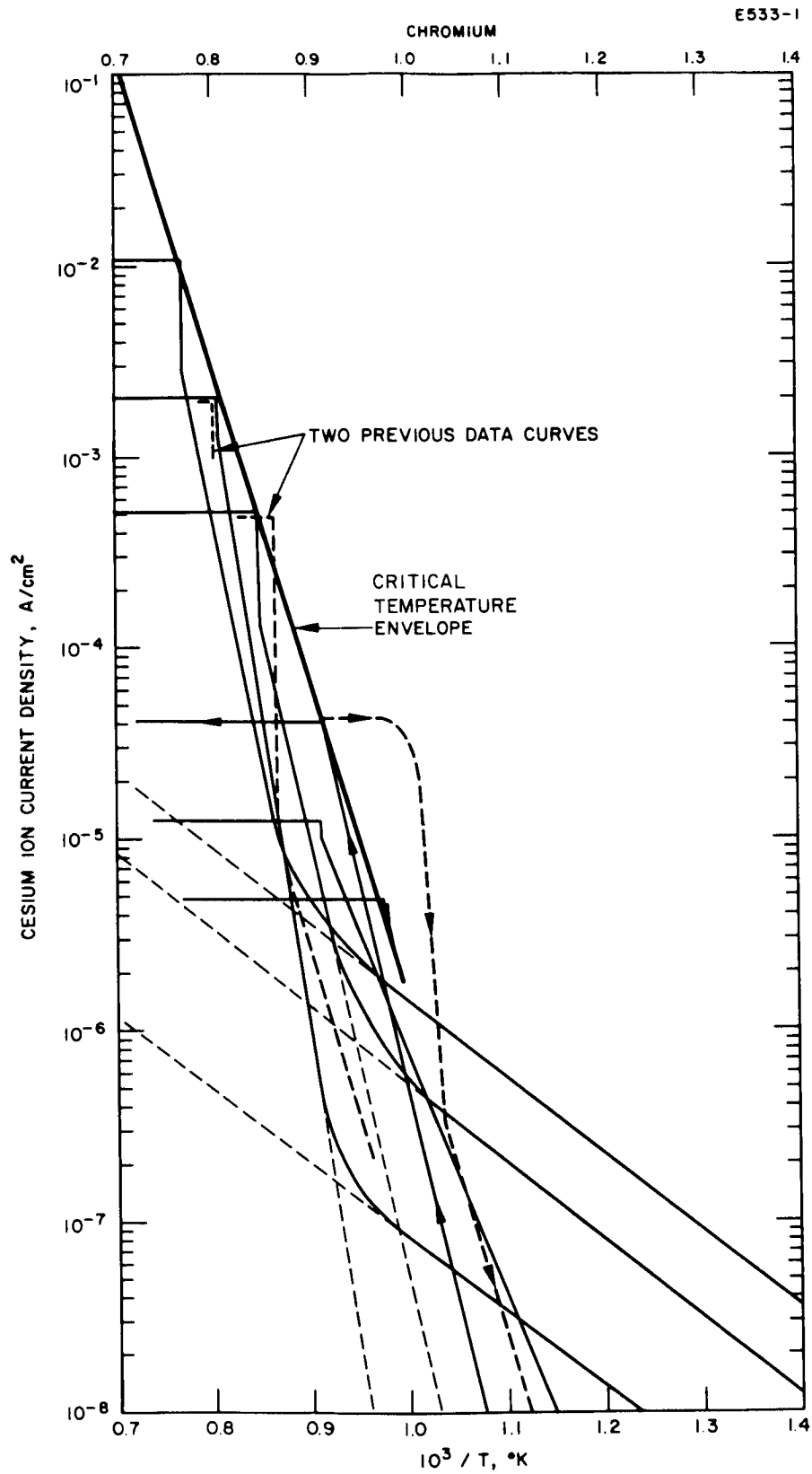
Fig. 12. Cesium ion emission from chromium.

The data for aluminum oxide are displayed in Fig. 13. Again the curves for various arrival fluxes fall on the same line, which also becomes the critical temperature envelope. A more significant "roll-over" occurs, increasing with increasing arrival flux. Some irregularity is seen in the curves at lower arrival fluxes. No sharp breaks to saturation occur, and the emission level is fairly low everywhere. Alumina is an insulator at low temperatures. However, the applied field lines may have terminated on a central conductor (the tungsten heater wire). It is uncertain where the cesium electrons go upon ionization at the surface.

C. CESIUM ION DESORPTION ENERGIES

The cesium ion current density versus surface temperature data measured with cesium arrival flux as a parameter, from which the critical temperature envelopes for the surface ionization of cesium are obtained, also provide the information required to calculate an experimentally measured value of the ion desorption energy at the critical coverage. This critical coverage value is small, of the order of a few hundredths of a monolayer. Therefore, the measured desorption energy is for very small surface coverage.

If the envelope of critical temperatures is a straight line on a plot of $\log J_+$ versus $1/T$, the slope of the line can be used to calculate $\lambda_+(\theta_c)$, or the tangent to the envelope at any point can be similarly used. This technique has been employed here to calculate experimental values of $\lambda_+(\theta_c)$ for the various substrates studied. $\lambda_+(\theta_c)$ is obtained from the expression

$$\lambda_+(\theta_c) = 0.862 \times 10^{-4} \frac{\ln J_{+_1}/J_{+_2}}{1/T_{c_2} - 1/T_{c_1}} \text{ eV} \qquad (2)$$

where (J_{+_1}, T_{c_1}) and (J_{+_2}, T_{c_2}) are the coordinates of two points on the critical temperature envelope and 0.862×10^{-4} is just the Boltzmann constant in electron volts per degree Kelvin.
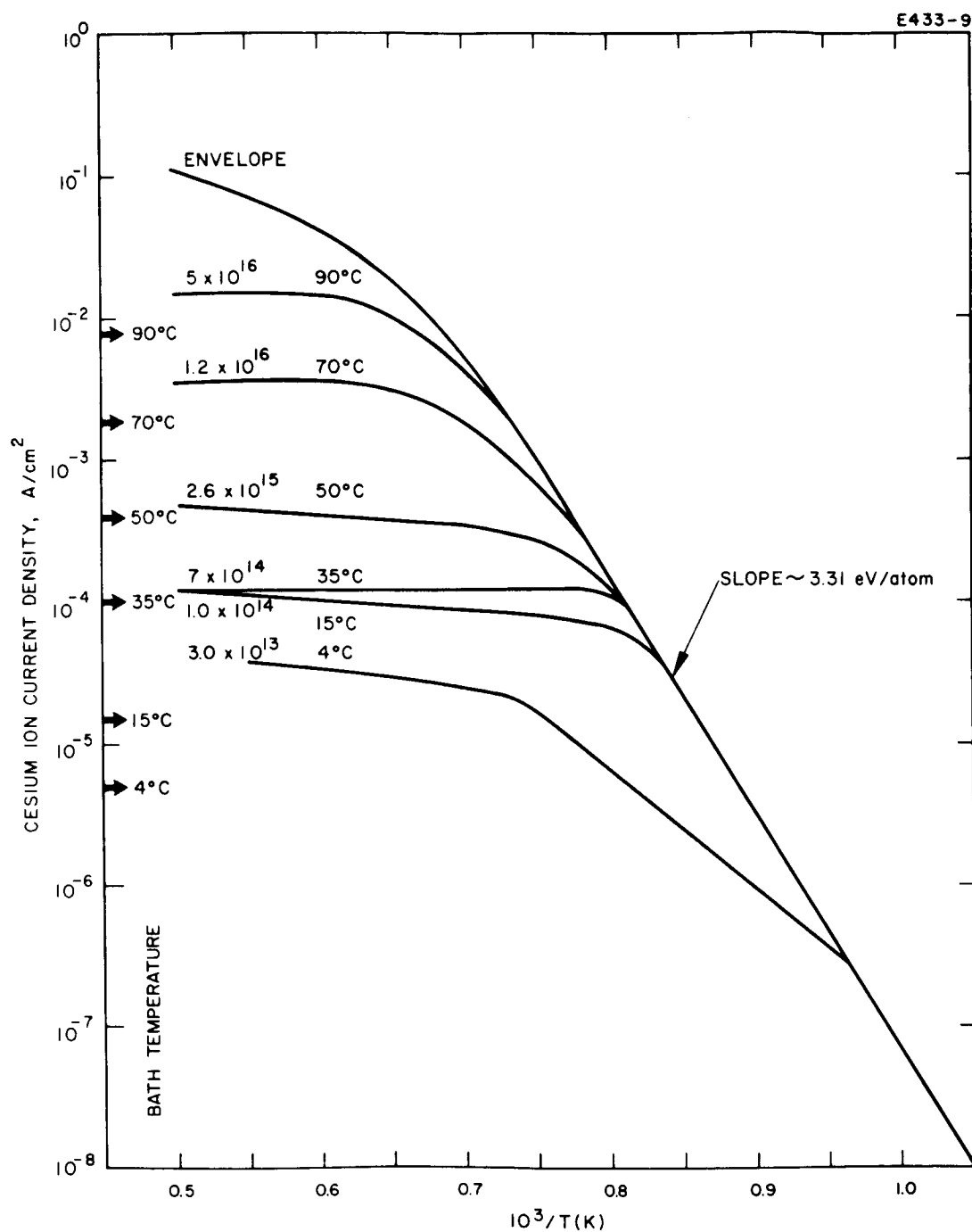
Fig. 13. Cesium ion emission data for aluminum oxide.

The cesium surface ionization critical temperature envelopes for the surfaces studied are combined in Fig. 14. The curve for copper is from the preliminary data described in Progress Report No. 1.[10] The experimental cesium ion desorption energies are listed in Table IV.

TABLE IV

Cesium Ion Desorption Energies
$(\lambda_+(\theta_c)$ in eV)

Surface	Vacuum Work Function (Clean Cesiated Work Function)	Ion Desorption Energy (Low Coverage)
Iron	4.5 (3.5)	5.95
Alumina	4.9 (5.0)	3.31
Chromium	3.9 (3.9)	3.10 (1.74)
Copper	4.5	2.85
Tungsten	4.6 (4.6)	2.77
Molybdenum Silicide	4.7 (4.7-2.8)	2.62
Molybdenum	4.2 (4.35)	2.45

In general, these data are for the critical coverage. The value of the critical surface coverage is not precisely known, but was calculated[10] to be about 0.03 for tungsten. The value probably differs slightly, depending upon the direction of approach in temperature to the critical point. The coverage for decreasing temperature would be expected to be lower because the surface is free from cesium at high temperatures, and cesium is beginning to adsorb strongly as the critical point is approached from the high side. For increasing temperature, the condition is just the opposite. The surface is heavily cesiated and, as the critical point is approached, cesium is desorbing rapidly. Therefore, the coverage might be slightly larger.
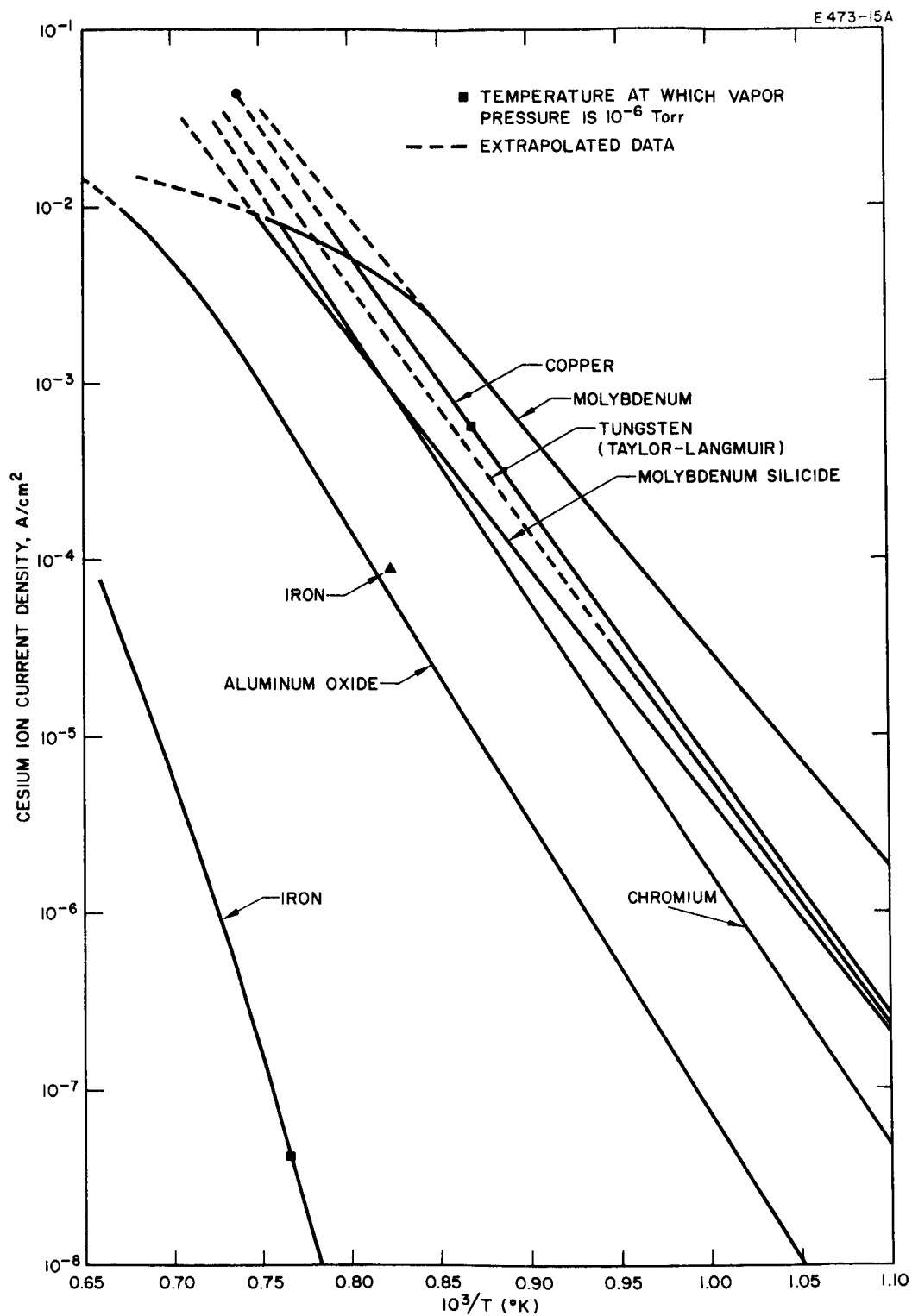
Fig. 14. Cesium ionization critical temperature envelopes for various substrates.

Indeed, the critical temperature envelopes corroborate this hypothesis by indicating slightly lower desorption energies (at lower arrival fluxes) for the decreasing temperature or lower coverage curves.

On the critical temperature envelopes in Fig. 14 are indicated melting point temperatures and the temperatures at which the vapor pressure becomes 10^{-6} Torr. Vaporization of electrode materials could cause a serious problem in ion thrustors, and appropriate temperature limits must be observed. Vapor pressure curves must be used in evaluating electrode candidates.

Melting point temperatures naturally limit the allowable temperatures of electrodes. However, extrapolation of the critical temperature envelopes above the melting temperature has a significant application under the one condition in which surface ionization on a material above its melting point is possible (i.e., when the low melting temperature electrode material is arriving at a more refractory surface, such as the ionizer (because of sputtering and evaporation), which is at a temperature above the former's melting point). If the equilibrium surface coverage of the electrode material under these conditions is high enough to create a surface which is effectively that of the electrode material, the extrapolated curve above the melting point is applicable and valid.

D.   CESIATED ELECTRON EMISSION

Electron emission curves for cesiated surfaces of molybdenum, molybdenum silicide, copper, iron, chromium, and aluminum oxide were obtained for cesium arrival fluxes in the range from 10^{13} to 10^{17} atoms/cm^2-sec. The electron S curves plotted as the logarithm of current density versus reciprocal absolute temperature from X-Y recorder traces are displayed in Figs. 15 through 21. Upper temperature limits were dictated either by the melting point or by rate of vaporization of the emitter material. The copper data are the preliminary data discussed in Progress Report No. 1, and are subject to change

following further study under Contract NAS 3-6278. The chromium data are tentative, pending a possible recheck under the same contract.

The electron emission curves for cesiated molybdenum in Fig. 15 agree fairly well with similar curves reported by Aamodt, Brown, and Nichols,[11] especially at higher cesium arrival fluxes. The dotted curve shown in Fig. 15 is their curve for an arrival flux of 10^{16} atoms/cm^2-sec. Our clean molybdenum work function is about 4.35 eV; theirs is about 4.38 eV. At 10^{16} atoms/cm^2-sec, the emission maxima would be essentially the same. Our minimum cesiated work function is about 1.62 eV and theirs is about 1.66 eV. Both heavily cesiated work functions are about 1.77 eV. The agreement between our data and their curves at lower arrival fluxes ($\sim 10^{13}$) is still fair, but it is not so good as at the higher fluxes. However, at such low arrival fluxes, their curves are extrapolated, whereas ours are measured. They obtained data down to the mid 10^{-7} A/cm^2 scale, while our curves were recorded down another two to three orders of magnitude at the lower arrival rates. Our different tube design allowed orders of magnitude lower background currents in the aperture-cup collector system (currents in the 10^{-11} and 10^{-12} A range). We were, of course, interested in data at lower arrival fluxes, while they were not, because of the different applications of interest.

The data for molybdenum silicide, shown in Fig. 16, involve a dynamic surface. The emitter surface, fabricated by W. McKee in this laboratory, was known to be essentially pure $MoSi_2$ (initially by x-ray diffraction). After the data of Fig. 16 were obtained, the emitter was again subjected to an x-ray diffraction measurement. The results indicated largely Mo_5Si_3 with a trace of Mo_5Si, no free molybdenum, and no $MoSi_2$. Thus the silicon content decreased continually during the measurements. It is now known that silicon diffuses onto the surface and evaporates at temperatures in excess of about 1500K, accelerating with increasing temperature. In the light of these facts, the following interpretation of the data in Fig. 16 is given.
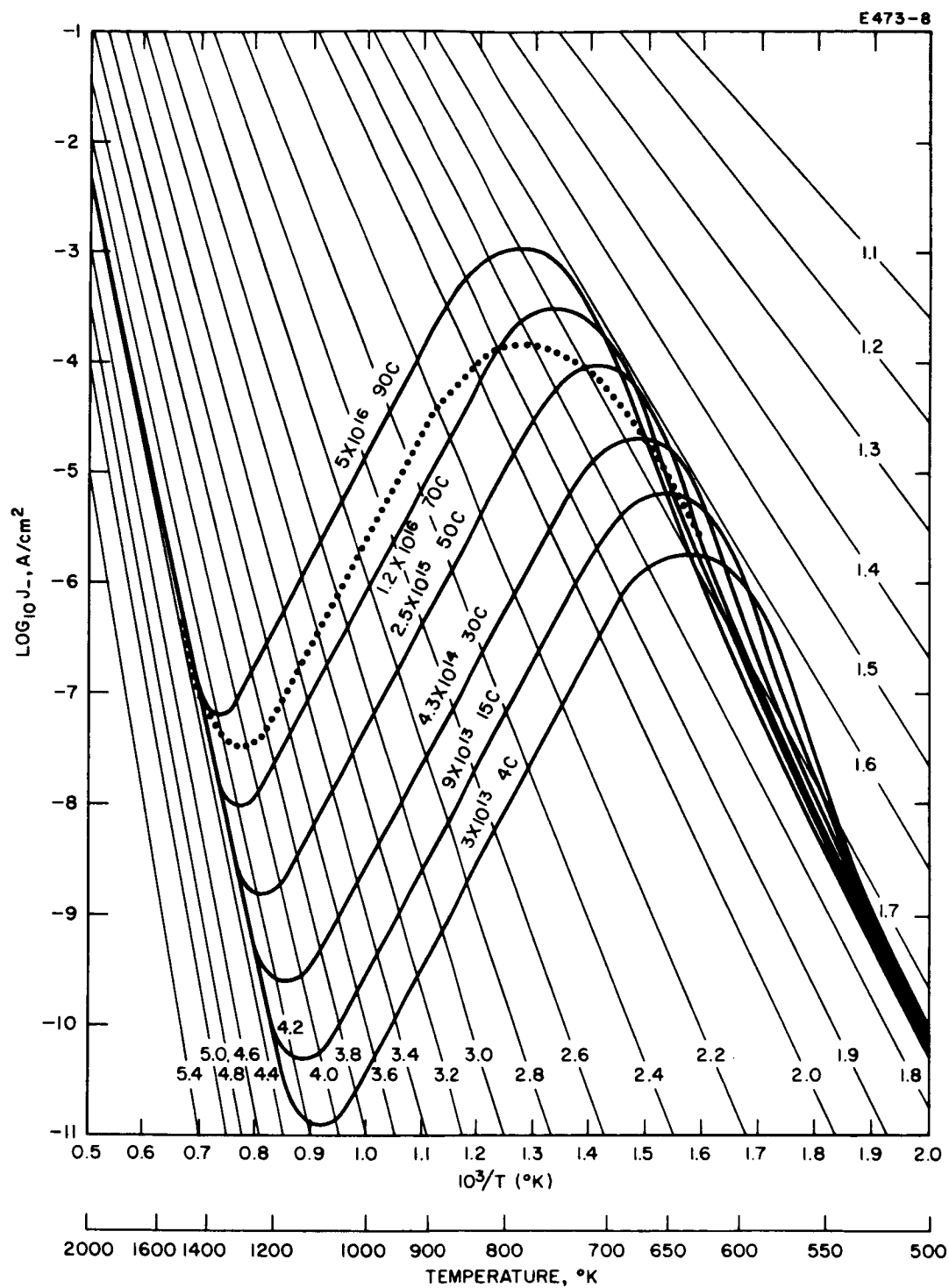
70

Fig. 15. Electron emission from cesiated molybdenum. Dotted curve is for 1×10^{16} atoms/cm^2-sec from Ref. 11.
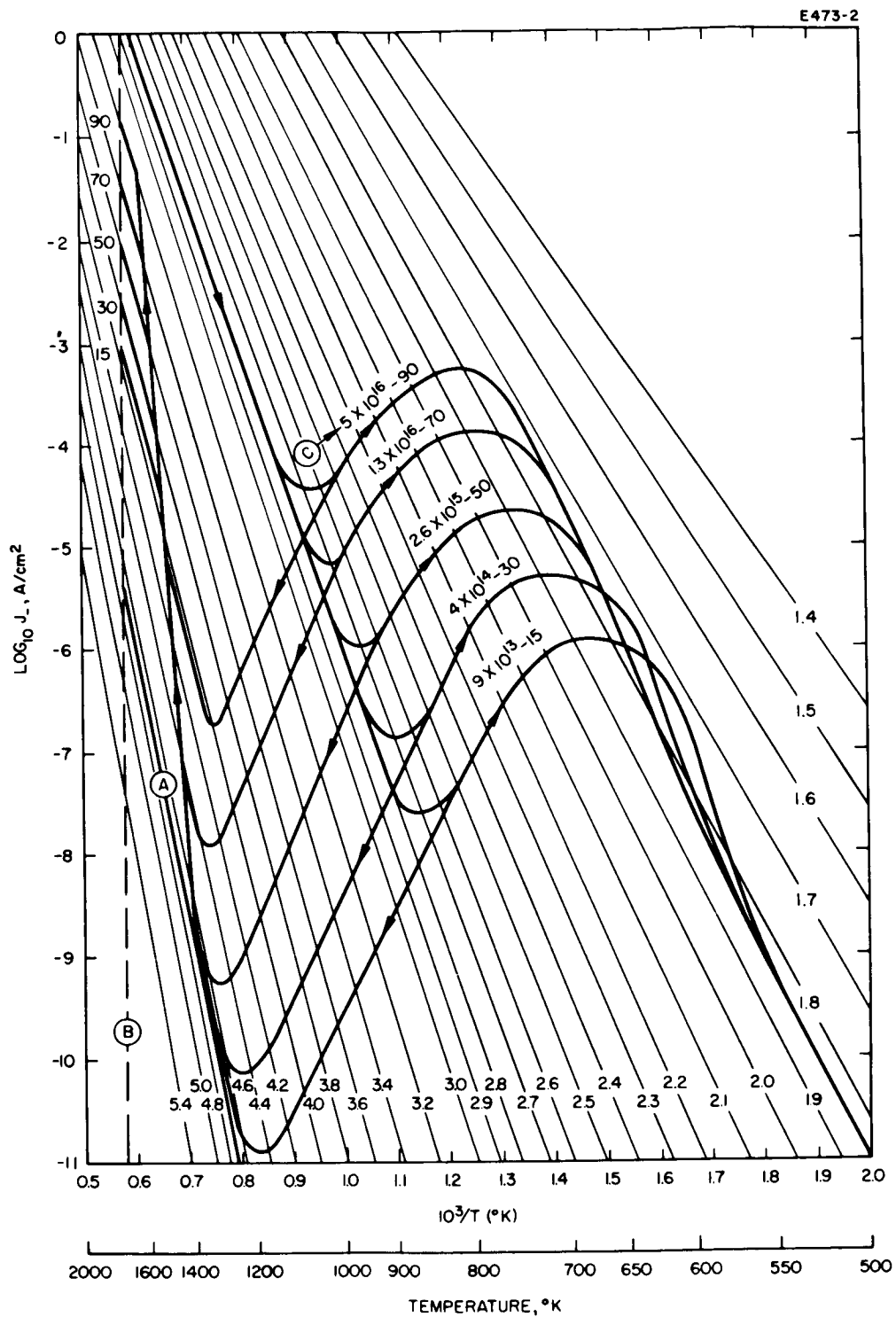
Fig. 16. Electron emission from cesiated molybdenum silicide.
A   Effective vacuum work function 4.72 ± 0.03 eV.
B   Upper temperature limit.   C   Cesium arrival flux in atoms/cm²-sec and corresponding bath temperature (C).

At a temperature of about 1450K, silicon starts to diffuse onto the surface; at and above 1600K silicon has covered the surface and is evaporating. This explains the emission curves for increasing temperature. The decreasing temperature curves were obtained immediately following an interval when the emitter was at 1700K. At first silicon is evaporating, and as the emitter cools, silicon is still covering the surface. The decreasing temperature curves are therefore probably for cesiated silicon, or more accurately, a cesiated silicon film on a molybdenum substrate. While the surface is cooling, the silicon diffuses back into the bulk from the surface and combines chemically to form some combination of $MoSi_2$ and Mo_5Si_3, depending on how much total silicon has evaporated. Before the next upward temperature curve is begun, at a new cesium arrival flux and bath temperature, the reaction has stopped and a new surface — some combination of $MoSi_2$ and Mo_5Si_3 — exists for the next run. The silicon concentration eventually decreases until no $MoSi_2$ remains, and the processes switch to a Mo_5Si_3 and Mo_5Si combination — still keeping a diffusing and evaporating silicon layer on the surface at high temperature.

The value of the effective vacuum work function of $MoSi_2$ was well established at 4.72 ± 0.04 eV (polycrystalline). The value of vacuum work function for cesiated emission S curves usually is attained at the high temperature end of the curve and maintained as the temperature is increased further. However, in the case of molybdenum silicide, a value of about 4.7 eV was attained at high temperature for increasing temperature data (starting from room temperature); with further increase in temperature, the work function decreased to lower and lower values (4.0 to 3.2 eV in the range of cesium arrival flux studied) with increasing cesium arrival flux. All of the decreasing temperature curves (for various cesium fluxes starting after being for some time above 1700K) came down along the 2.8 eV line to the appropriate S curve which they then followed to lower temperatures.

73

The data for copper in Fig. 17 were obtained by heating the copper emitter before each curve was measured to a temperature 100C below the melting point, resulting in the evaporation of a layer of copper onto the tube envelope. The data were then obtained immediately by continuously decreasing the surface temperature from this maximum to room temperature. These vacuum conditions were inferior to later work with the other materials reported here. It is likely that the curves for copper were influenced by some surface contamination resulting from absorption from the ambient background gas. The lowest cesium arrival flux curve of Fig. 17 was obtained at a bath temperature of -11C accomplished by the use of alcohol and solid carbon dioxide. A similar attempt at -20C failed to produce emission currents greater than the background leakage currents. Corresponding curves for a definitely contaminated copper surface were reported in Progress Report No. 1.

The electron emission data for iron exhibited three distinct types of behavior, all of which are shown in Figs. 18 and 19. The data were obtained with three different experimental tubes. The data from the first tube were obtained under vacuum conditions which were not up to the requirements of this work. Furthermore, the diode separation was closer than it should have been during part or all of the measurements, resulting in higher applied fields than were intended. These data, obtained with the diaphragm collector rather than with the aperture-cup collector system, are shown in Fig. 18, and are believed to represent a contaminated iron surface with somewhat higher fields than correspond to the zero field condition. Because of these problems a second iron tube was fabricated. The pressure in this tube was better and no geometry problems arose. The data were drastically different (see curve A of Fig. 19). The broadness of the curve accounts for small differences among many curves for the various cesium arrival fluxes and increasing and decreasing temperature curves. No cesium adsorption-desorption peak resulting in the usual maxima and minima was observed. The emitter temperature was taken down to and up from room temperature, but a low temperature emission part of the S curve was not found.
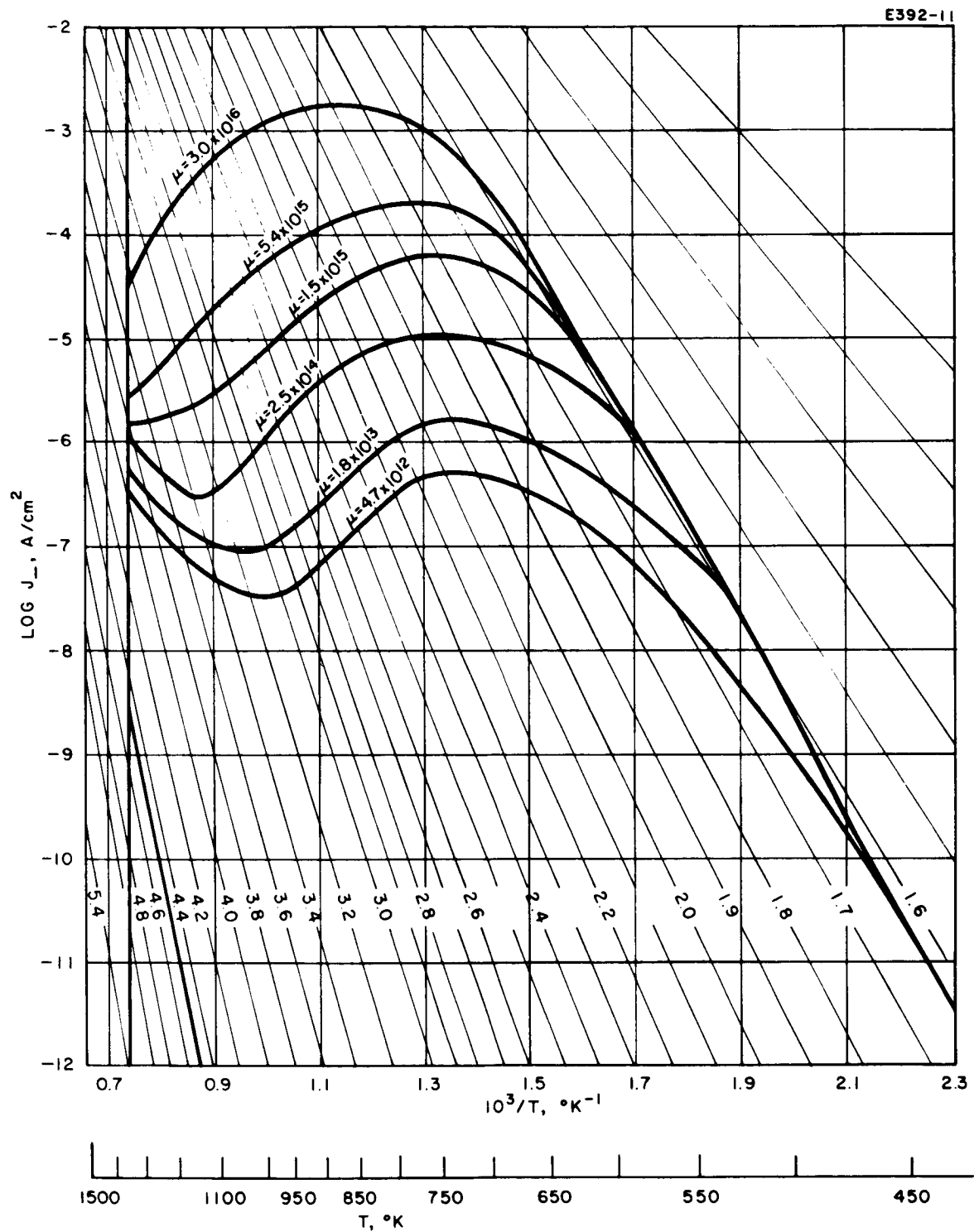
Fig. 17. Preliminary electron emission curves for copper at essentially zero field.
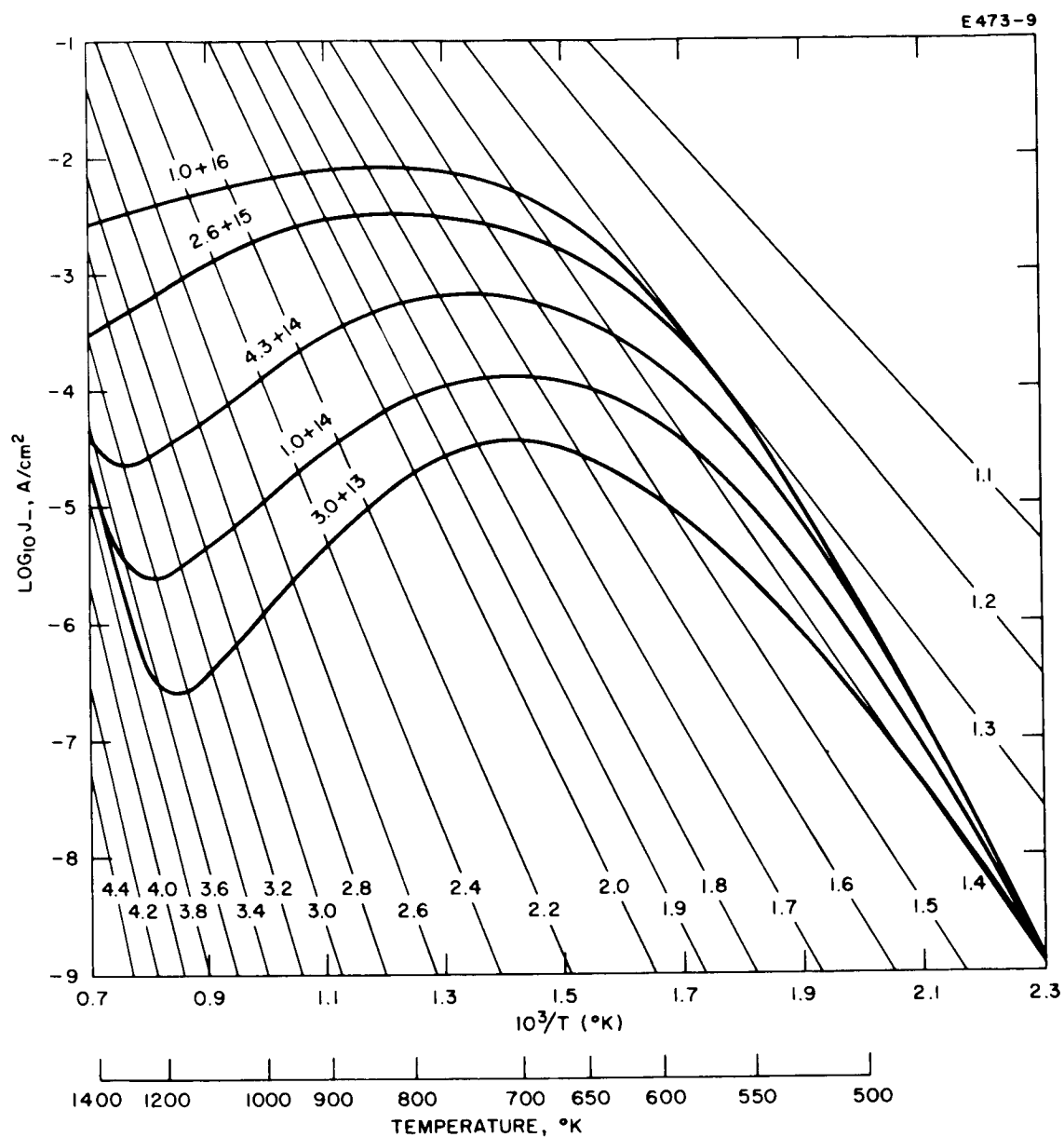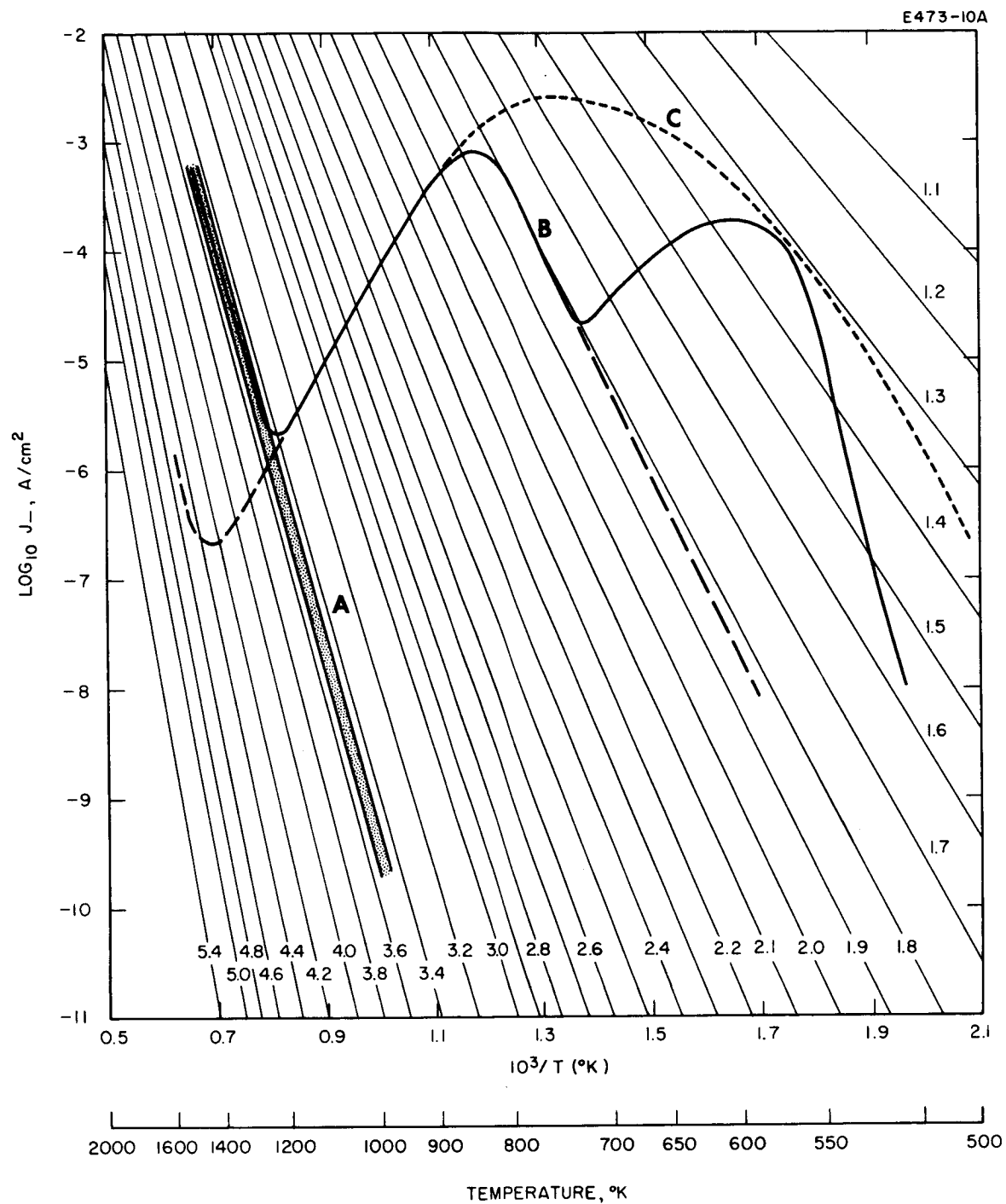
Fig. 18. Electron emission from cesiated iron.

Fig. 19. Electron emission from cesiated iron.

Because of the substantial differences between the results for the two iron tubes, a third was fabricated and tested. The results were identical to those for the second iron tube; the data for all bath temperatures fell on or near curve A in Fig. 19. However, curve B of Fig. 19 was the result of a special effort and was obtained by increasing the emitter temperature from room temperature at the maximum possible rate by driving a sudden high current pulse through the emitter heater and then sustaining a high current. The curve was traced in a few seconds from low to high temperature. The high temperature end coincides with the data of curve A. However, a double peak appeared at low temperature. By extrapolating the higher temperature peak, a usual kind of S curve can be drawn, which might have been expected for iron. Curve C represents data obtained under the fast temperature sweep conditions from the first tube (with the diaphragm collector) at the same arrival flux as for curve B. It is believed that curve C represents a summation of the two peaks exhibited in curve B, but it was taken slowly enough to allow the contamination to destroy the minimum which distinguishes the two peaks in curve B.

The bulk of the data for iron under the better vacuum conditions fits curve A for both of the collector systems. The different data of curves B and C of Fig. 19 and all of the data of Fig. 18 are indicative of contamination but include the usual influence of cesium.

As discussed in a previous section, the cesium ion emission data for iron were also anomalous and consistent with the electron data. The observed 3.5 eV work function of the cesiated iron surface is mentioned in relation to the 4.5 eV vacuum work function measured for iron. It is also pointed out that the binding energy for cesium ions (desorption energy) is 6 eV, calculated from the slope of the ion emission data. The lack of electron emission from what should be a cesiated, but otherwise clean, iron surface may fit the picture properly. Several possible explanations for these anomalous observations were offered in the section on ion emission. The originally pure (5 N's) iron surfaces were known

to be pure iron surfaces upon completion of the measurements. They showed evidence of considerable evaporation of iron during the measurements.

The curves for chromium (Fig. 20) are similar to those for tungsten for lower temperatures. A minimum work function of about 1.7 eV is observed. The lower vacuum work function of chromium causes differences at higher temperatures. The "clean" cesiated work function for chromium is seen to be about 3.55 eV, whereas its vacuum work function is about 3.9 eV.

The electron emission curves for alumina are shown in Fig. 21. The uncesiated work function curve reached at higher temperatures is about 5.0 eV. The vacuum measurement prior to the introduction of cesium was 4.9 eV. No minimum work function followed by a "roll-over" to a higher value at coverages greater than one monolayer is exhibited for alumina. Instead, a constant cesiated work function of between 1.83 and 1.85 eV is observed for all cesium arrival fluxes and all low temperatures. This effect distinguishes the alumina data from those of the metals and semiconductor metal compounds. Another observed difference is the shallowing of the minima and the depression of the maxima in the S curves resulting in flatter and shallower S curves with increasing arrival flux. Extrapolation predicts that above about 5×10^{17} atoms/cm^2-sec, no minimum would exist.
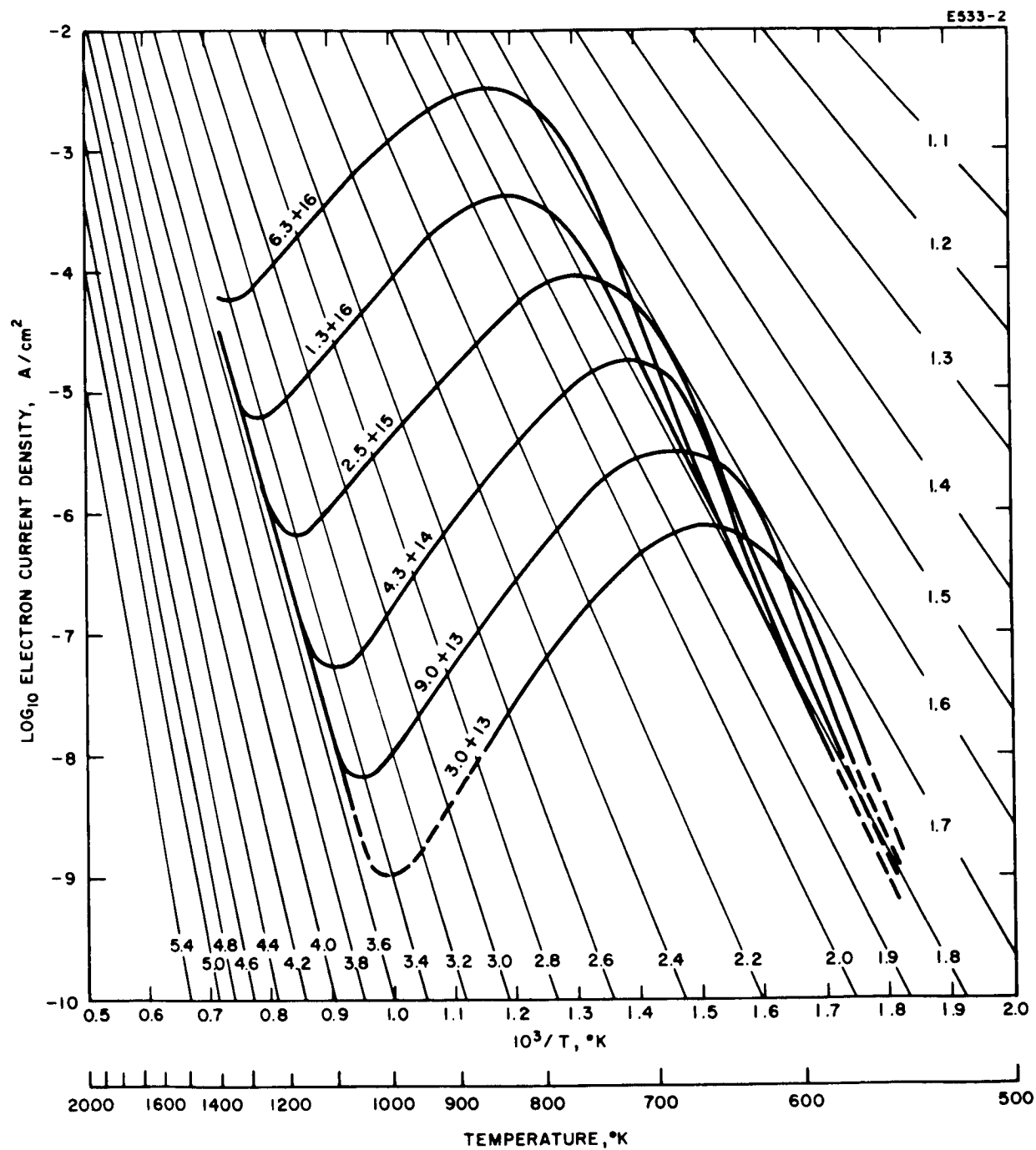
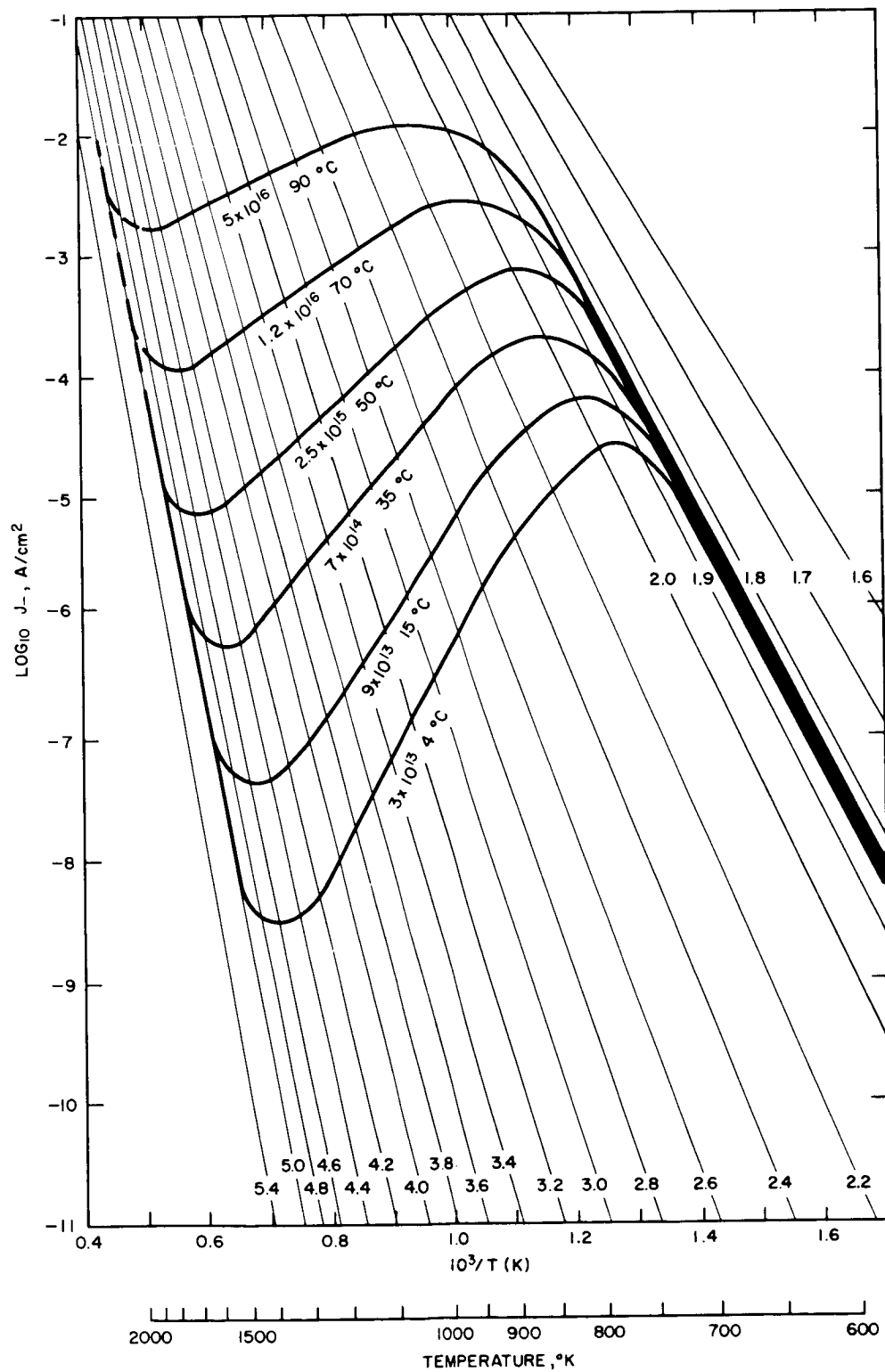Fig. 20. Cesiated electron emission from chromium.

Fig. 21. Electron emission from cesiated aluminum oxide.

E.   CESIATED WORK FUNCTIONS

For any substrate material and sufficiently high cesium surface coverage (greater than one monolayer), the composite surface work function should approach that of bulk cesium, about 1.8 or 1.9 eV. However, as the coverage approaches one monolayer, the work function generally decreases below the bulk cesium value for surface temperatures just below the emission maximum, and results in a minimum work function. This applies to the low- or zero-field condition. Larger surface electric fields cause higher emission and lower apparent work function for all values of coverage.

For every substrate, a value of the minimum work function exhibited as the surface coverage approaches a monolayer can be obtained from the electron emission S curves, as can a value of the work function of bulk cesium (or at least a heavily cesiated surface). These two distinguishable values of cesiated work function are listed in Table V for the surfaces studied. The values for copper, platinum, and tungsten are subject to change because they were obtained from the preliminary measurements reported in Progress Report No. 1,[10] rather than with the special clean vacuum system. From the experimental data for most of the surfaces which can be thermally cleaned, the experimentally measured bulk work function of cesium is seen to be 1.85 eV.

F.   TEMPERATURE, FIELD, AND TIME HYSTERESES

In the measurement of surface ionization ion current density as a function of surface temperature, several investigators have observed that a hysteresis effect results from a reversal in the direction of temperature change through the critical region. This effect was observed in the work reported here, as well as similar effects in the electron current density versus temperature plots and time dependent hysteresis, i.e., from differences in the time rate of change of the surface temperature as well as from reversal of the direction of temperature change.

TABLE V

Cesiated Work Functions

Surface	Minimum Cesiated Work Function ($\theta \rightarrow 1$), eV	Heavily Cesiated Work Function ($\theta > 1$), eV
Tungsten[a]	1.70	1.84
Molybdenum	1.62	1.77
Copper[a]	1.58	1.64[b]
Platinum[a]	1.73	1.85
Chromium	1.65	1.70[b]
Iron	1.82 (to 1.4)	1.82 (to 1.4[b])
Molybdenum Silicide	1.73	1.85
Alumina	1.83	1.86

[a]Tentative

[b]Probably contaminated

In addition, field dependent hysteresis was observed in the region of ion critical temperature hysteresis. All of these effects were examined in some detail, and as a function of various other parameters such as cesium arrival rate, electric field, and substrate material.

Figure 22 shows a cesium ion current density versus temperature trace for molybdenum at a cesium arrival flux of 6.2×10^{14} atoms/cm^2-sec measured with the cup collector. This curve illustrates the directional temperature hysteresis effects generally observed in this arrival flux range. This curve was obtained for a slow rate of temperature change. The trace for increasing temperature is relatively smooth; it increases nearly exponentially up to 1038K where the characteristic critical temperature break occurs; at this point an increase of one and one-half orders of magnitude in current density occurs over a temperature interval of about 2K, above which the saturated current density is
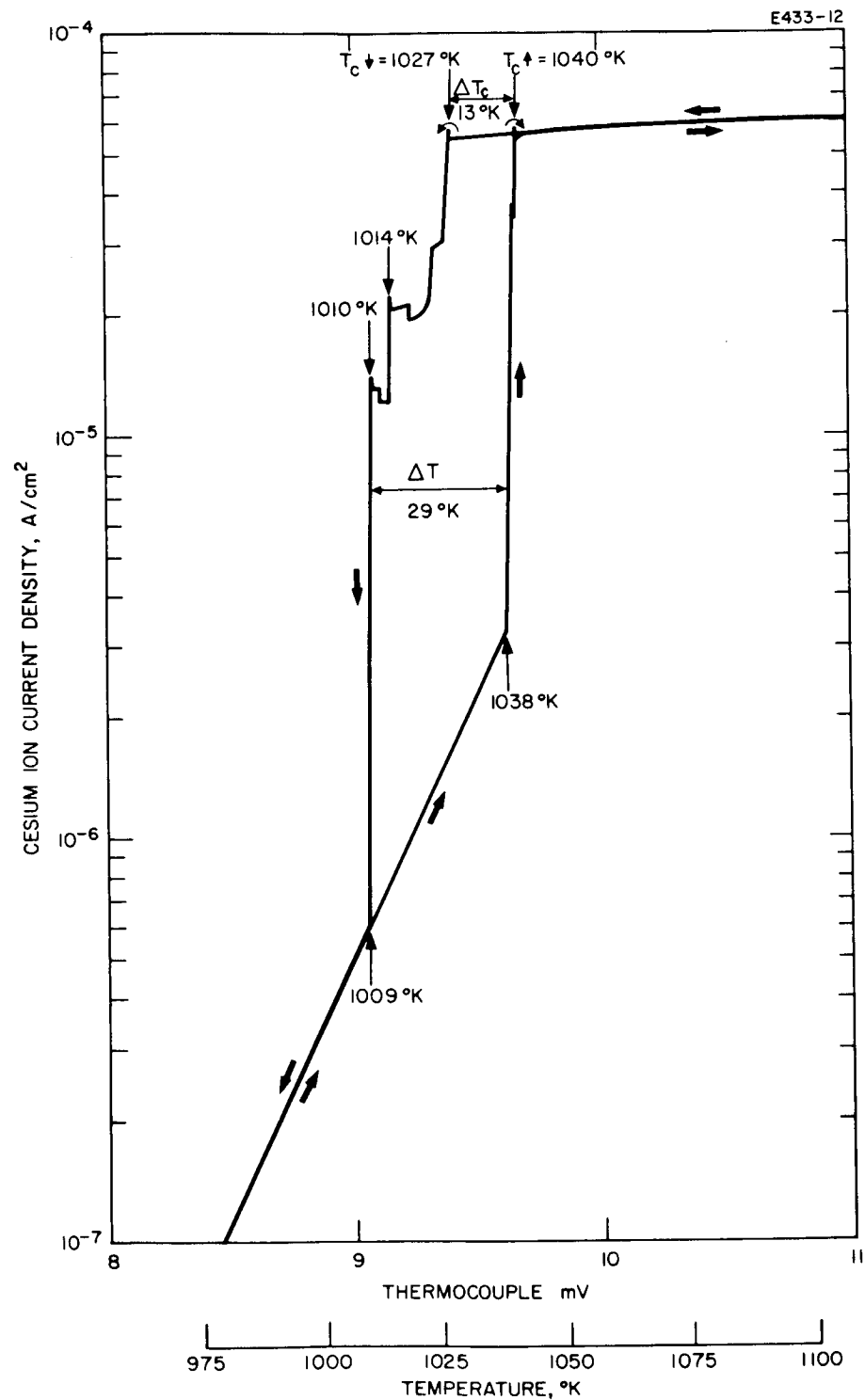
Fig. 22. Critical temperature, temperature hysteresis, and cesium adsorption effects for ionization of cesium on molybdenum.

drawn. The ascending temperature or "upper" critical temperature (because it is higher) is defined as the temperature at which the saturated ion current density is drawn, or 1040K in Fig. 22. One slight break is observed just before the saturated current density is reached. A very small spike is seen just as saturation is achieved which appears as if a slight overshoot occurred because of an electromechanical effect in the recorder. However, this and other similar spikes are attributed to a true surface emission phenomenon because they also occur in the decreasing temperature curves when approached from a constant current condition.

As the temperature is subsequently reduced from several hundred degrees above the critical temperature, the current density traces back along the increasing curve but continues to maintain saturation as the former critical temperature is passed. At 1027K a small spike occurs, followed by a decrease in current density. However, the current density does not fall rapidly through one or two orders of magnitude but exhibits the interesting structure seen in Fig. 22. This structure consists of step-wise changes with a general tendency to decrease, and of more spikes prior to sharp decreases. Finally, at 1010K a sharp drop of about one and one-half orders of magnitude occurs in about 1K and reaches the original increasing temperature curve, which it then traces to lower current densities.

In the case shown and in others, the processes were repeated exactly to check for reproducibility of the observed hysteresis loop. In nearly all of them, the hysteresis loops were reproduced by identical temperature breaking points and by identical reproductions of the fine structure in the decreasing temperature curve in magnitude of the step-wise decreases, breaking point temperatures, and even the spikes. In other cases, the magnitude of the current density steps varied somewhat (10 to 30%) but the temperature breaks and general structure were very closely reproduced. In the specific case illustrated in Fig. 22, the curve was very well reproduced.

For this reason, the fine structure in the decreasing temperature curve is felt to be characteristically related to the process of cesium adsorption occurring in this region, possibly on different types of surface patches, under the specific sets of conditions of cesium arrival flux, surface electric field, and time rate of temperature change. It has been shown that changes in all of these conditions will influence the observed structure, as will be illustrated.

In Fig. 22, the point at which ion current density exhibits its first sharp decrease from saturation (1027K in this case) is defined as the descending temperature or "lower" critical temperature. The difference between upper and lower critical temperatures is designated ΔT_c. This quantity is seen in Fig. 22 to be 13K at saturation and 29K between the sharp, large-magnitude current density steps. This quantity ΔT_c has been observed consistently to decrease with increasing cesium arrival flux until it disappears at about 1 mA/cm^2 of saturated cesium ion current density. It has also been shown to vary with the rate of temperature change. Both of these latter observations are illustrated in Fig. 23(a) and (b), which are a series of actual recorder plots for a molybdenum surface at two cesium arrival fluxes, one at 1 x 10^{14} atoms/cm^2-sec, which shows a substantial hysteresis effect, and one at 8 x 10^{15} atoms/cm^2-sec, which shows only a very small hysteresis effect for slow rate of temperature change. The plots of Fig. 23(a) and (b) are intended for qualitative illustration; no specific current densities or temperatures are shown. The current density magnitudes do not necessarily correspond to the various curves in the figures.

The effect of varying the time rate of change of surface temperature at the two different cesium arrival fluxes is seen in Fig. 23(a) and (b). The time spent in traversing the temperature interval between the marks on the abscissa is indicated on each curve. It is observed that the magnitude of the temperature hysteresis effect increases as the rate of temperature change increases for both arrival rates. In the fastest plots at both arrival rates, some distortion caused by exceeding the tracking sensitivity of the X-Y recorder is believed to occur.
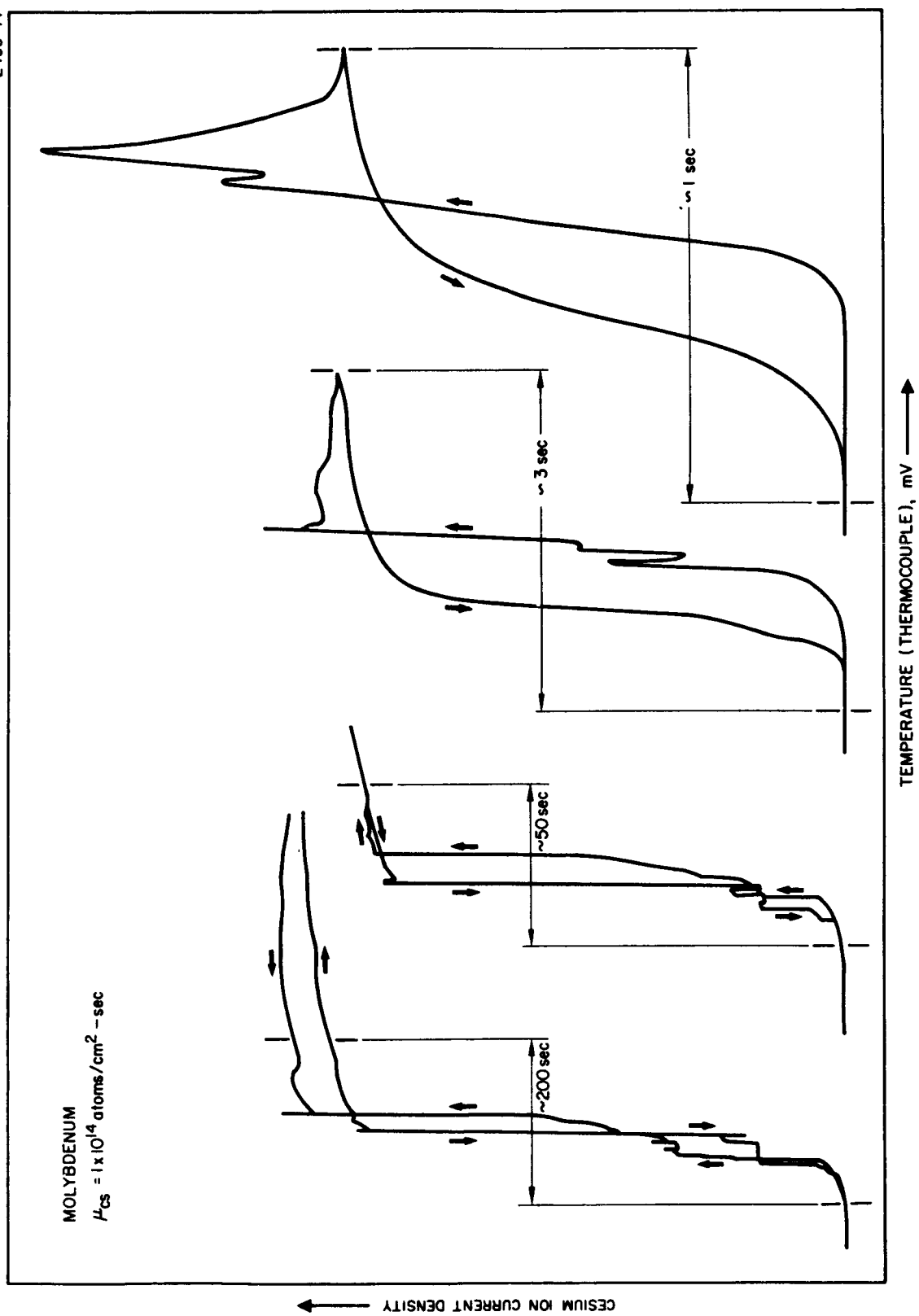
Fig. 23(a). Influence of time and current density on temperature hysteresis for ionization of cesium on molybdenum.
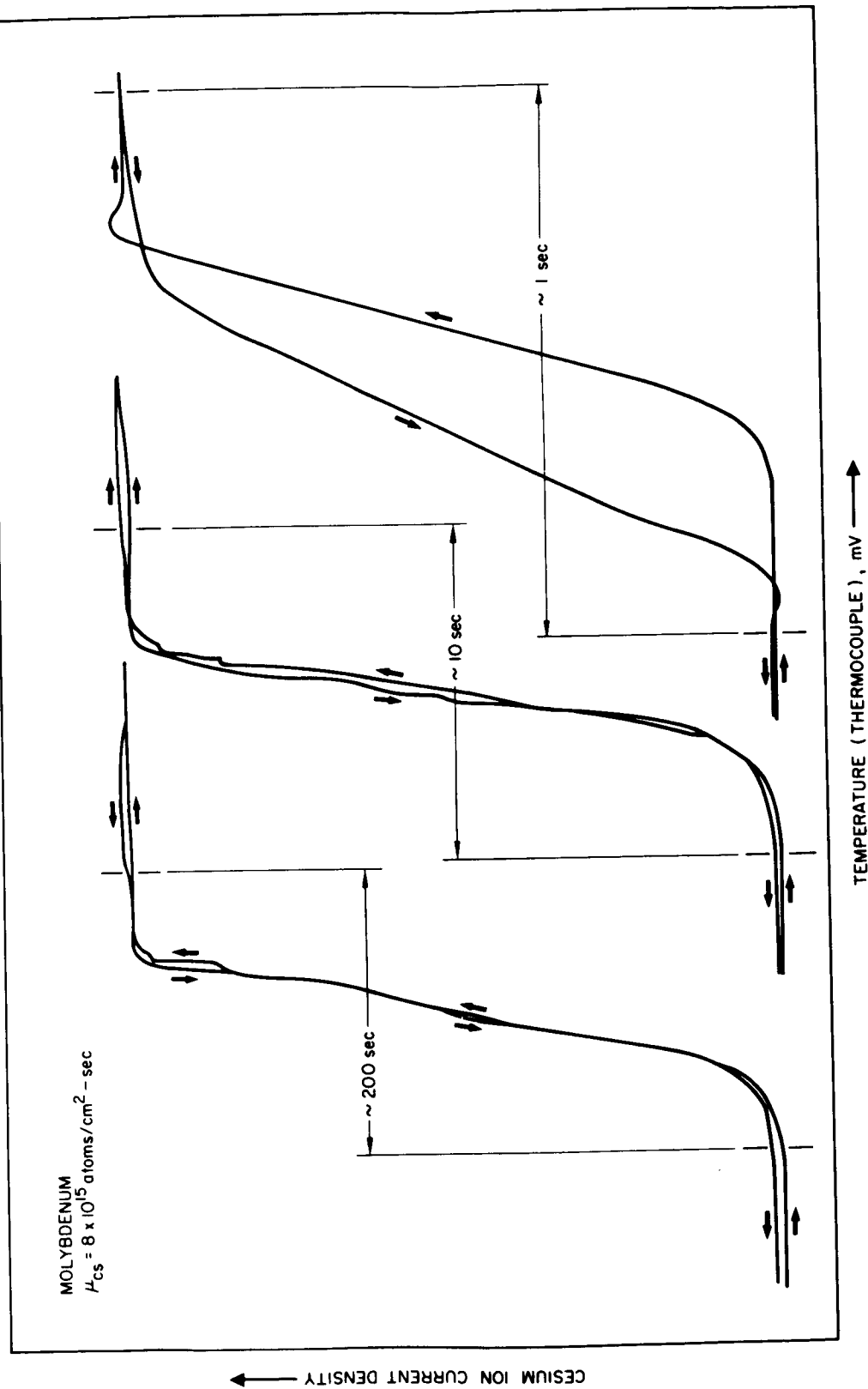
87

Fig. 23(b). Influence of time and current density on temperature hysteresis for ionization of cesium on molybdenum.

Because the ion emission current is observed to be bivalued at temperatures within the temperature hysteresis region, two distinct values of surface work function at these temperatures are implied. The cause is clearly two different cesium surface coverages, resulting from the approach to the region from nearly zero coverage for decreasing temperature, and from larger coverage for increasing temperature. Sharp discontinuities of the right magnitude have been observed occasionally in electron emission curves at temperatures within the temperature hysteresis region in the corresponding cesium arrival flux ion emission curves; these indicate that the composite surface work function and the electron emission may be influenced by a bivalued surface coverage. This possibility was investigated in more detail for a copper surface.

A temperature hysteresis condition was established as shown in Fig. 24. The cesium arrival flux was about 7×10^{14} atoms/cm^2-sec and the electric field was 750 V/cm. The temperature was then fixed in the hysteresis region, as indicated by the arrow in Fig. 24. The electric field was varied from zero to greater than 10^4 V/cm and back to zero. A reproducible electric field hysteresis effect was observed for electron emission with both the aperture-cup collector and the diaphragm collectors as shown in Figs. 25 and 26, respectively. Two different zero-field extrapolation values of effective electron work function can be obtained from the cup collector data as shown in Fig. 25, where a value of 2.93 eV is obtained by extrapolating the low field data (0 to 300 V/cm), and a value of 2.59 eV is obtained when the high field data (300 to $> 10^4$ V/cm) are used. It is evident that a general hysteresis region exists for a cesiated surface, resulting from two possible values of cesium surface coverage, and that it may be manifested in both ion and electron emission as temperature and/or electric field hysteresis effects.

Fig. 24. Cesium ion critical temperature for copper showing hysteresis.

In the figure:

Y-axis (left): CESIUM ION DIAPHRAGM COLLECTOR CURRENT, A
Y-axis (right): CESIUM ION FARADAY CUP COLLECTOR CURRENT, A
X-axis: SURFACE TEMPERATURE

$E = 750 V/cm$
$\mu_{cs} = 6.8 \times 10^{14}$ atoms/cm^2 sec

TEMPERATURE AT WHICH
ELECTRIC FIELD HYSTERESIS
WAS MEASURED

Fig. 25. Applied surface electric field hysteresis effect in the cesiated electron emission cup collector current for a copper surface at a temperature in the cesium ion critical temperature region (see Fig. 24).
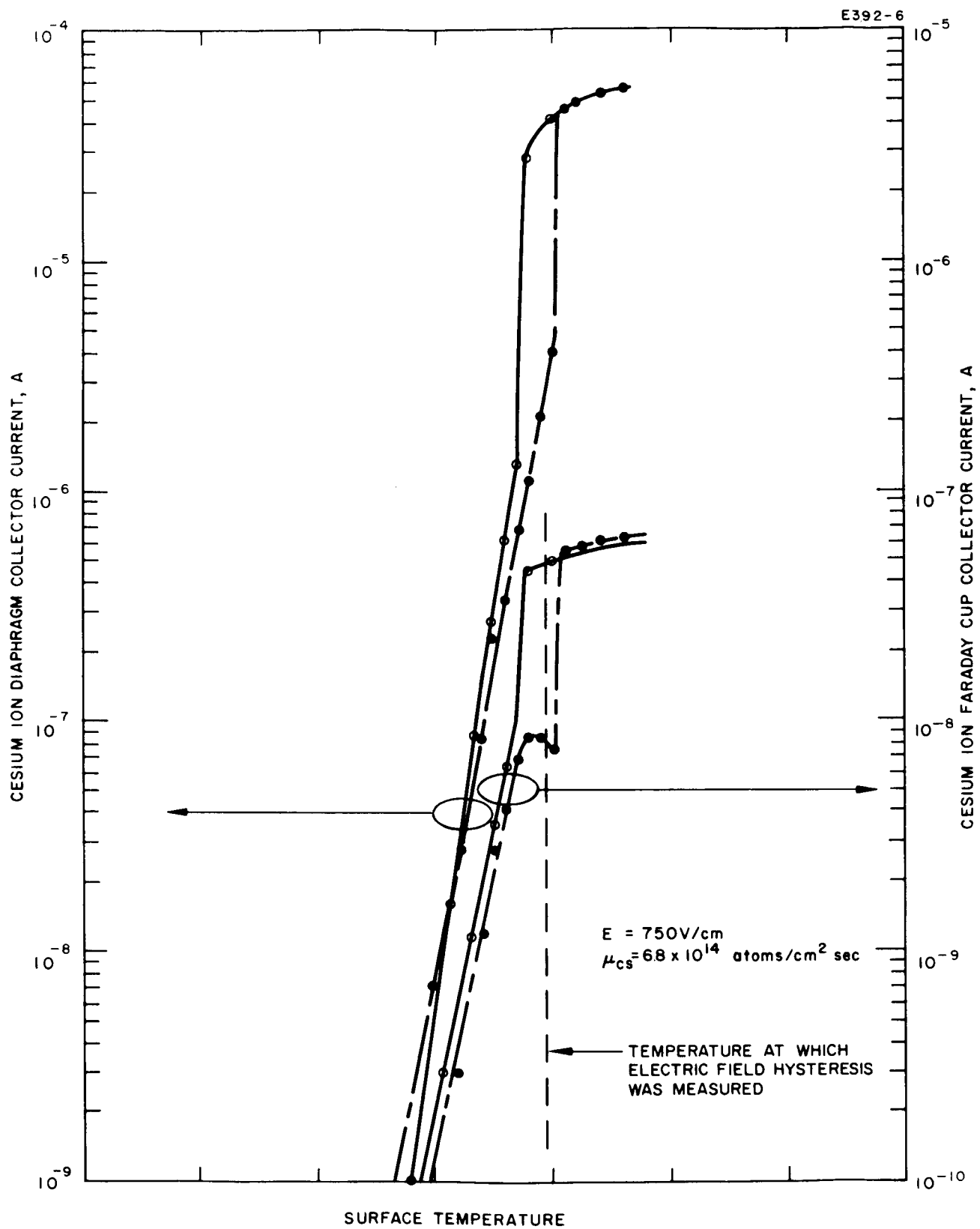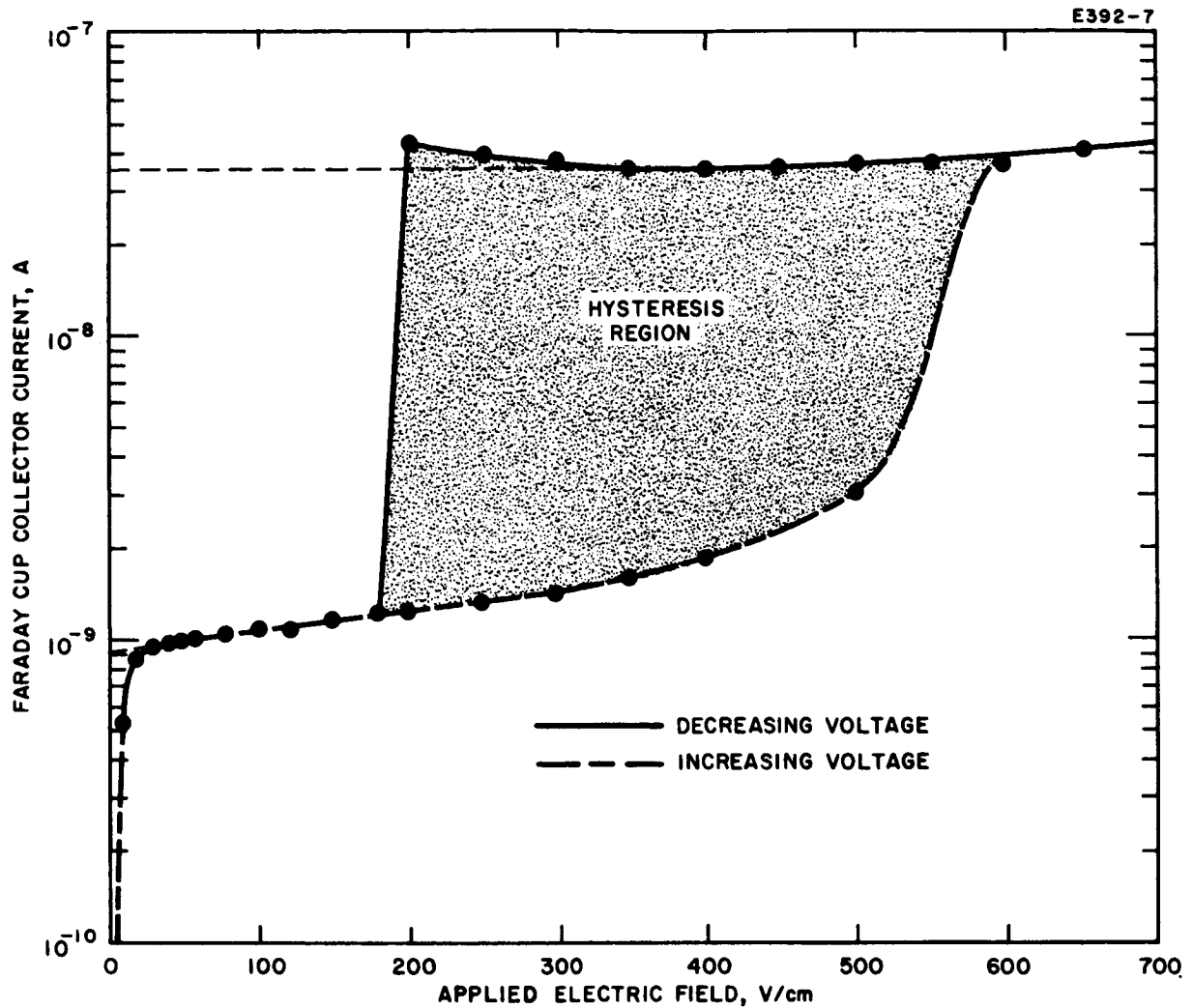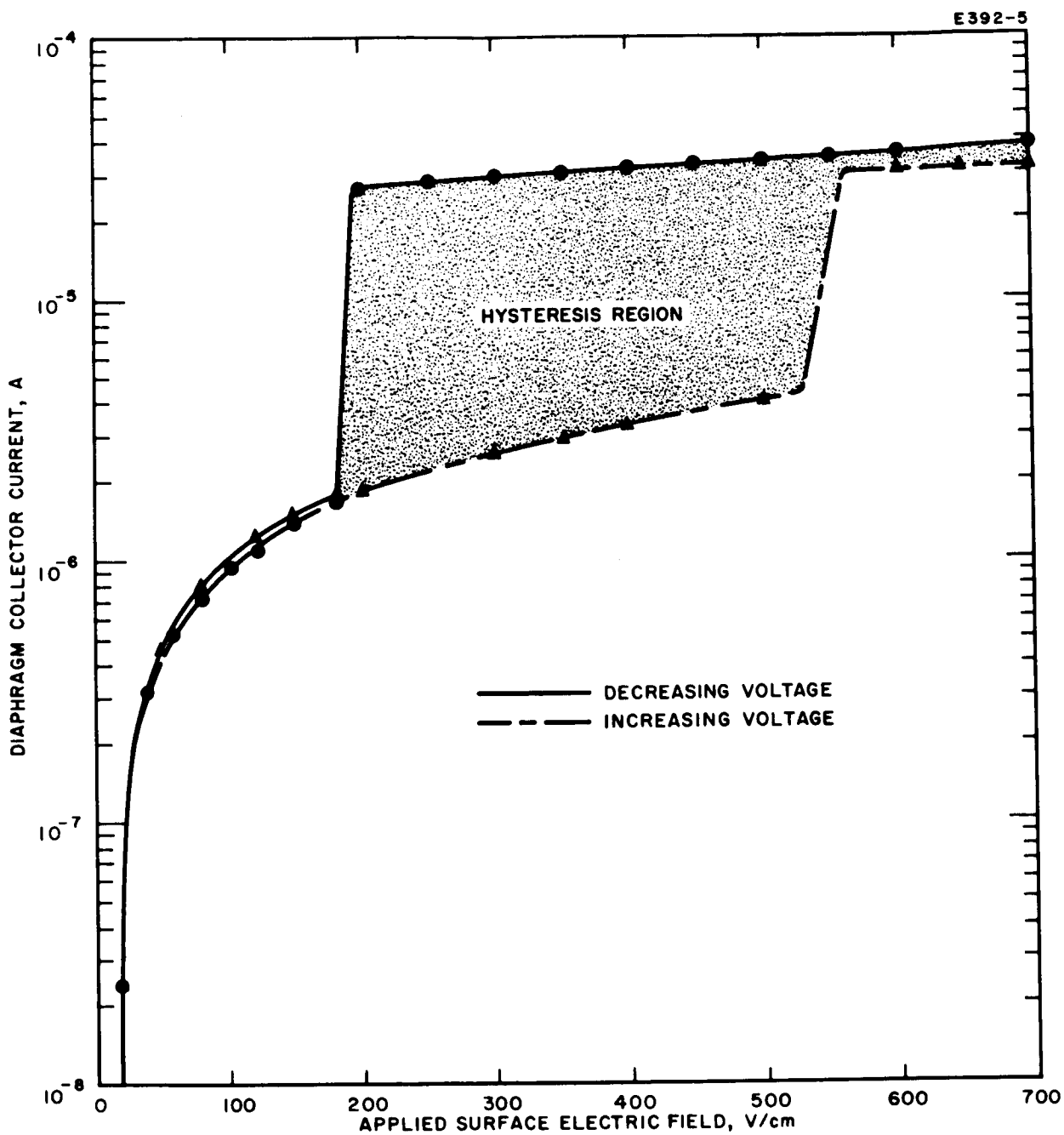
Fig. 26. Applied surface electric field hysteresis effect in the cesiated electron emission diaphragm collector current for a copper surface at a temperature in the cesium ion critical temperature region (see Fig. 24).

G. INFLUENCE OF APPLIED SURFACE ELECTRIC FIELD AND CONTAMINATION

The emitter surfaces studied in this program were clean "as-received" or machined polycrystalline. These surfaces were usually very pure, similar to those employed in practical devices such as surface contact ion thrustor electrodes. They were probably very patchy in terms of work function, and were microscopically rough. Therefore patch field effects were expected. The normal Schottky effect was expected to be observed for the plane parallel diode diaphragm collector currents. The shape of the I-V characteristics curves for the aperture-cup collector (normal electric and magnetic fields) was not yet known.

Experimentally observed shapes of the I-V curves for the two collector types are shown in Figs. 27 and 28 for a molybdenum ribbon at 1970K. In Fig. 27, the data for the diaphragm collector are plotted versus $\sqrt{E}$ (to greater than 10^4 V/cm) to show the Schottky plot extrapolation to the zero-field current value. The corresponding aperture-collector cup data are plotted in Fig. 28 to 2000 V/cm. Data were obtained to 5×10^4 V/cm, but the collector current remained constant from 22 to 5×10^4 V/cm except for a slight decrease above 2.5×10^4 V/cm. The perveance of the system was 8×10^{-5} A/V$^{3/2}$ (per cm^2).

A slightly different field effect was observed for chromium at high values of applied field. For fields up to about 10^3 V/cm, Schottky emission was observed as shown in Fig. 29. From 10^3 to 10^5 V/cm, a stronger field dependence was observed as shown in Fig. 30. The dependence changed from $I \propto E^{1/2}$ to approximately $I \propto E$. A third type of field dependence, including virtual extrapolations, was observed for alumina, as described in more detail in the discussion of alumina in Section IV-A.

Little and Whitney[11] have shown that for a number of metals at room temperature, fields of 10^5 V/cm can cause surface whiskers which can result in local field enhancement and in subsequent field emission. However, their observed currents were temperature independent. The

E473-4
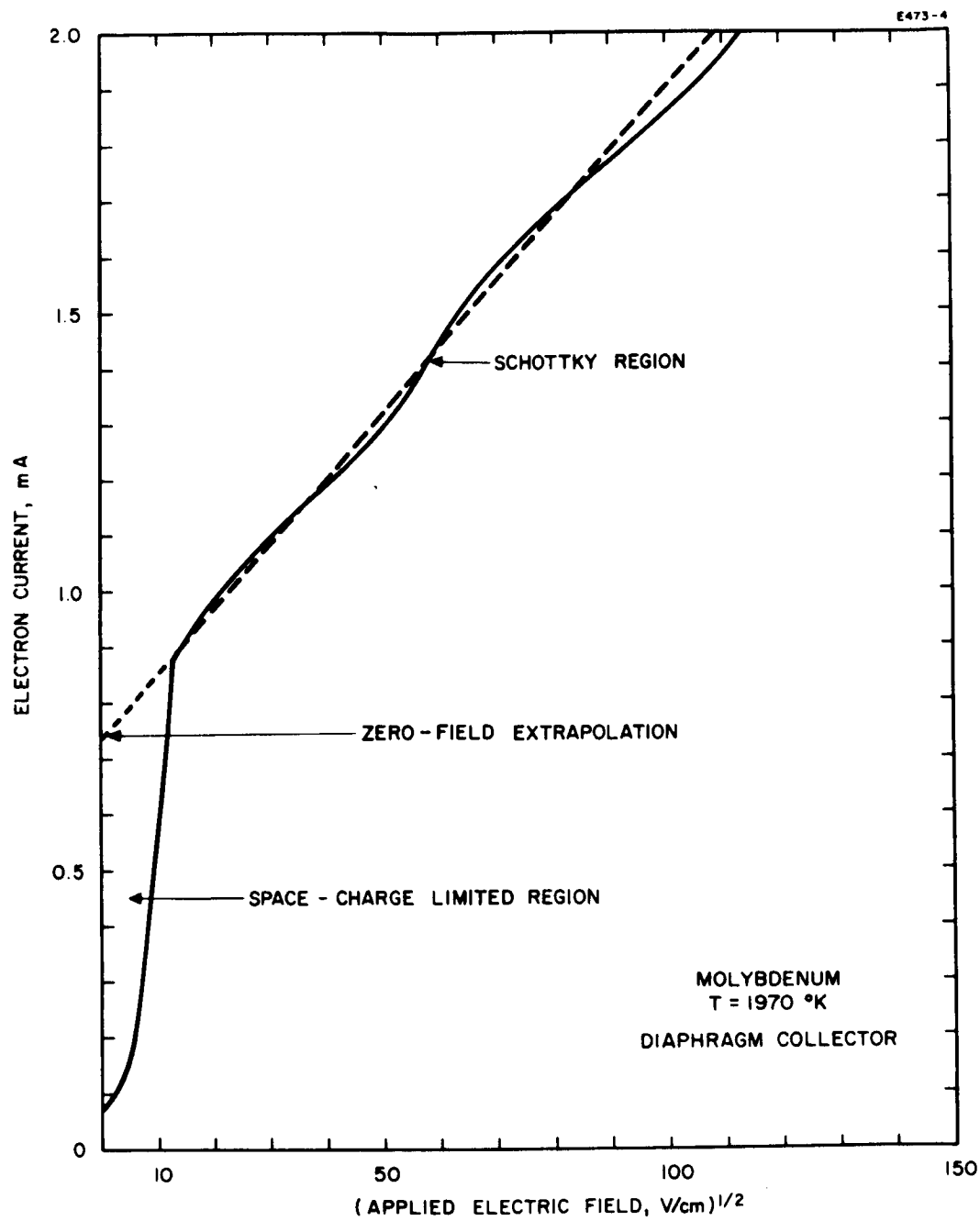
Fig. 27. Current-voltage characteristics for diaphragm collector.
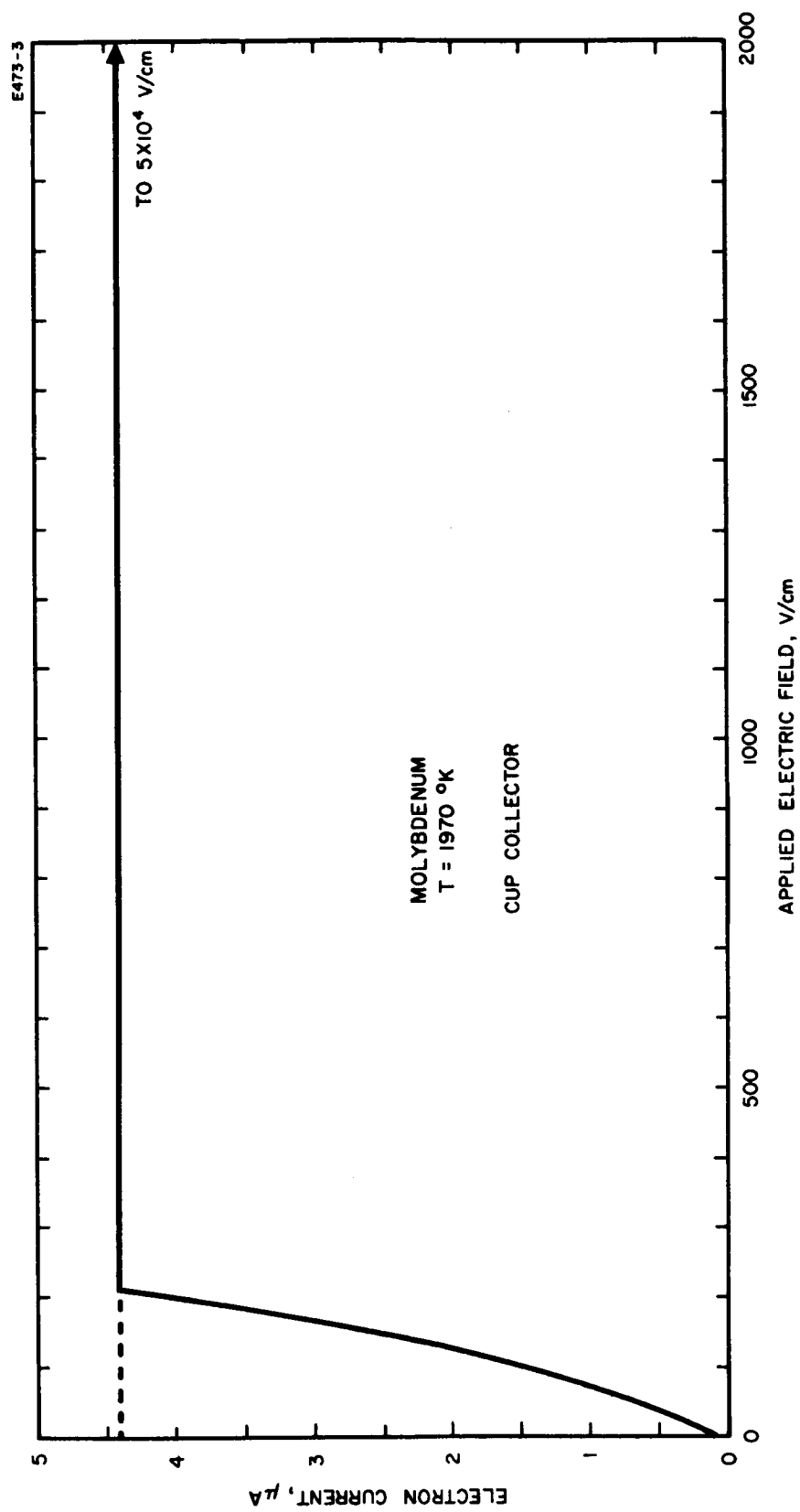
94

Fig. 28. Current-voltage characteristics for aperture-cup collector.
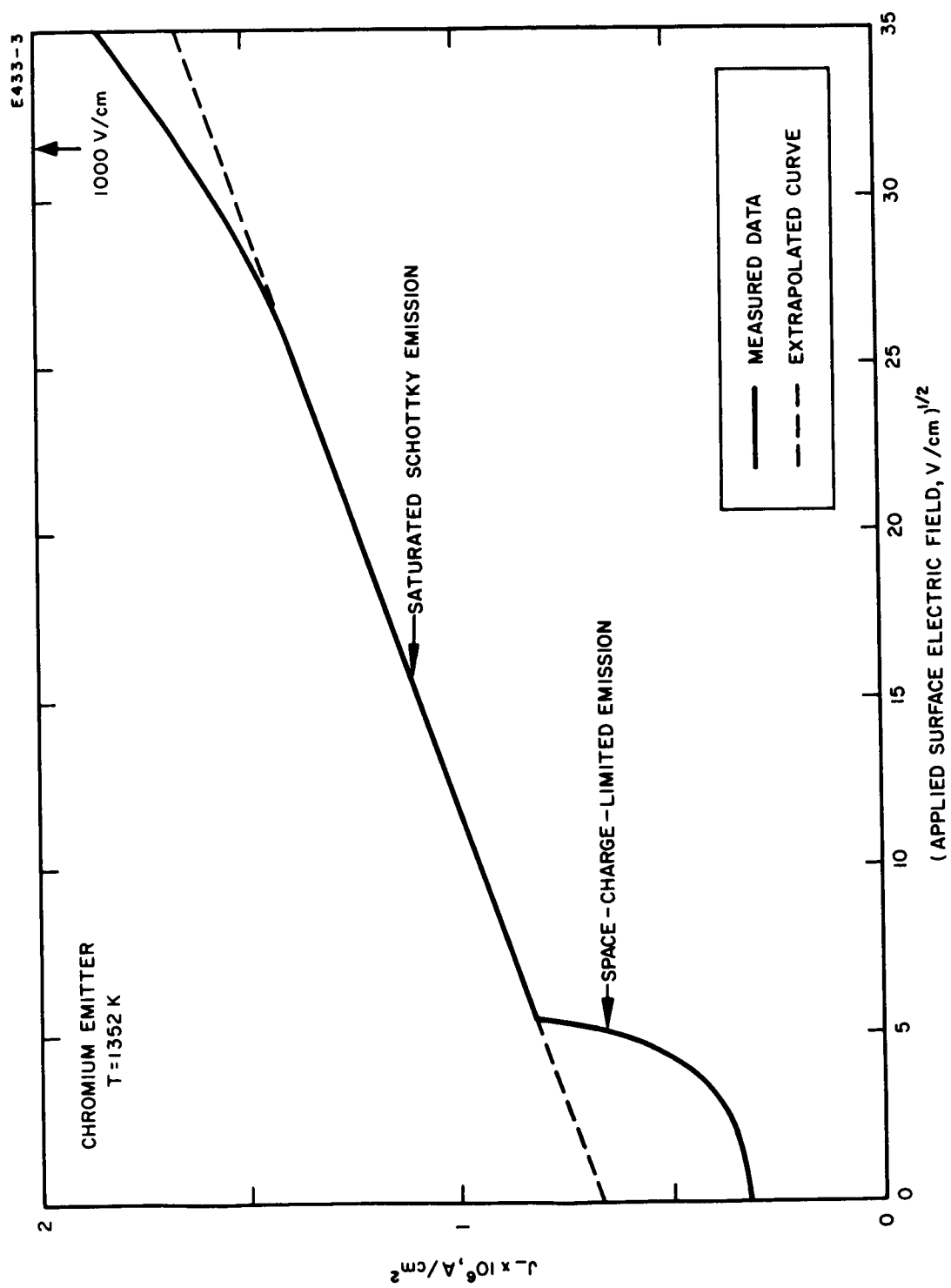
95

Fig. 29.   Thermionic electron current density versus the square root of applied surface electric field for polycrystalline chromium, $0 \leq E \leq 10^3$ V/cm.
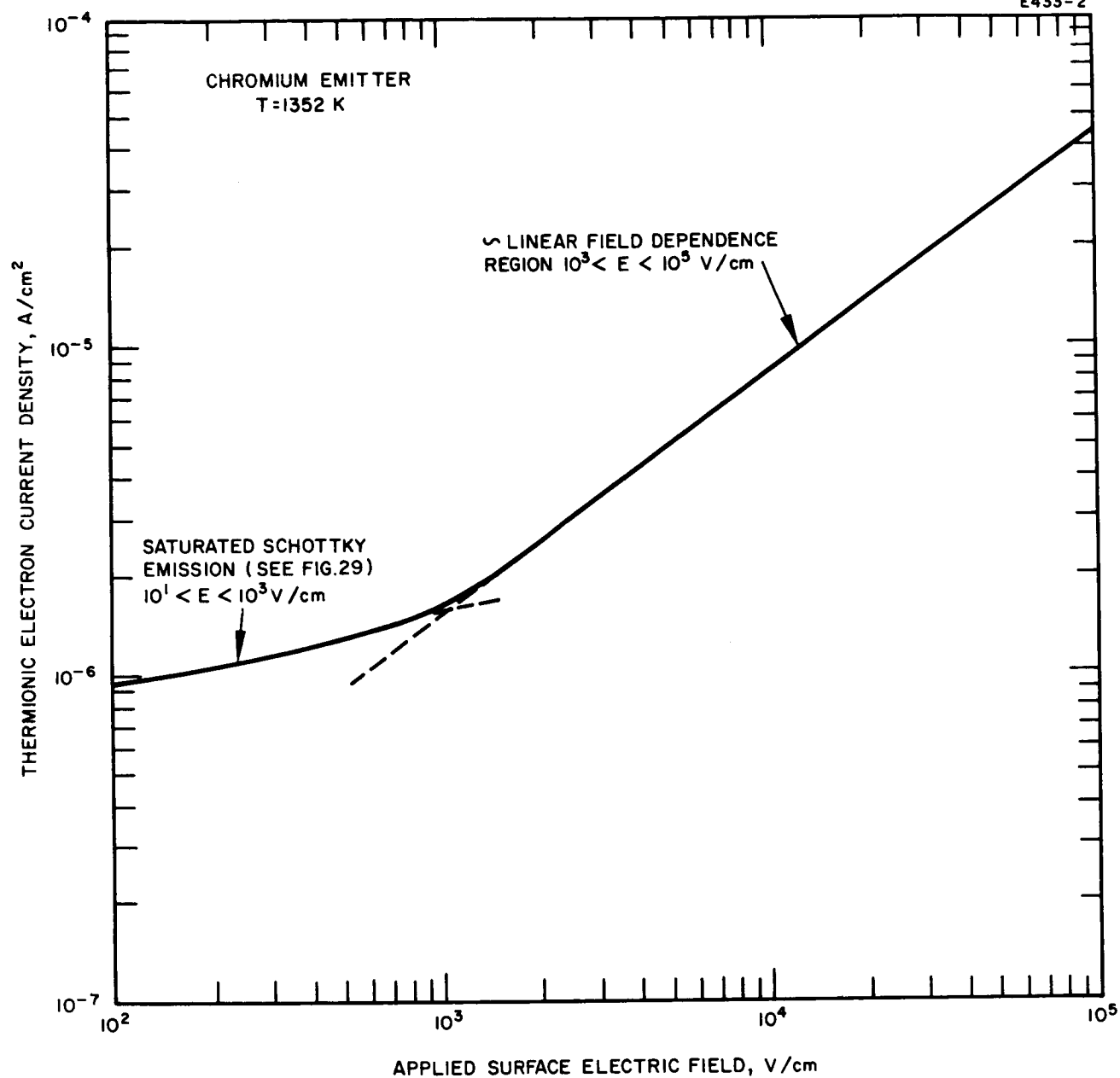
Fig. 30. Thermionic electron current density versus applied surface
electric field for polycrystalline chromium, $10^2 \leq E \leq 10^5$.

enhanced emission observed in this work was temperature dependent and was therefore probably thermionic. Furthermore, only rarely were fields greater than 10^4 V/cm applied in this work; they were used only to check for these field effects. Therefore, the whisker-growth field enhancement is not believed to account for any of the field effects observed in this work.

Early in this program, before the automatic data procurement techniques were fully developed, a very strong effect on the cesiated electron emission curves was observed and attributed to an electric field effect because increasing the field increased very greatly the emission levels under most circumstances. However, when it became possible to obtain emission curves quickly and accurately using the X-Y recorder, and when time dependent effects could be studied, a careful study of this apparent field effect was made on several emitters. It had been observed that when data were obtained at a rather slow rate and at some time after cleaning of the emitter, increases in the applied electric field had an effect on the electron S curves similar to that corresponding to increasing the cesium arrival rate. The emission level between the two limiting work function lines (arms of the S) increased rapidly with increasing electric field, ultimately resulting in the disappearance of the minimum. The special field effect and time dependent measurements have since shown conclusively that the previously observed field effects were caused by surface contamination. The emission was enhanced by the high fields, but only in the presence of contamination. The special measurements showed that the way in which this enhancement occurs is a function of the direction in which the temperature is changed, and of the time elapsed following emitter cleaning. Several cases are qualitatively illustrated in Fig. 31. When data were obtained soon enough following cleaning, the influence of applied electric field followed that predicted by the Schottky effect applied to electron S curves. In Table VI, Schottky field enhancement effect data are tabulated as a function of electric field to 10^6 V/cm, and of temperature. In Fig. 31, they are applied to a specific experimental S curve, one for molybdenum

E473-6

LOG$_{10}$ J$_-$, A/cm^2

1.1
1.2
1.3
1.4
1.5
1.6
1.7

10^{5}V/cm
10^4
10^3
10^2

-2
-3
-4
-5
-6
-7
-8
-9
-10
-11

0.5   0.7   0.9   1.1   1.3   1.5   1.7   1.9

5.4 4.8 4.4   4.0   3.6   3.2 3.0 2.8   2.6   2.4 2.3 2.2 2.1 2.0 1.9 1.8
5.0 4.6 4.2   3.8   3.4

10^3/ T(°K)

2000 1600 1400 1200 1000 900 800 700 650 600 550 500
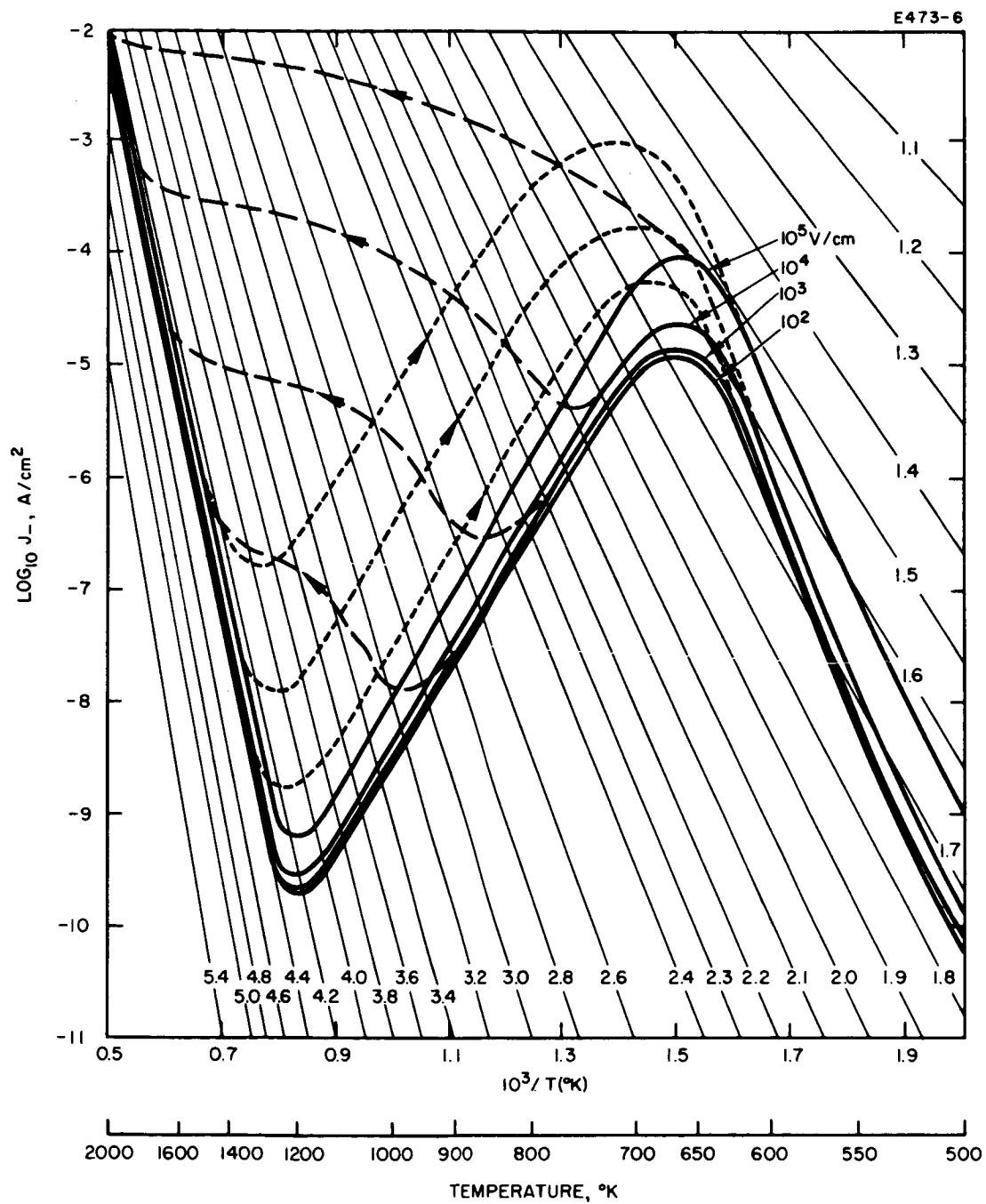
TEMPERATURE, °K

Fig. 31. Electric field effects on electron emission curves.

TABLE VI

Influence of Schottky Field Effect: Table of Values of $e^{\left|\frac{e\sqrt{eE}}{kT}\right|}$

T(K)	E, V/cm				
	10^2	10^3	10^4	10^5	10^6
500	1.09	1.32	2.41	16.1	6600
600	1.08	1.26	2.08	10.2	1270
700	1.07	1.22	1.87	7.3	535
800	1.06	1.19	1.73	5.70	245
900	1.05	1.17	1.65	4.66	133
1000	1.05	1.15	1.55	4.02	74
1200	1.04	1.12	1.44	3.19	39.3
1400	1.03	1.11	1.37	2.69	23.0
1600	1.03	1.09	1.32	2.39	15.7
1800	1.02	1.08	1.28	2.17	11.4
2000	1.02	1.07	1.25	2.00	9.0

at a cesium arrival flux of 4×10^{14} atoms/cm^2-sec, shown as solid curves for four electric field strengths. The measured curves for increasing electric field agreed with these curves within experimental error over the full range of temperature. Two additional sets of curves are shown for conditions where sufficient time had elapsed to cause some contamination. The set of dashed curves shows the combined influence of the contamination and applied field when the data are obtained by increasing the surface temperature from room temperature. The set of dotted curves shows the corresponding effect when the temperature is decreased from high temperature, but slowly enough to allow contamination to occur. The latter curves exhibit the same effects as if the cesium arrival rate had been consistently increased.

100

In a similar study of the influence of contamination (through time dependent studies) on a molybdenum silicide surface (which could also be thermally clean), some additional effects were observed, which were not seen for molybdenum. These are described with the aid of Fig. 32. It has been previously noted that it is now known that silicon was evaporating from the surface at high temperatures. Curve 1 was recorded for increasing temperature from room temperature with no preliminary high temperature cleaning. Curve 2 was recorded immediately following curve 1 for decreasing temperature starting from about 1650K with no long, high temperature cleaning; the temperature was just raised to 1650K and immediately decreased. Curves 3 and 4 are repeats of curves 1 and 2 following about a 20 min hold at about 1700K. Curve 3 is seen to be a normal S curve. Curve 1 is similar but shows the influence on some contaminant resulting from the surface sitting at room temperature prior to emission measurements. The emission level is raised for all low temperatures. For curves 2 and 4, the surface was certainly initially heavily covered with evaporating silicon. The emission level is raised at high temperatures, but the curves retrace the clean curve for a small temperature range when they first reach the clean curve; then they "tunnel" through the cesiated peak, and one retraces the clean curve again through a small temperature range. Finally, both curves exhibit a pair of low temperature, high emission peaks which are slightly displaced, depending upon the surface treatment conditions. These low temperature peaks were reproducible at other cesium arrival rates for decreasing temperature following initial high temperature operation, but they were never observed for increasing temperature. They are probably associated with the interaction of cesium with the large coverages of silicon which are recombining with the molybdenum substrate following their diffusion out onto the molybdenum surface, and evaporation from it, at the initial high temperature. In other words, the data are probably for the cesium-silicon-molybdenum tertiary system.
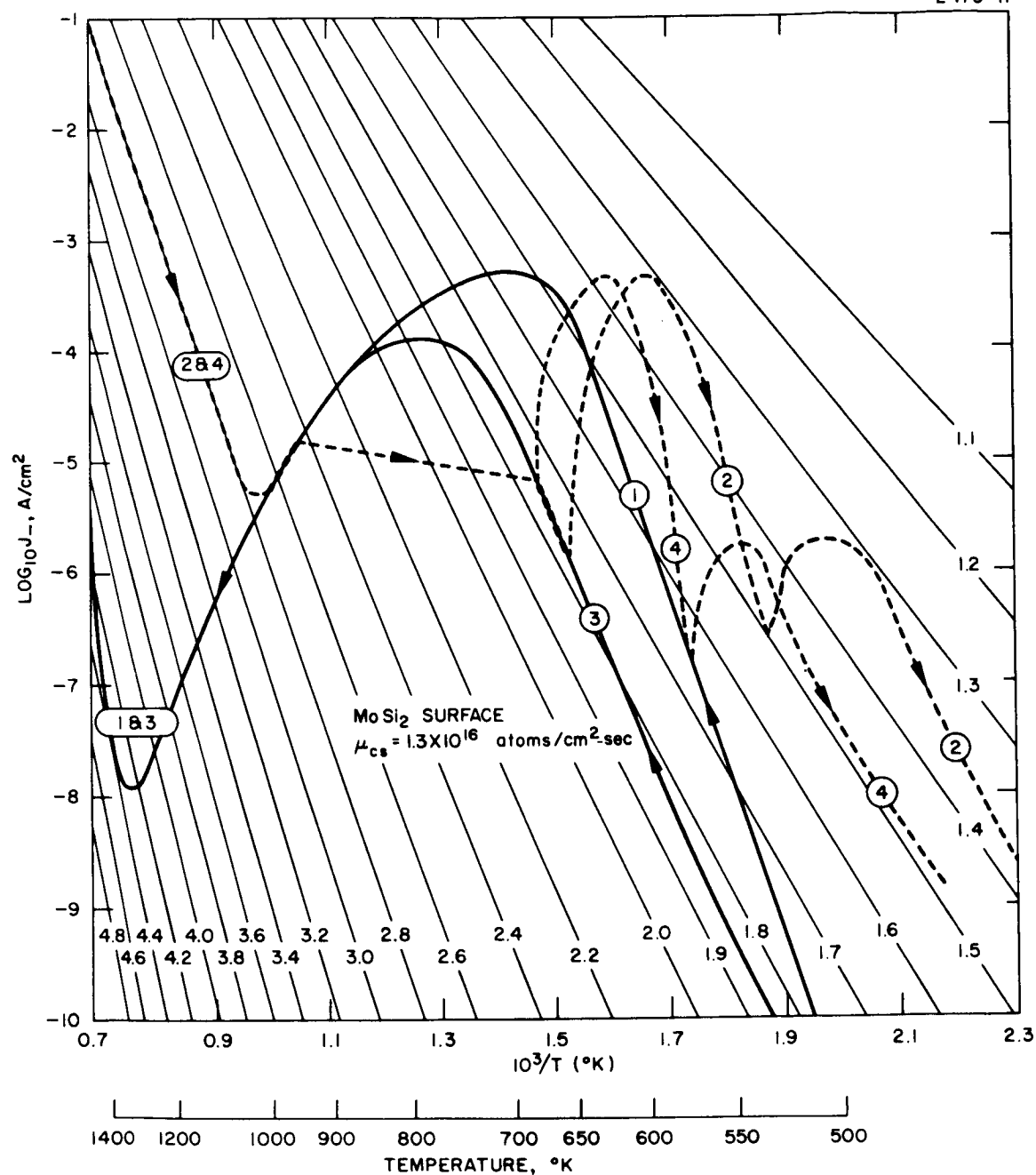
Fig. 32. Effects of contamination on electron emission for molybdenum silicide.

102

SECTION V

CONCLUSIONS

The practical goal of this work was to provide information about surfaces which can be used to select better or optimum materials for the electrodes in cesium contact ion thrustors. The work of this contract was oriented primarily toward the accel and focus electrodes. The primary variables, in addition to the surface material, were the surface temperature, the cesium arrival flux, and the applied electric field. An expanded program for next year (Contract NAS 3-6278) will include materials for cesium ionizers in addition to the accel and focus electrode surfaces, and will greatly increase the number of surfaces investigated experimentally.

The different criteria for these three electrode surfaces were established in Section II. A good ionizer surface is a porous refractory material with a slow sintering rate and good high temperature cesium compatibility. Its emission characteristics are twofold. Both a low neutral cesium fraction and a low cesium surface ionization critical temperature are important for a long-life, efficient thrustor. In Section II and the Appendix, the cesium neutral fraction properties of all the metals are analytically calculated from fundamental properties of the metals.

The conclusions are that, in terms of the neutral fraction, iridium should be the best surface, with rhenium a good second. If the operating point of 15 mA/cm^2 of cesium ions at a cesium neutral fraction of 0.1% is used as a minimum acceptable condition for very long life operation, rhodium is barely acceptable and osmium, ruthenium, and tungsten are just short of the requirement, but acceptable for shorter life applications. All other metals are entirely unacceptable. Two higher work function metals, platinum and palladium, are not given consideration because of their melting point temperatures and sintering rates.

The criterion of critical temperature can only satisfactorily be determined experimentally. The critical temperature envelope (variation with ion current density) for cesium ionization measured in this work provides the necessary information. None of the above-named low-neutral-fraction metals was studied on this contract, but a number of them will be investigated on Contract NAS 3-6278.

A good focus electrode surface, or the nonionizing portion of a continuous ionizer surface in a thrustor design not employing independent focus electrodes, has characteristics diametrically opposed to those for the ionizer. A low cesium ionization efficiency and a high surface ionization critical temperature are desirable. A surface with a low cesiated work function at the operating temperature will result in a low cesium ion current density.

A refractory surface with a low vacuum work function (well below the ionization potential of cesium, e.g., 3.5 eV) will always exhibit a low work function. The analysis of Section II showed only two metals, hafnium and thorium, which have suitable vacuum work functions. Fabricating electrodes for large ion thrustors from either of these metals would be difficult. Some refractory metal compounds, the borides, carbides, and silicides, for which some evidence of low work function existed, were also considered as possible candidates for non-ionizing surfaces. Two such surfaces, molybdenum silicide and tantalum boride, were investigated on this program. Both exhibited relatively high vacuum work functions, rather than low ones. It is believed that these very stable compound crystals should have these observed high effective vacuum work functions and that the previously reported data[9] are in error because of poor vacuum conditions and changing contamination. The cesiated emission properties of one, molybdenum silicide, were investigated in detail. It was a relatively good cesium ionizer and does not qualify as a desirable nonionizing surface. Tantalum boride was found to be a hard, brittle, fragile surface, which caused the failure to obtain any cesiated emission measurements. These properties together with the high vacuum work function make it an unlikely candidate.

The carbides of zirconium and molybdenum and the silicides of tungsten and tantalum will be investigated on Contract NAS 3-6278, but the results for the two compounds studied on this contract cast suspicion on the previously reported data for all of these compounds.

Considering the other materials examined in this work, the data of Fig. 14 show that, at any given temperature, lower cesium ion current densities are emitted by alumina and by iron (under the condition generally exhibited by the iron surfaces studied). Alumina is only slightly better than the other materials; the particular iron data are orders of magnitude better. Some qualifications are noted in both cases. The alumina data were obtained for one of many kinds of commercial porous alumina of 99.5% purity. Therefore it is uncertain that these data would apply to any arbitrary commercial alumina. It would be better to test a higher density, higher purity, better defined alumina product. This will be done on Contract NAS 3-6278 when a machined piece of Lucalox will be studied. Data obtained by H. L. Garvin (this laboratory) indicate the possibility of even lower cesium current densities from Lucalox. The iron sample, for which the reported data were obtained, was 99.999% pure and the very low ion emission data were obtained after the sample was heated to 1200C in the presence of cesium, after which the electron work function was always observed to be 3.5 eV. It is uncertain whether an iron surface of lower purity not heated in a cesium atmosphere will exhibit this 3.5-eV work function in a cesium atmosphere.

A major problem regarding iron as the nonionizing surface concerns the vapor pressure and evaporation rate. Iron was not considered a candidate for the focus electrode for this reason. At a temperature of 1000C (or 1300K), the vapor pressure of iron is 10^{-6} Torr, and the evaporation rate must be considered with respect to the length of the required operation, and the possible capability for cooling this electrode.

A suitable accel electrode material must fulfill the various requirements discussed in Section II. The only likely candidates from preliminary considerations are copper, beryllium, and some of the

Transition I metals. Data are reported here for copper, iron, and chromium. The copper data are tentative, and copper surfaces will be investigated early in Contract NAS 3-6278. The chromium data are subject to some question. After being heated in the cesium atmosphere, pure iron exhibited extraordinary properties. While in one case, for which the background pressure was unsatisfactory, the cesiated iron electron emission was high, the two cleaner cases resulted in no observable cesiated emission peak and therefore in many orders of magnitude lower emission current densities than for any other material. If this condition could be produced in an ion thrustor, an ideal electrode surface would exist.

In Fig. 33 are displayed comparative electron emission curves for all of the materials studied at one cesium arrival flux, 2.5×10^{15} atoms/cm^2-sec. Ignoring the unusual iron data (which make it a potentially excellent candidate), and using the more normal iron data curve, the following comparisons can be made (at this one arrival flux). The lowest electron current density below 800K is from molybdenum silicide; and above 800K, molybdenum. However, neither material is suitable for accel electrodes from the point of view of the influence of sputtering onto the ionizer. Comparing copper, chromium, and iron, iron is best to 750K, above which chromium or copper is better to 1050K, above which iron is again better. Clearly the choice depends on the operating temperature of the electrode if minimization of electron emission is desired.

While the experimental measurements with these few electrode candidate materials have not resulted in the discovery of any outstandingly better electrode materials, they have definitely eliminated some materials from consideration by showing unsuitable characteristics, and they have explained some of the operating characteristics and behavior patterns of cesium ion thrustors being ground tested in the laboratory. They have also led to certain particular electrode design criteria, e.g., minimizing certain electrode areas, and they have provided valuable information about operating temperature regimes for the electrodes.
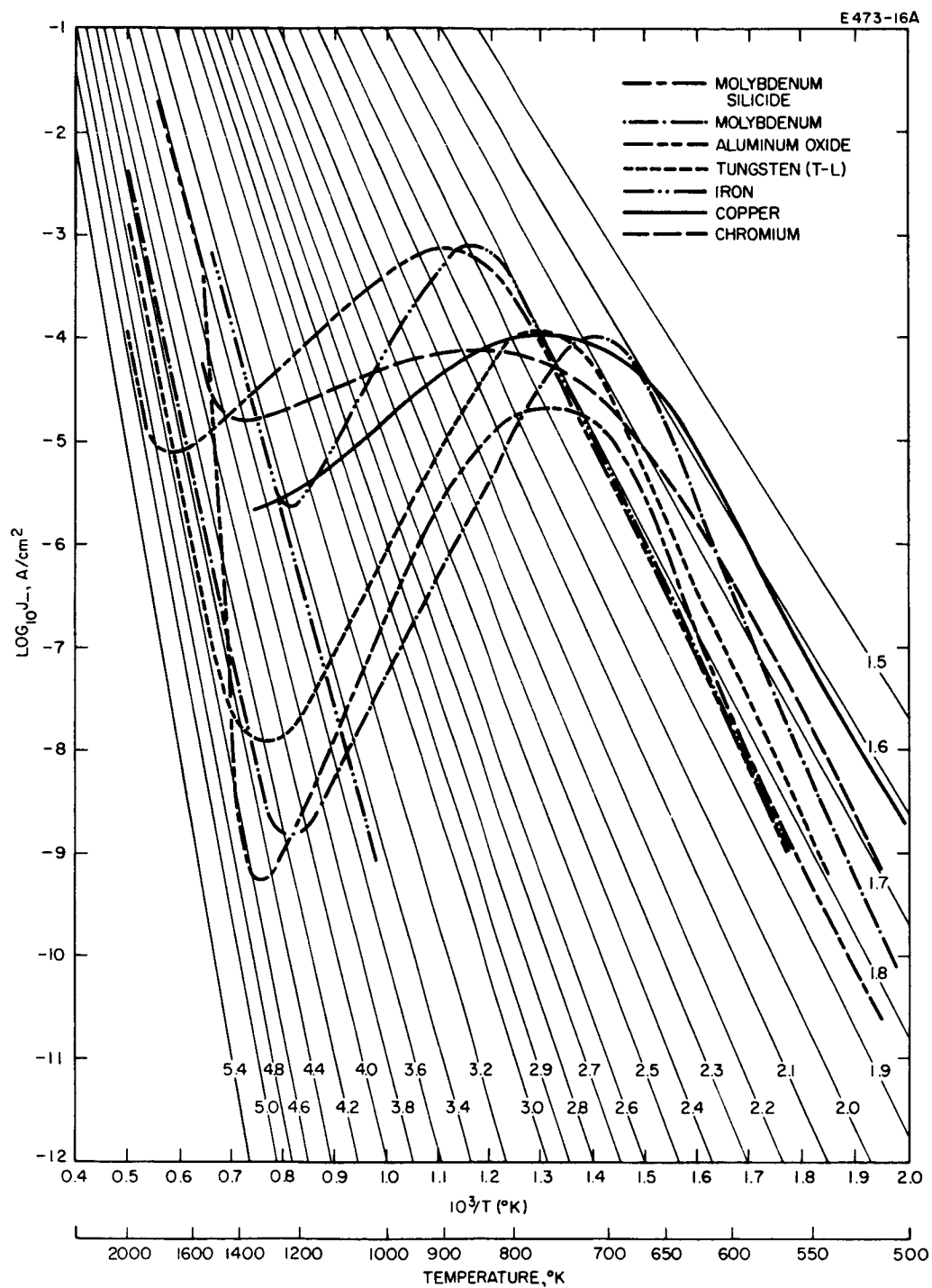
Fig. 33. Comparative electron emission curves for various substrates at cesium arrival flux of 2.5 x 10^15 atoms/cm²-sec.

SECTION VI

FUTURE PLANS

This work is to be continued in 1965 under Contract NAS 3-6278. The materials to be studied are (tentatively): (1) clean and oxygenated copper, (2) beryllium, (3) Lucalox (Al_2O_3), (4) 304 stainless steel, (5) molybdenum carbide, (6) zirconium carbide, (7) iridium, (8) nickel, (9) platinum, (10) osmium, (11) titanium, (12) tungsten silicide, (13) tantalum silicide, (14) rhenium, (15) tungsten, and (16) niobium. It is hoped that time will be available to complete the study of tantalum diboride.

SECTION VII

CONTRIBUTING PERSONNEL

The persons associated with the research program carried out under this contract, and their contributions, were

R. G. Wilson	— Project Scientist
P. J. Coane	— Fabrication and operation of the vacuum system, emission measurements, and data reduction and analysis
J. D. Montross	— Fabrication and processing of experimental tubes and special materials procurement and handling
G. H. Guss	— Computer Programmer
R. Kesterson and C. H. Fetters	— Glass blowing associated with experimental tubes and vacuum system
G. W. Childs	— Equipment supply and maintenance
W. E. McKee and J. M. Hammond	— Refractory compound surface fabrication
E. Senkovits	— X-ray diffraction measurements

Only the first two persons listed contributed full time to the program.

REFERENCES

1.   Summary Report, Phase III, NAS 5-517, March 1964.

2.   Handbook of Chemistry and Physics, 44th ed. (1962-63) (Chemical Rubber, Cleveland, 1962).

3.   American Institute of Physics Handbook, 2nd ed. (McGraw-Hill, New York, 1963).

4.   R. T. Sanderson, Chemical Periodicity (Rheinhold, New York, 1960).

5.   R. E. Honig, RCA Review 23, 567 (1962).

6.   O. Almén and G. Bruce, Nuclear Instruments and Methods (North-Holland, Amsterdam, 1961), Vol. II, pp. 257 and 279.

7.   G. K. Wehner, in Ionization Phenomena in Gases (North-Holland, Amsterdam, 1962), p. 1141; also B. Perovic, p. 1172.

8.   K. B. Cheny, E. E. Rogers, and E. T. Pitkin, ARL Report 63-125, Contract AF 33(616)-8120, 1963.

9.   S. V. Yermakov and B. M. Tsarev, Radioteckhnia i Elektronika 7, 1956 (1962).

10. R. G. Wilson, "Electrode Surface Physics Research," Quarterly Progress Report No. 1, Contract NAS 3-5249, 27 February 1964 through 31 May 1964.

11. R. L. Aamodt, L. J. Brown, and B. D. Nichols, J. Appl. Phys. 33, 2080 (1962).

12. R. P. Little and W. T. Whitney, J. Appl. Phys. 34, 2430 (1963).

APPENDIX

THEORY AND ANALYTICAL CALCULATIONS

LIST OF SYMBOLS

α	polarizability, cm^3 or $\mathring{A}^3$
$\bar{\alpha}$	reflection coefficient or sticking probability, unitless
β	surface ionization efficiency, unitless
θ	surface coverage, unitless
λ	desorption energy, eV
μ	arrival flux, atoms/cm^2-sec
ν	desorption flux, atoms/cm^2-sec
σ	surface concentration, atoms/cm^2
τ	mean residence time, sec
ϕ	effective work function, eV
χ	electronegativity, eV
χ_o	distance of adatom from substrate at which probability of electron transition vanishes, approximately r, cm or $\mathring{A}$
ψ	angle, unitless
ω	fundamental vibration frequency, sec^{-1}
d	diameter, cm or $\mathring{A}$
E	applied surface electric field, V/cm
g	statistical weight, unitless
G	shape factor (nonarbitrary), unitless
$H_s \Delta H_s$	sublimation energy per atom, eV/atom or kcal/mole
j^v	vibration partition function, unitless
J	current density, A/cm^2

k   Boltzmann constant, $eV/atom\text{-}^{\circ}K$

m   effective dipole moment, coul-m

M   dipole moment, coul-m

NF   neutral fraction, unitless

r   covalent radius, cm or $\overset{\circ}{A}$

S   orbital strength; entropy (ΔS is change in entropy), unitless; $eV/atom\text{-}^{\circ}K$

T   surface temperature, degrees

v   valence, unitless

V_i ionization potential (energy), eV

subscripts

o   atom

+   ion

-       electron

c   ion critical (temperature) point

NOTE: All parentheses indicate the value of θ for which the function is evaluated; (0) corresponds to the bare substrate and (1) refers to the bulk adsorbate.

Of considerable significance in this program are atom and ion desorption energies for cesium on a variety of metal surfaces, non-refractory as well as refractory; the atom and ion desorption energies for a variety of metals from a tungsten substrate and other refractory metals; the equilibrium surface coverage of any one metal on another as a function of arrival flux, surface temperature, and atom and ion desorption energies; the variation of surface work function of various adsorbate-substrate combinations as a function of surface coverage; and the critical temperatures for saturated cesium-ion emission from a variety of metal surfaces.

EQUILIBRIUM SURFACE COVERAGE

The dependent variable in the expressions for the three fundamental (not applied, as are T and E) surface physics quantities, ϕ, λ_o, and λ_+, is the surface coverage θ. The most general expression for θ, including the influence of all strengths of applied field and an ion component of incident flux, is

$$\theta = \frac{\overline{a}\mu_o + \mu_+}{\sigma(1)} \left(\frac{h}{kT}\right)\left[1 - e^{-\left(\frac{h\omega}{kT}\right)}\right]^{-1} e^{-\left(\frac{\Delta S}{k}\right)}\left\{e^{-\left[\frac{\lambda_o(\theta) + \frac{1}{2}\alpha_o(1) E^2 + eE \chi_o}{kT}\right]}\right.$$

$$\left. + \frac{g_o(1)}{g_+(1)} e^{-\left[\frac{\lambda_+(\theta) + \frac{1}{2}\alpha_+(1) E^2 - e\sqrt{eE}}{kT}\right]}\right\}^{-1} . \qquad (A-1)$$

This expression results from the fundamental definition of θ, or

$$\theta \equiv \frac{\sigma}{\sigma(1)} = \frac{\mu_{total} \tau_{total}}{\sigma(1)} . \qquad (A-2)$$

119

The total arrival flux may be composed of an ion component and a neutral component. In general, there is a reflection coefficient or a sticking probability which reduces the effective neutral component.

$$\mu = \bar{\alpha} \mu_o + \mu_+ \quad . \tag{A-3}$$

In the most general case, when both atomic and ionic states of the adsorbate are considered, the general expression for the adsorbate mean residence time is

$$\tau = \left[\frac{1}{\tau_o} + \frac{g_o^{(1)}}{g_+^{(1)}} \frac{1}{\tau_+} \right]^{-1} \quad . \tag{A-4}$$

g_+/g_o is the statistical weight ratio of the adsorbate ionic to atomic states, which is 1:2 for the alkali metals.

For a metal substrate, the activation energy for surface migration (or diffusion) is low compared with that for evaporation. Surface migration therefore maintains equilibrium among the adsorbate particles. Under these conditions τ_i is obtained from the isotherm of the adsorbate particles

$$\tau_i(\theta, E) = \left(\frac{h}{kT} \right) j^v \, e^{\left(\frac{\lambda_i(\theta, E)}{kT} - \frac{\Delta S}{k} \right)} \tag{A-5}$$

which is a form of the Arrhenius equation. j^v is the statistical mechanics vibration partition function which is, in any number of dimensions,

$$j^v = \left[1 - e^{-\left(\frac{h\omega}{kT} \right)} \right]^{-1} \quad . \tag{A-6}$$

120

exp$[-(\Delta S/k)]$ is an entropy term discussed in more detail in Ref. A-1. It is related to the statistical population density in the adsorbed layer and is influenced by the population and depopulation of the adsorbed layer by the adsorption-desorption process. Its value is unity at $\theta = 0$ and increases with increasing θ. However, its magnitude is limited by the formation of multiple layers, which starts to occur well before the first monolayer is completed (about 0.6). Therefore it never reaches the potential large values at $\theta = 1$, because, before $\theta = 1$, multiple layers have formed at some locations and the mass condensation mode sets in. This term is near unity for small θ, such as in the region of θ_c which is below 0.05. This term can account for differences between experiment and theory for values of θ approaching and greater than 0.5 and should be calculated when a rigorous comparison with theory is desired.

$$\frac{\Delta S}{k} = \ln\left(\frac{A_t}{A_f}\right)\theta \frac{\partial}{\partial\theta}\left[\ln\left(\frac{A_t}{A_f}\right)\right] \qquad (A-7)$$

where A_t is the total surface area available for adsorption and A_f is the free area available for translation. Three models for calculating A_f are discussed in Ref. A-1.

The θ and E dependences of λ_o and λ_+ can be written explicitly. The θ dependences are discussed at length in subsequent sections. The electric field dependences are written below.

$$\lambda_o(\theta, E) = \lambda_o(\theta) + \frac{1}{2} a_o(1) E^2 + eE X_o \qquad (A-8)$$

and

$$\lambda_+(\theta, E) = \lambda_+(\theta) + \frac{1}{2} a_+(1) E^2 - e\sqrt{eE} \qquad (A-9)$$

where the $+(1/2)\alpha E^2$ terms are increases resulting from the inter-action of an inhomogeneous field with the polarized adsorbate, EX_o is the shift in the ionization energy caused by the presence of the electric field, and $-e\sqrt{eE}$ is a reduction in λ_+ only, resulting from the same reduction in the image charge forces between the ion and the substrate surface. If μ_+ is negligible or nonexistent, as it is in the case under consideration and in most cases, and if $E \lesssim 10^6$ V/cm, eq. (1) reduces to

$$\theta = \frac{\overline{\alpha}\mu}{\sigma(1)}\left(\frac{h}{kT}\right)\left[1 - e^{-\left(\frac{h\omega}{kT}\right)}\right]^{-1} e^{-\left(\frac{\Delta S}{k}\right)}\left\{ e^{-\frac{\lambda_o(\theta)}{kT}}\right.$$

$$\left. + \frac{g_o(1)}{g_+(1)} e^{\frac{\lambda_+(\theta) + e\sqrt{eE}}{kT}} \right\}^{-1} , \qquad (A-10)$$

which is the expression applicable in this analysis. It is noted that θ itself occurs as an independent variable in two exponents. Therefore, θ cannot be independently solved for. However, once $\lambda_o(\theta)$ and $\lambda_+(\theta)$ curves are calculated from the expressions in the subsequent sections, an iterative process can be used to find a value of θ which satisfies (A-10). This can be conveniently done with a fast computer.

COMPOSITE SURFACE WORK FUNCTION

The expression

$$\phi(\theta) = \phi(0) - [\phi(0) - \phi(1)] [1 - G(\theta)]$$

$$- \frac{C_1 \theta G(\theta) \sigma(1) [\phi(0) - \phi(1)] \left\{1 - \dfrac{1}{2\sigma(0) [r(0) + r(1)]^2}\right\}^{1/2}}{\left\{1 + \dfrac{\alpha(1)}{[r(0) + r(1)]^3}\right\} \left\{1 + 9 \alpha(1) [\sigma(1) \theta]^{3/2}\right\}} \qquad (A-11)$$

is written with the aid of Gyftopoulos and Levine.[A-2] This expression results from the superposition of a dipole barrier and an electronegativity barrier. The electronegativity barrier $\phi_e(\theta)$ is assumed proportional to the electronegativity of the composite surface

$$\phi_e(\theta) = C_2 + C_3 X(\theta) \quad . \tag{A-12}$$

The application of appropriate boundary conditions on $\phi_e(\theta)$ and $d\phi_e(\theta)/d\theta$ at $\theta = 0$ and 1 results in

$$\phi_e(\theta) = \phi(1) - [\phi(0) - \phi(1)] \, G(\theta) \tag{A-13}$$

where $G(\theta)$ is a polynomial in θ which is given by the boundary conditions or may be known empirically from contact potential measurements. This polynomial has been recently derived by an independent technique.[A-3]

The dipole barrier $\phi_d(\theta)$ results from polarization of both the adsorbate and substrate atoms resulting from interelectron bonding which is partly ionic and partly covalent, and is related to the electronegativity. The dipole moment of a single adatom-substrate dipole $M(0)$ is calculated. A square array of adatoms and therefore of dipoles is assumed, and the depolarizing field and the effective dipole moment $m(\theta)$ are calculated.

$$\phi_d(\theta) = -\frac{m(\theta) \, \sigma(1) \, \theta}{\epsilon_o} = -\frac{\theta \, G(\theta) \, \sigma(1) \, M(0)}{\epsilon_o \left\{ 1 + \dfrac{9\alpha(1) \, [\sigma(1) \, \theta]^{3/2}}{4\pi \, \epsilon_o} \right\}} \tag{A-14}$$

where

$$M(0) = 4 M(0-1) \cos \psi = \frac{C_4[\chi(0) - \chi(1)] \left\{ 1 - \dfrac{1}{2\sigma(0)[r(0) + r(1)]^2} \right\}^{1/2}}{\left\{ 1 + \dfrac{a(1)}{4\pi\epsilon_o[r(0) + r(1)]^3} \right\}} .$$

$$(A-15)$$

Equation (A-11) has been used to calculate the surface work function as a function of surface coverage of composite surfaces of the adsorbate cesium on about 50 substrate elements, of about 50 adsorbates on a tungsten substrate, and of 14 adsorbate elements on the three additional substrate metals (molybdenum, hafnium, and platinum). C_1 and all other constants to be used are functions only of the system of units employed. Curves of $\phi(\theta)$ for 50 adsorbates on a tungsten substrate are plotted in Figs. A-1 through A-8. Curves of $\phi(\theta)$ for cesium on 14 substrates are plotted in Figs. A-9 and A-10.

ATOM AND ION DESORPTION ENERGIES

The expression for the ion desorption energy

$$\lambda_+(\theta) = \lambda_o(\theta) + V_i(1) - \phi(\theta) \qquad (A-16)$$

derived from application of the Born-Haber energy cycle is commonly used when $\lambda_o(\theta)$ can be obtained by explicit calculation. It should be realized that in this expression the surface ionization potential V_s, which occurs in the energy cycle, is implicit within $\lambda_o(\theta)$. This expression is used herein because $\lambda_o(\theta)$ and $\phi(\theta)$ are calculated explicitly.
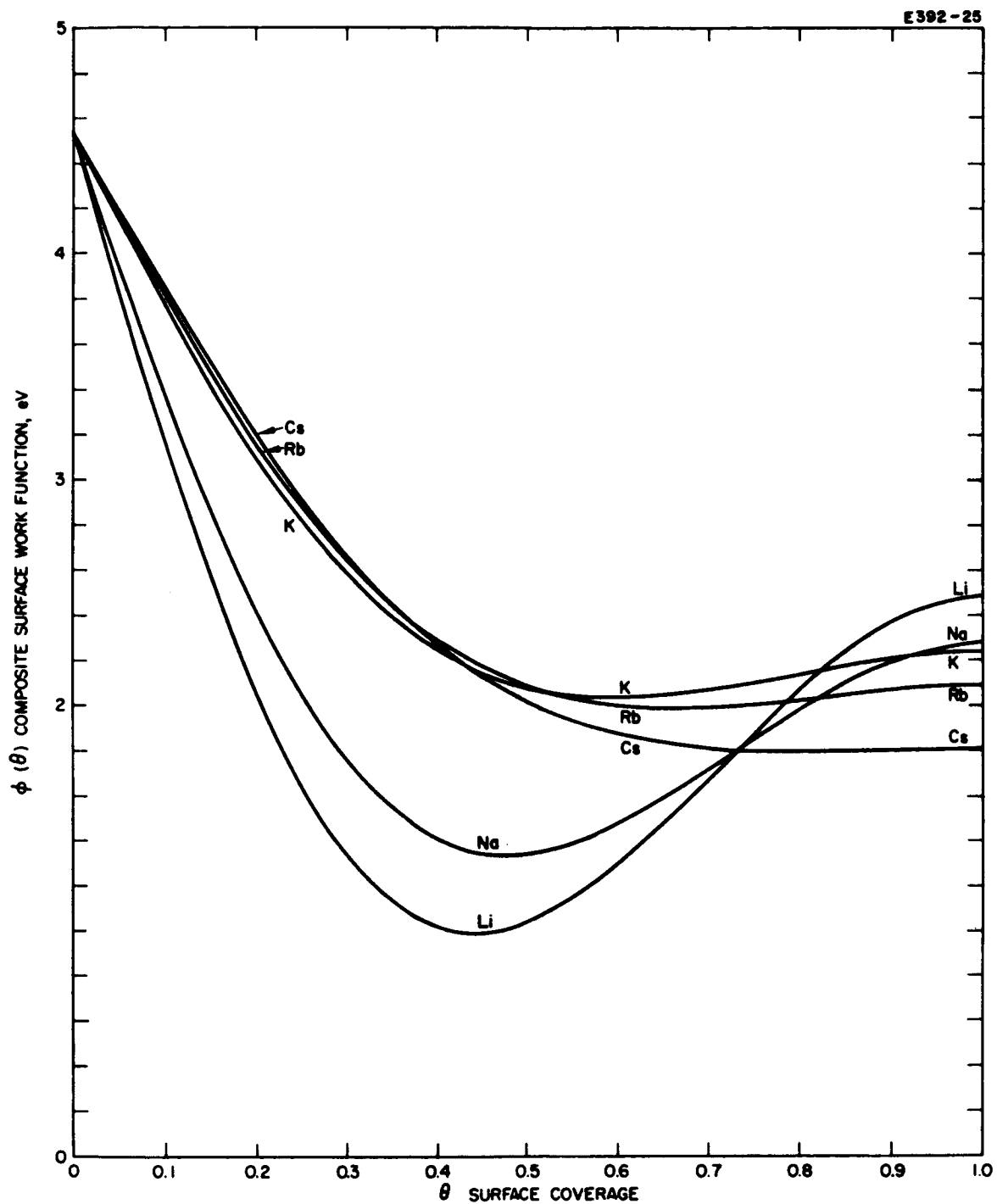
124

Fig. A-1. Computer calculated composite surface work functions versus surface coverage for the alkali metals on tungsten.
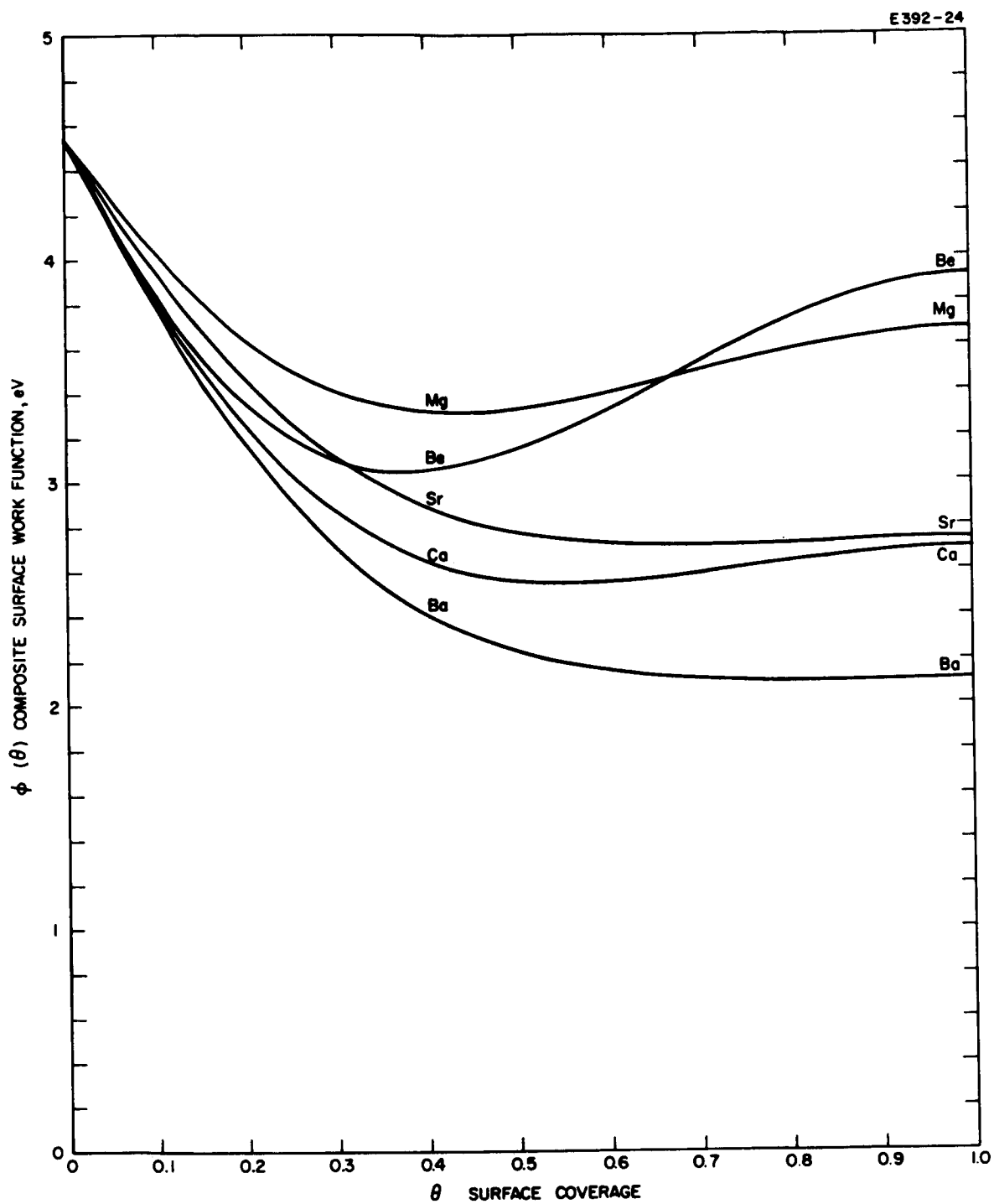
Fig. A-2. Computer calculated composite surface work functions versus surface coverage for the alkaline earth metals on tungsten.
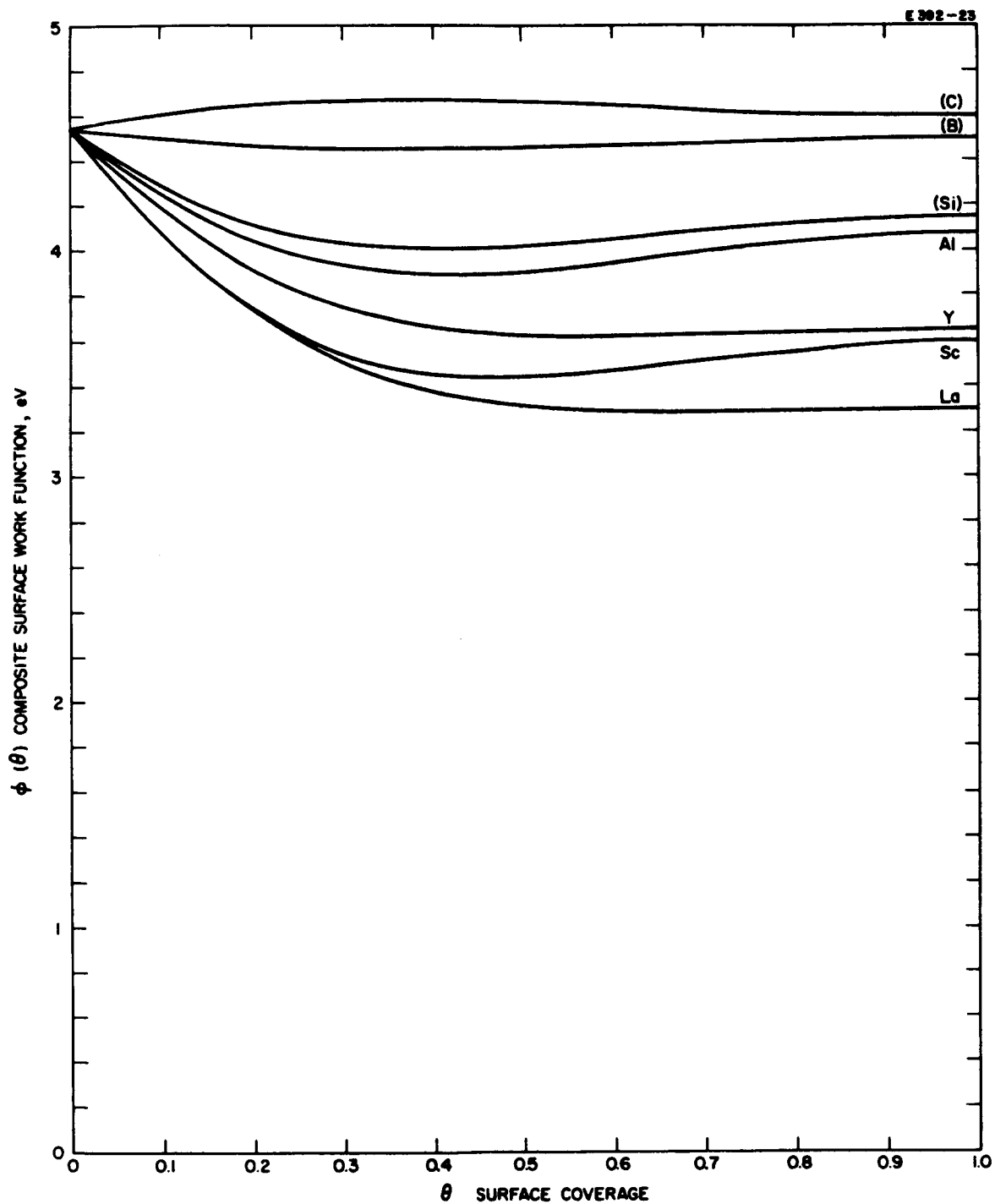
Fig. A-3. Computer calculated composite surface work functions versus
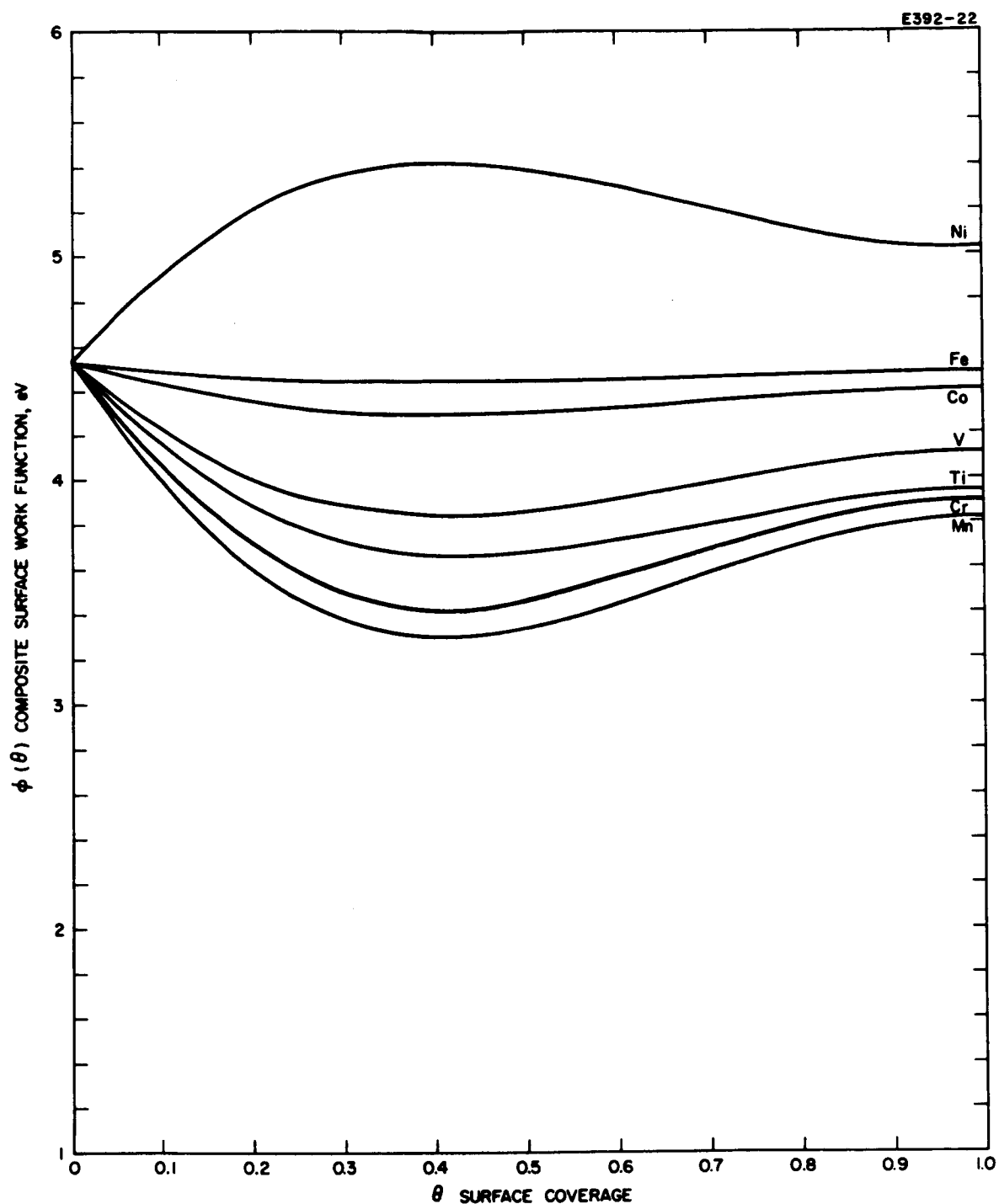surface coverage for the Period III and IV elements on tungsten.

Fig. A-4. Computer calculated composite surface work functions versus surface coverage for the transition Group I metals on tungsten.

Fig. A-5. Computer calculated composite surface work functions versus surface coverage for the transition Group II metals on tungsten.

Fig. A-6. Computer calculated composite surface work functions versus surface coverage for the transition Group II metals on tungsten.
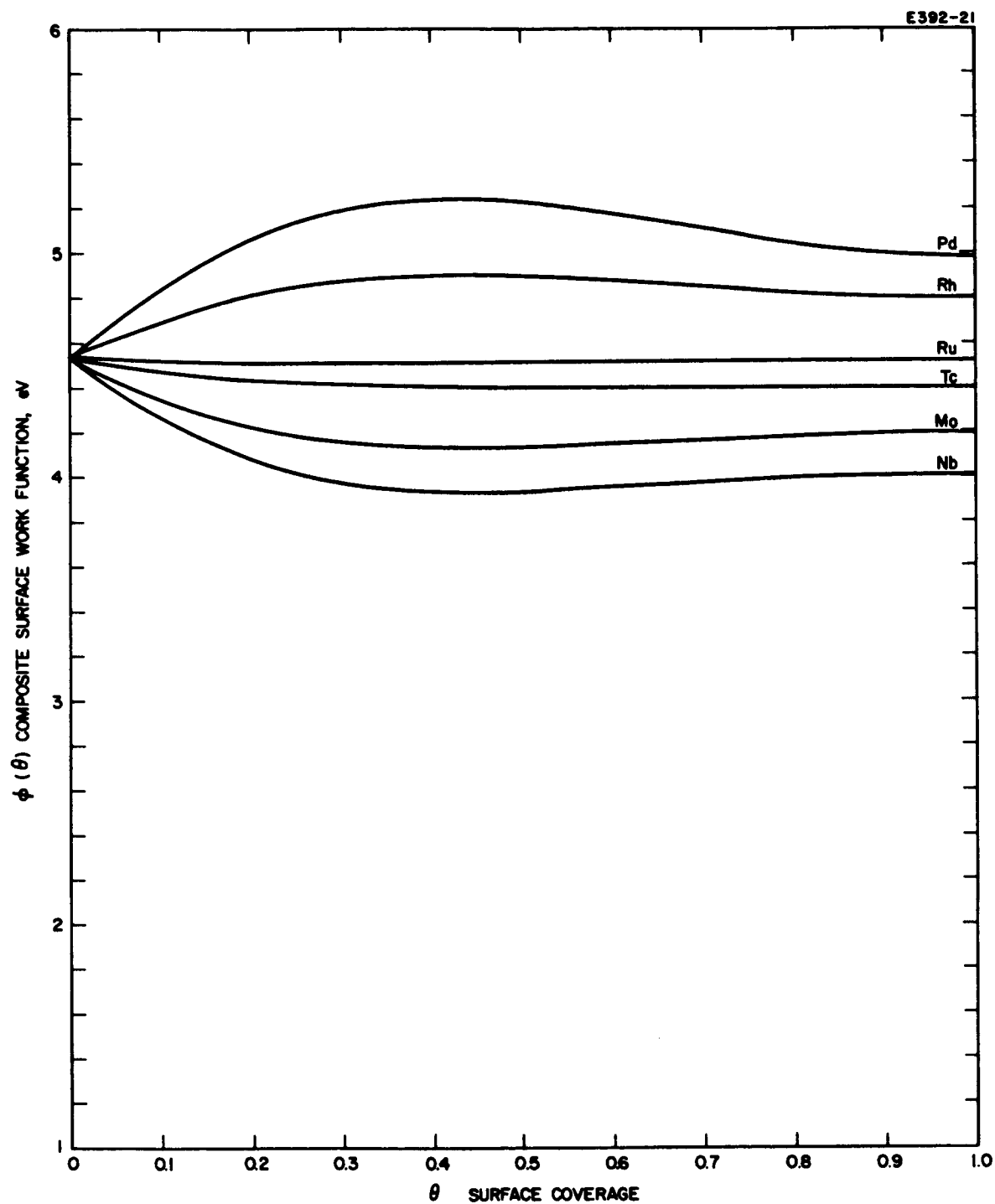
130

Fig. A-7. Computer calculated composite surface work functions versus
surface coverage for some medium weight metals on tungsten.

Fig. A-8. Computer calculated composite surface work functions versus surface coverage for some heavy and noble metals on tungsten.

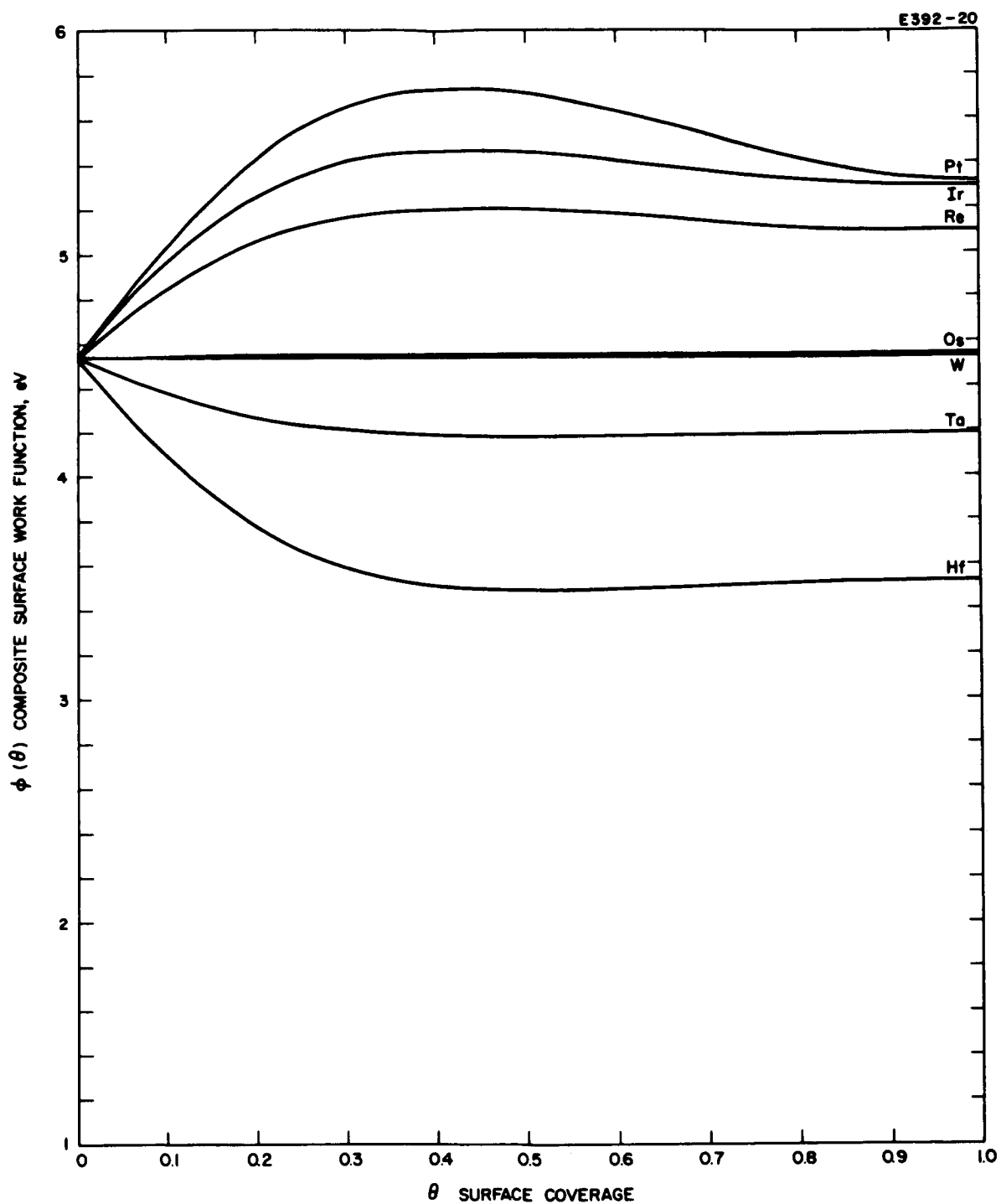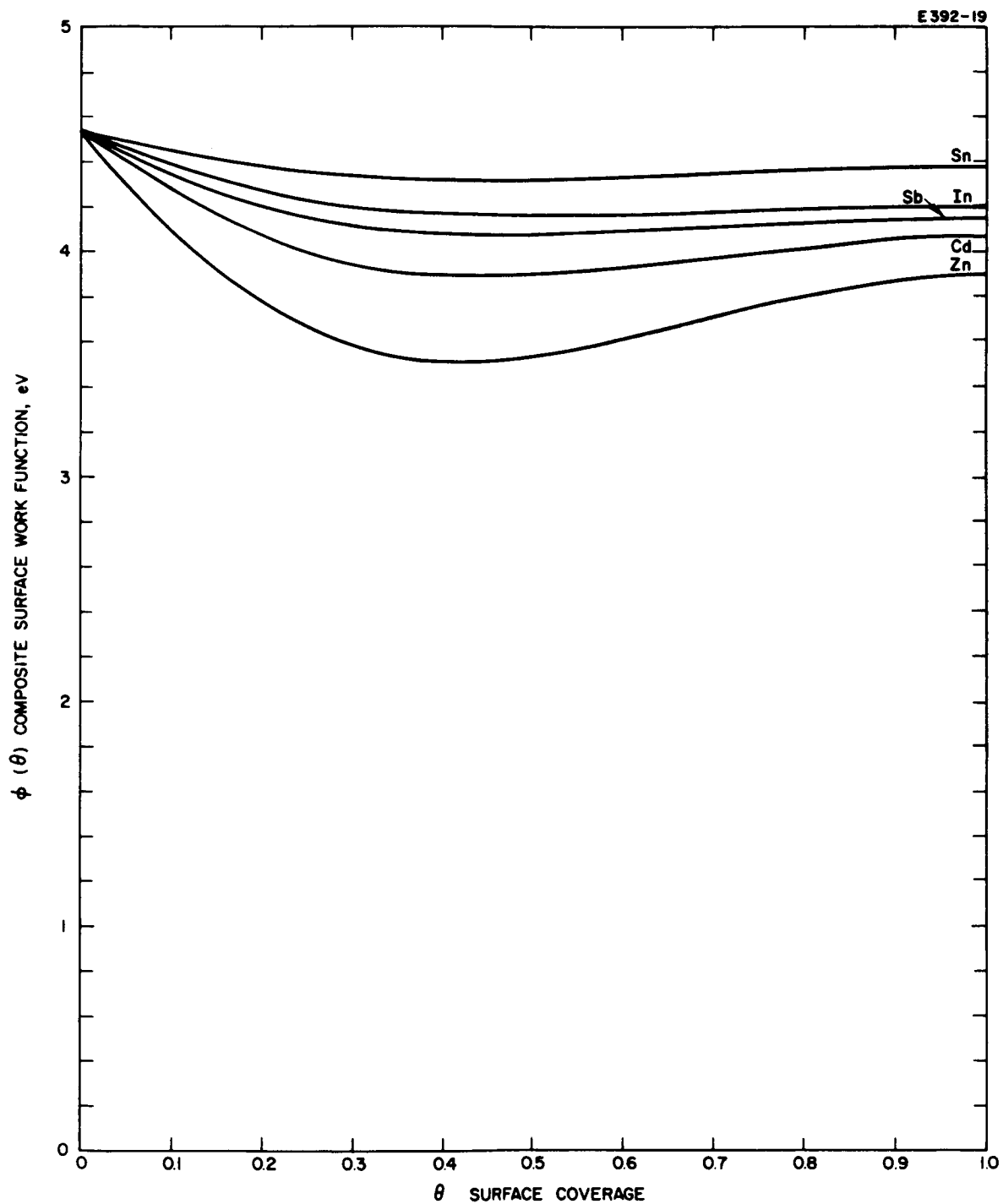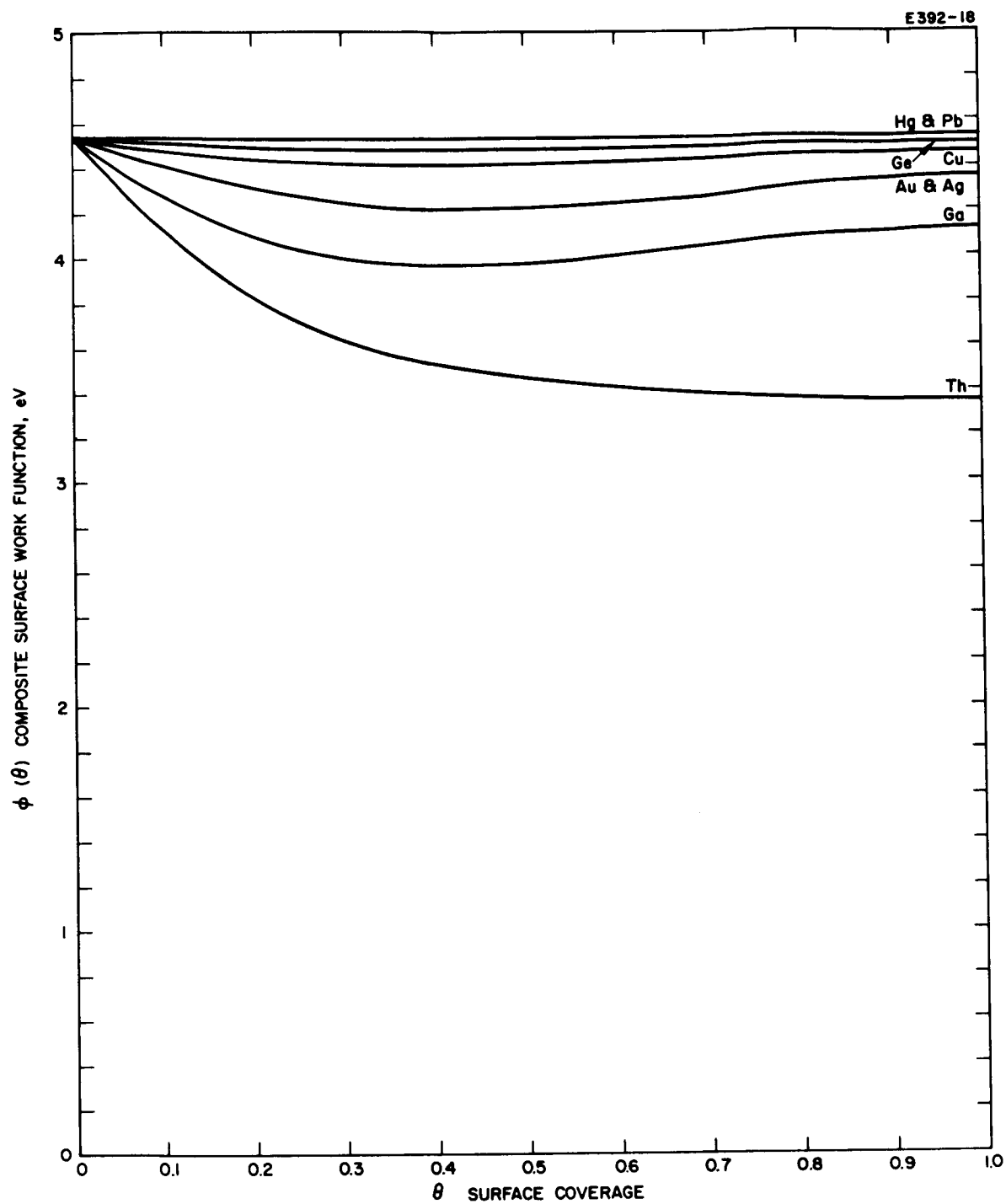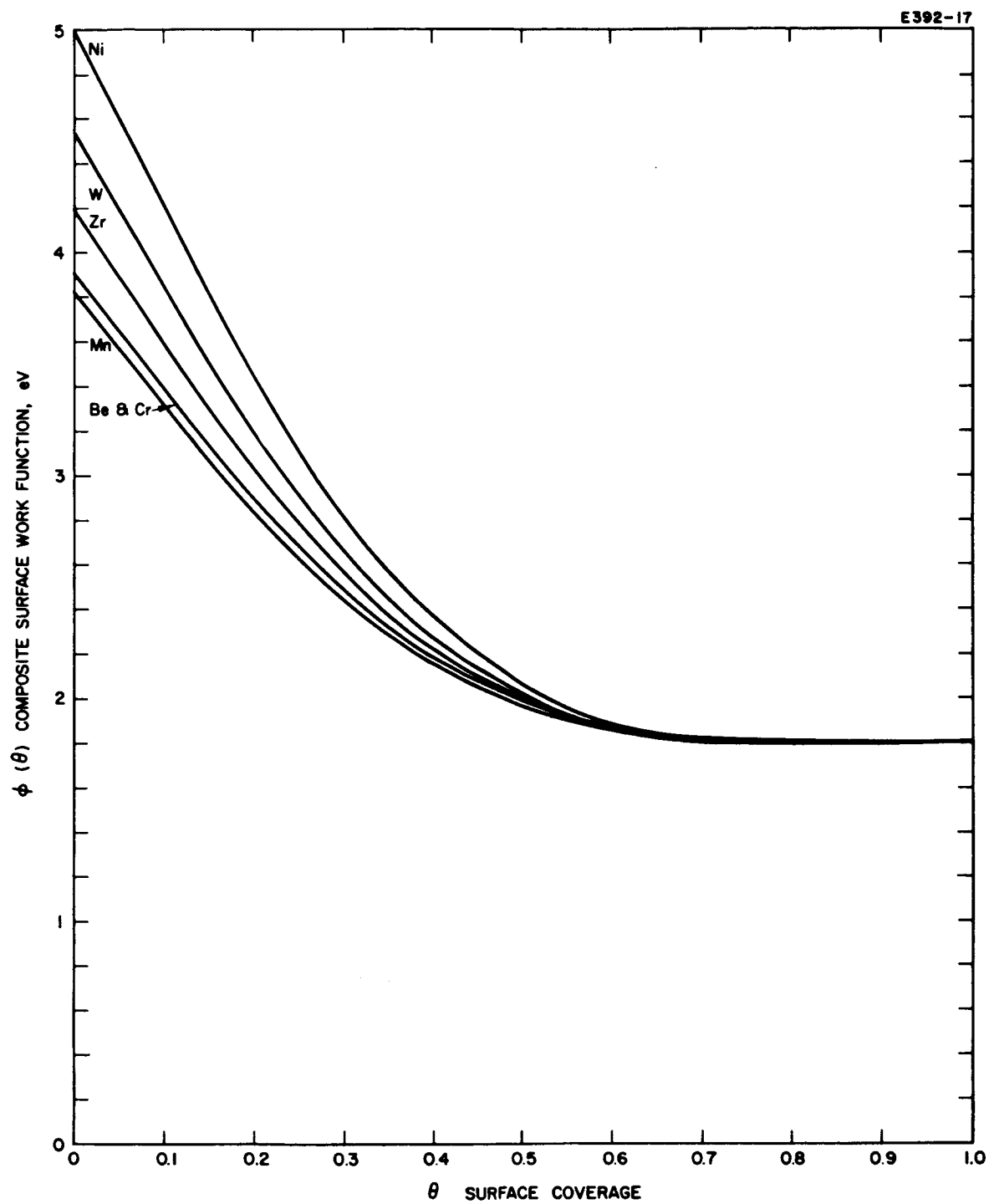Fig. A-9.   Computer calculated composite surface work functions versus surface coverage for cesium on some metals.
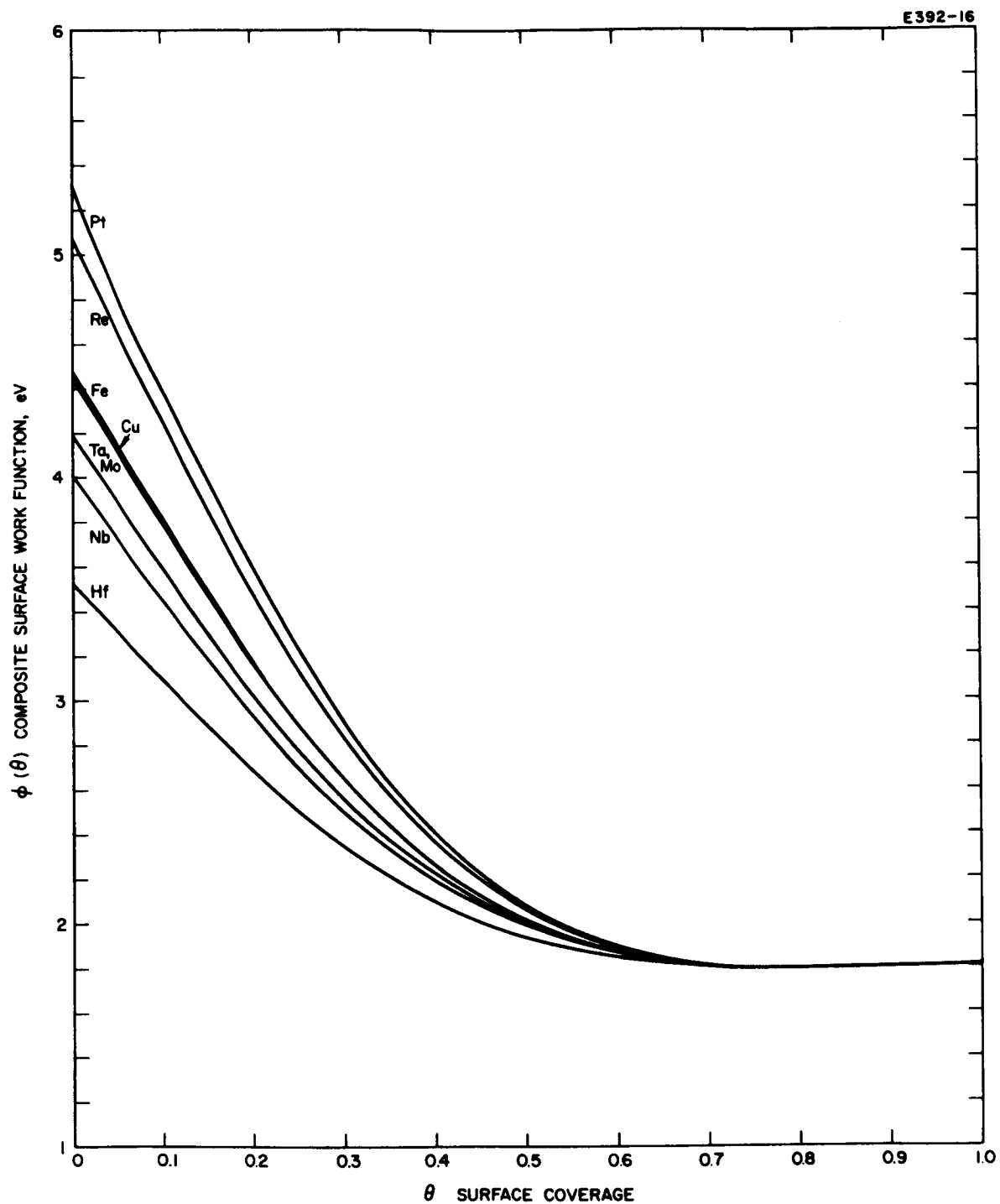
Fig. A-10. Computer calculated composite surface work functions versus surface coverage for cesium on some metals.

The explicit expression for $\lambda_o(\theta)$ is written with the aid of Ref. A-1.

$$\lambda_o(\theta) = \underbrace{F(\theta)\,\phi(\theta)\,[1 + \delta(\theta)]}_{\text{ionic part}} + \underbrace{[H_s(0)H_s(1)]^{1/2}\left[\dfrac{2}{\dfrac{S(0)}{S(1)} + \dfrac{S(1)}{S(0)}}\right]\left[1 - \dfrac{F^2(\theta)}{v^2}\right]^{1/2}}_{\text{covalent part}}$$

$$\tag{A-17}$$

where

$$F(\theta) = \frac{C_5\,[\phi(0) - \phi(1)]\,G(\theta)}{[r(0) + r(1)]\left\{1 + \dfrac{a(1)}{[r(0) + r(1)]^3}\right\}} \tag{A-18}$$

and

$$\delta(\theta) = \frac{F(\theta)}{\phi(\theta)}\left\{\frac{C_6}{[r(0) + r(1)]} - V_i(1)\right\} \tag{A-19}$$

C_5 and C_6 again depend only on the system of units employed.

This expression for $\lambda_o(\theta)$ is derived from a treatment of inter-metallic surface bonding as a combination of ionic and covalent forces based on a surface model which assumes a single polarized species which may be desorbed as either atoms or ions, rather than the existence of two distinct adsorbed species, adatoms and adions, on a conductor, thereby avoiding a number of fundamental shortcomings of the latter model. A number of analogies are drawn from molecular adsorption physics.

$\lambda_o(\theta)$ is written as the superposition of ionic and covalent parts. The ionic part is assumed to result from a coulomb interaction between opposite charges at opposite ends of the bonds, and the covalent part from pairing of valence electrons contributed by the atoms in the bond. A purely ionic bond is characterized by a dipole moment equal to the product of the charges and the internuclear distance. A purely covalent bond has no dipole moment. The ionic part is assumed to result from a

fraction of charge $F(\theta)$ transferred from the adsorbate to the substrate, which determines the ionic character of the bond and which is associated with the surface dipole moment. The ionic part reduces to zero when no dipole moment exists and the bond is purely covalent ($F = 0$) and to the energy required to remove an adsorbed ion from the surface of a conductor when $F = 1$. The fraction of charge F results from a surface double layer of thickness equal to the internuclear distance in which self-depolarization is accounted for.

The covalent contribution to $\lambda_o(\theta)$ is assumed to result from mutual pairing of valence spins of adsorbate and substrate particles. This covalent portion is estimated as the geometric mean of the product of three terms, each of which is the product of a component for the adsorbate and for the substrate. This expression reduces to the proper limiting values when the all-ionic or all-covalent, or the pure adsorbate or the pure substrate extremes are chosen. The first term is the heat of sublimation and is the major contributor. The second is the square of the orbital strength because the greater the eccentricity of the wave function of the valence orbital, the larger the overlapping of the electron clouds of the surface particles, and the stronger the covalent bond. The last term is the valence charge participating in the covalent bond and is the smallest contributor, included to insure that when the bond is purely ionic, the covalent term vanishes. The second and third factors may be interpreted as the angular efficiency of the orbitals and the charge efficiency, respectively. These two terms are consistent in indicating that perfect covalent electron pairing occurs only when the pairing orbitals are identical and have equal charges.

In the calculation of equilibrium surface coverage, mean atom and ion residence times, and composite surface work function, the atomic desorption energy λ_o occurs in a sensitive exponent. Small changes or inaccuracies in λ_o therefore have a large effect on the values of the above quantities. The major contributing term in the expression for λ_o in (A-17) is $[H_s(0) H_s(1)]^{1/2}$. It is therefore very important to use the proper values for the H_s's.

136

The values of $H_s(0)$ and $H_s(1)$ called for in the equation for the atomic desorption energy $\lambda_o(\theta)$ are the desorption energies of a substrate atom from its own surface (lattice) and of an adsorbate atom from its own bulk solid surface. These quantities are not strictly the heats of sublimation ΔH_s of the two species, although they are closely related to them. The heat of sublimation is the energy required to remove an atom from within the surface of a (metal) lattice (i.e., completely bound in the metal lattice). More nearest neighbor and next nearest neighbor bonds must be broken in this case than for desorption from an adsorption site on the surface of the lattice. Therefore, the heat of sublimation per atom is larger than the atomic desorption energy (by a factor of less than two). The actual surface desorption energy varies with the crystal face from which desorption occurs and therefore it depends on the crystal structure of the substrate. An investigation of the nearest-neighbor and next-nearest-neighbor bonding for the various crystal faces of the three principal crystal structures encountered in the work to which this problem is being applied (body-centered cubic, face-centered cubic, and hexagonal close-packed) has been made in order to solve this problem.

Assuming that the interactions between neighboring atoms in a crystal can be described as occurring between pairs of nearest neighbors with a bond energy E_1, and between next nearest neighbors, with a bond energy E_2, the desorption energies can be written for the various crystal faces of the various crystal types from knowledge of the crystal structure. These can then be related to the expression for an atom removed from within the crystal structure (i.e., the experimentally measured sublimation energy). Ratios of these can then be taken to obtain the desired result. As an example, Table A-I gives the nearest-neighbor plus next-nearest-neighbor bonding sums for the three principal planes of the three primary crystal structures, the ratios of the strengths of the next-nearest-neighbor bonds to the nearest-neighbor bonds E_2/E_1, the corresponding total sublimation energy expression, and the ratio of surface desorption energy to sublimation energy.

TABLE A-I

Influence of Crystallography on Sublimation Energies

Crystal Structure Type	$\Delta H_s + \frac{kT}{2}$	H_s (100) or (001)	H_s (110) or (010)	H_s (111) or (110)	$\dfrac{E_2}{E_1}$	Average Ratio of $H_s / \Delta H_s$
Face-centered cubic	$6E_1+3E_2$	$4E_1+1E_2$	$5E_1+2E_2$	$3E_1+3E_2$	1/10	0.667
Body-centered cubic	$4E_1+3E_2$	$4E_1+1E_2$	$2E_1+2E_2$	$4E_1+3E_2$	1/2	0.788
Hexagonal close packed	$6E_1+3E_2$	$3E_1+3E_2$	$4E_1+4E_2$	$5E_1+2E_2$	1/10	0.682

A further correction is required in the calculation of H_s to account for the temperature dependence of ΔH_s. The sublimation energy decreases with increasing surface temperature as

$$\Delta H_s(T) = \Delta H_s(0) - \frac{kT}{2} \qquad \text{(A-20)}$$

or

$$\Delta H_s(T_x) = \Delta H_s(T_m) + \frac{k}{2}(T_m - T_x) \qquad \text{(A-21)}$$

where $\Delta H_s(T_m)$ is the sublimation energy measured (or quoted) at T_m, and T_x is the temperature at which ΔH_s is desired. Values for ΔH_s are often quoted at 25C. Therefore for a substrate surface temperature of 1400K, the correction factor when ΔH_s is quoted at 25C, is 0.047 eV.

The values of H_s used in the expression for $\lambda_o(\theta)$ are then obtained from the expression

$$H_s(T_x) = \left(\frac{H_s}{\Delta H_s}\right) \left[\Delta H_s(T_m) + \frac{k}{2}(T_m - T_x)\right] \qquad \text{(A-22)}$$

where the ratio $(H_s / \Delta H_s)$ is calculated for the appropriate crystal structure type at T_x by the technique described above and illustrated in Table A-I.

Calculated curves of $\lambda_o(\theta)$ and $\lambda_+(\theta)$ as a function of θ from zero to unity are displayed in Figs. A-11 through A-14 for cesium on 14 substrates at 1400K and in Figs. A-15 and A-16 for 16 metals on a tungsten substrate at 1400K. The corrections for crystallography as well as temperature have been made where believed appropriate. In addition, the values of $\lambda_o(0)$, $\lambda_o(1)$, $\lambda_+(0)$, and $\lambda_+(1)$ for cesium on 41 substrates are included as Table A-II.

Fig. A-11. Computer calculated atom desorption energies versus surface coverage for cesium on some metals.

Fig. A-12. Computer calculated atom desorption energies versus sur-
face coverage for cesium on some metals.

Fig. A-13. Computer calculated ion desorption energies versus surface coverage for cesium on some metals.
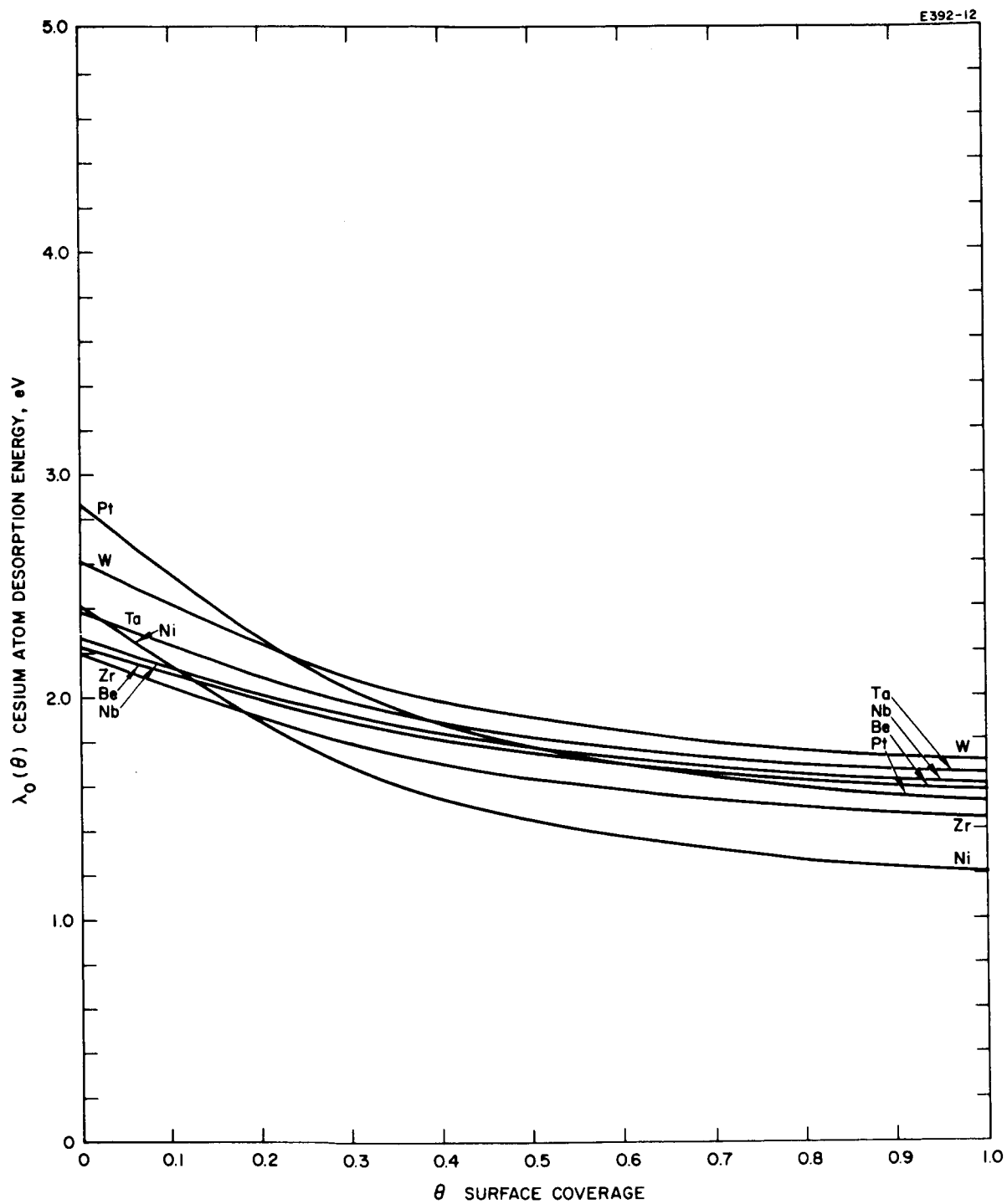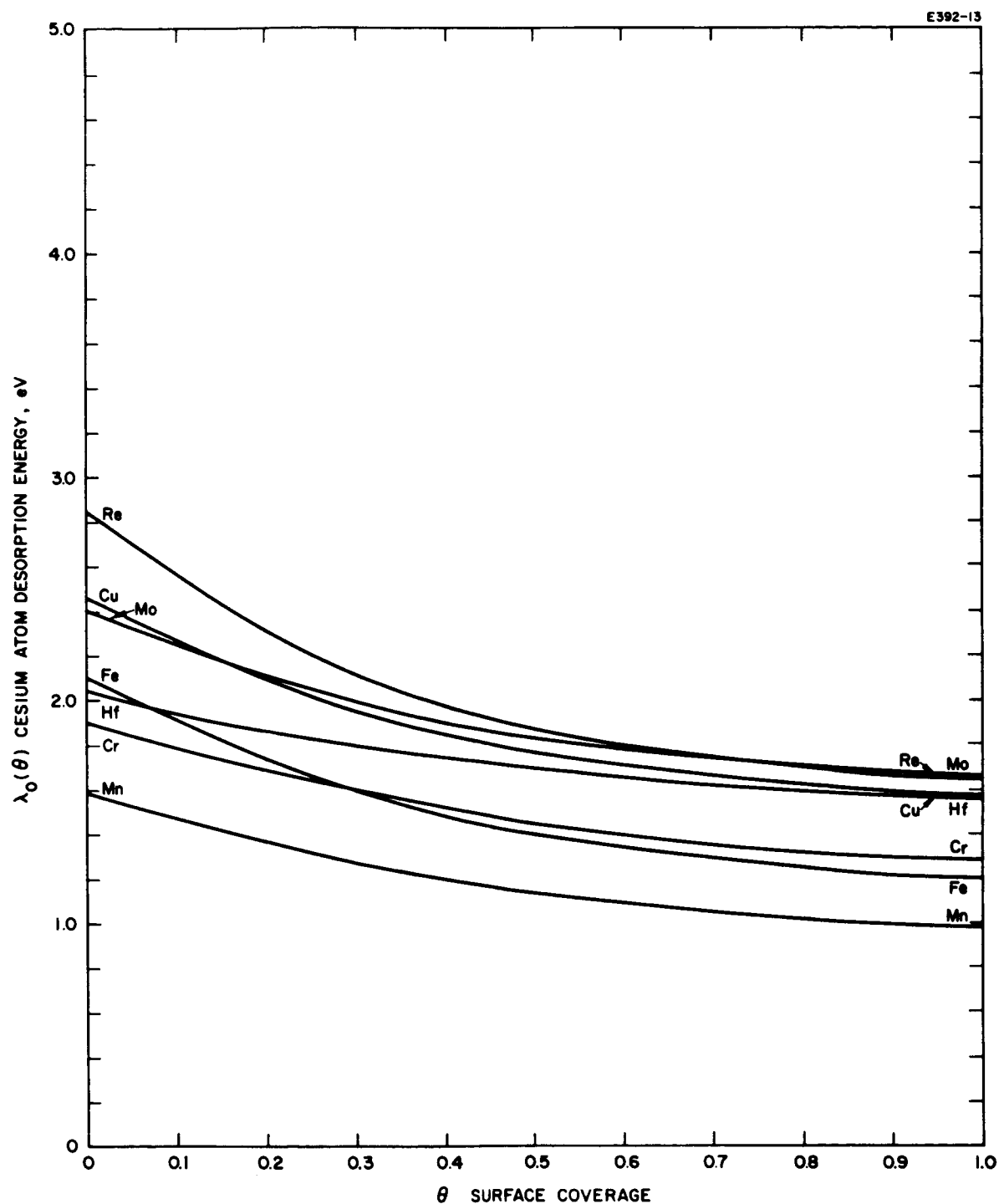
Fig. A-14. Computer calculated ion desorption energies versus surface coverage for cesium on some metals.
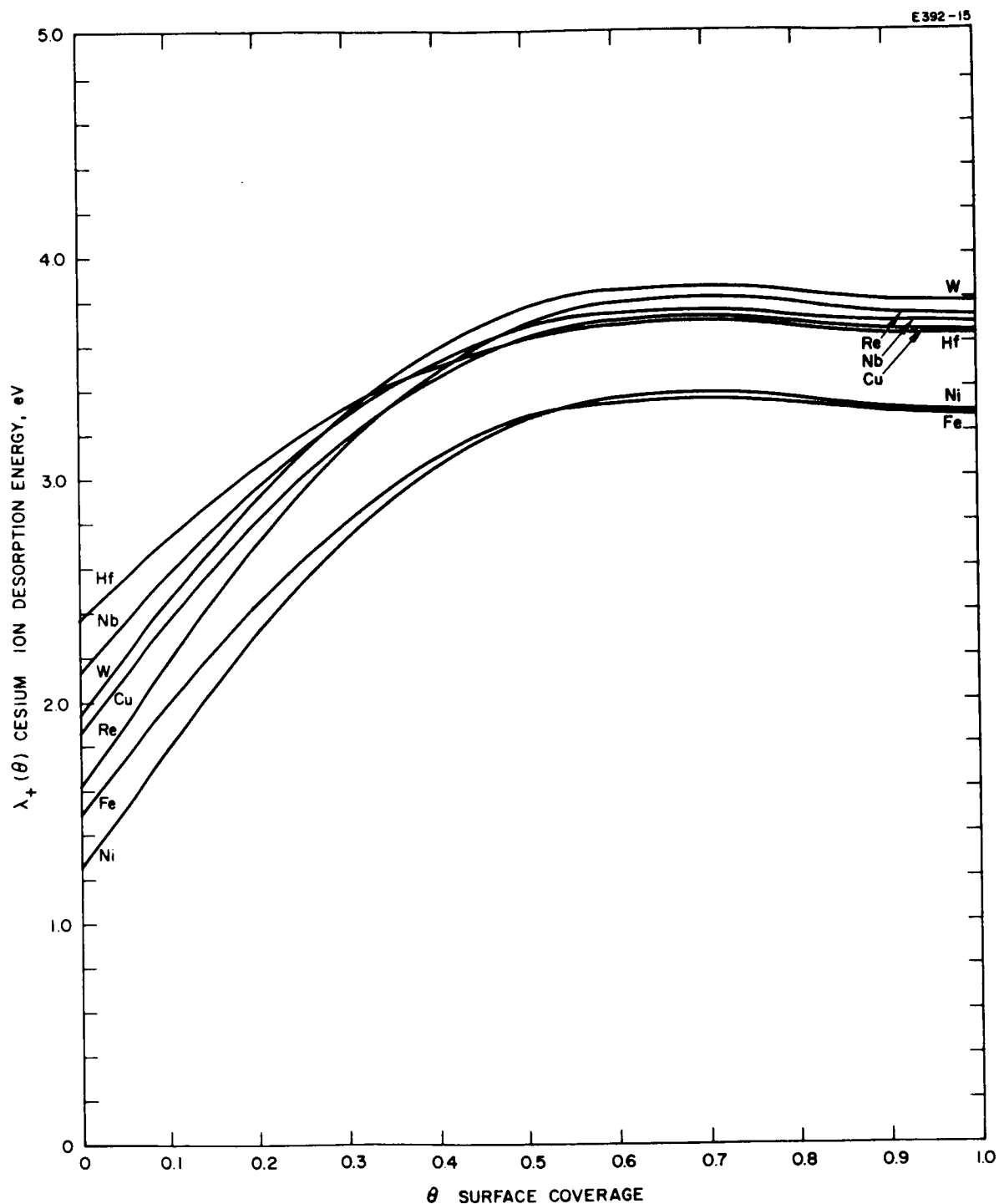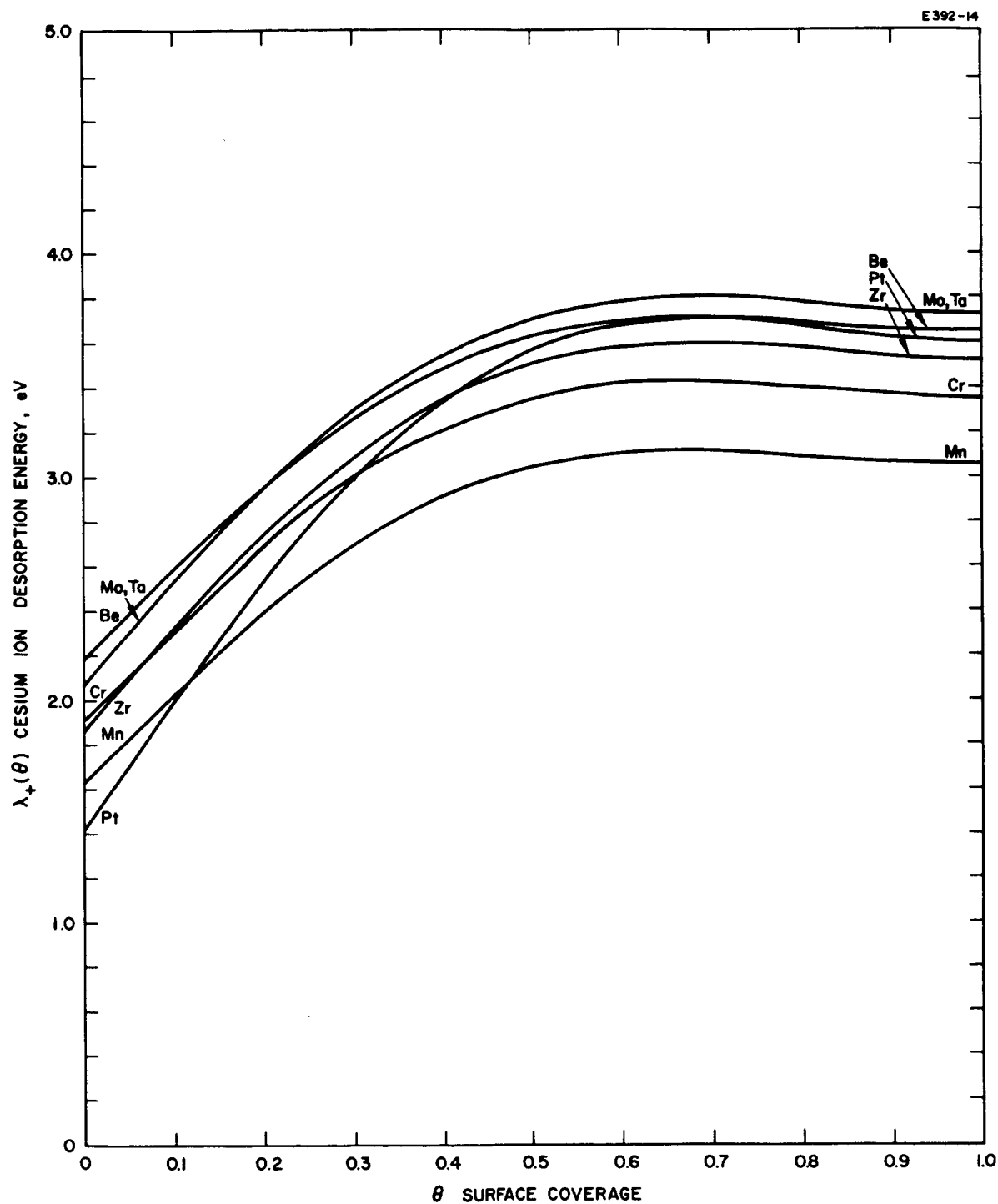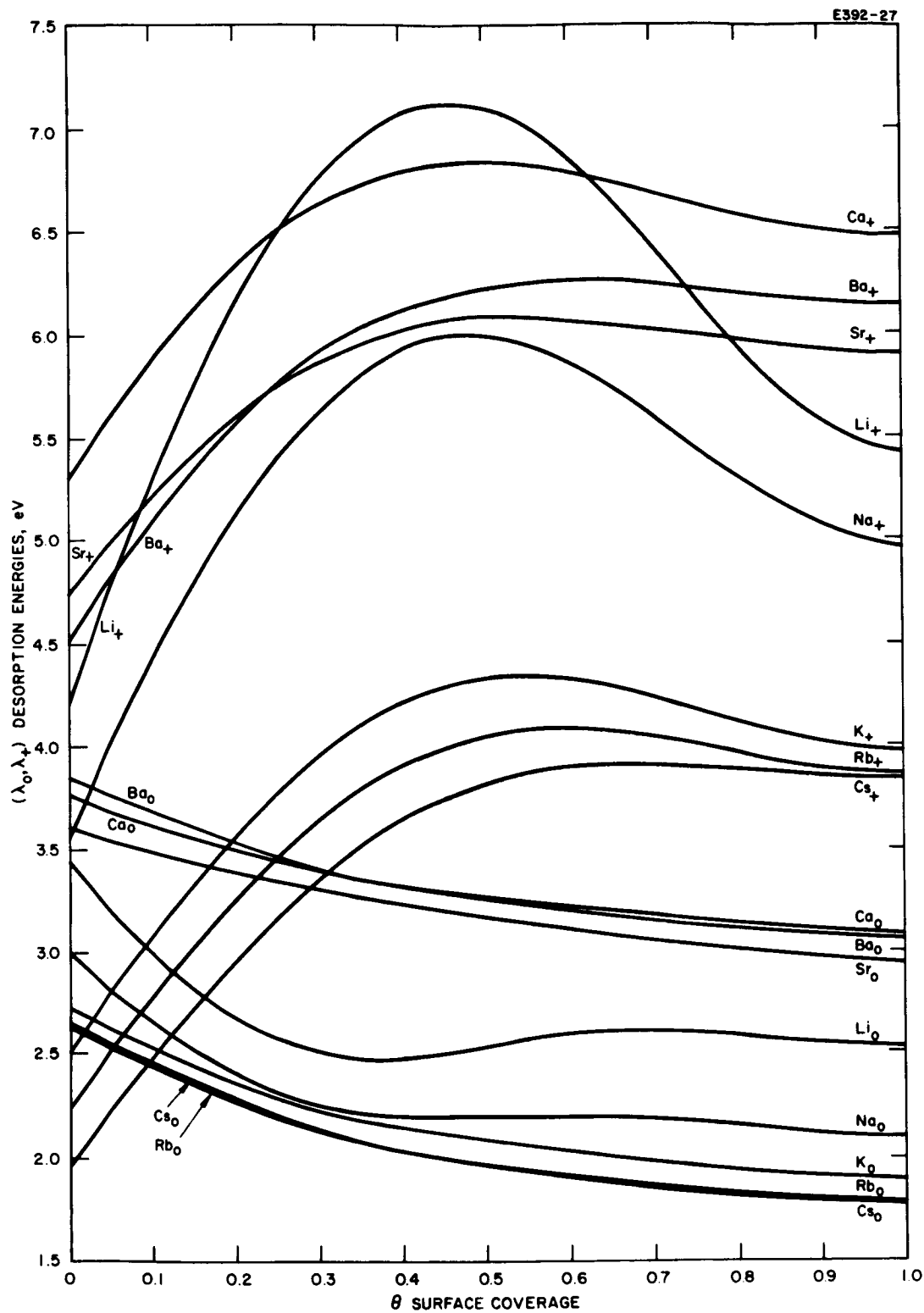
Fig. A-15. Computer calculated atom and ion desorption energies versus surface coverage for some metals on tungsten.
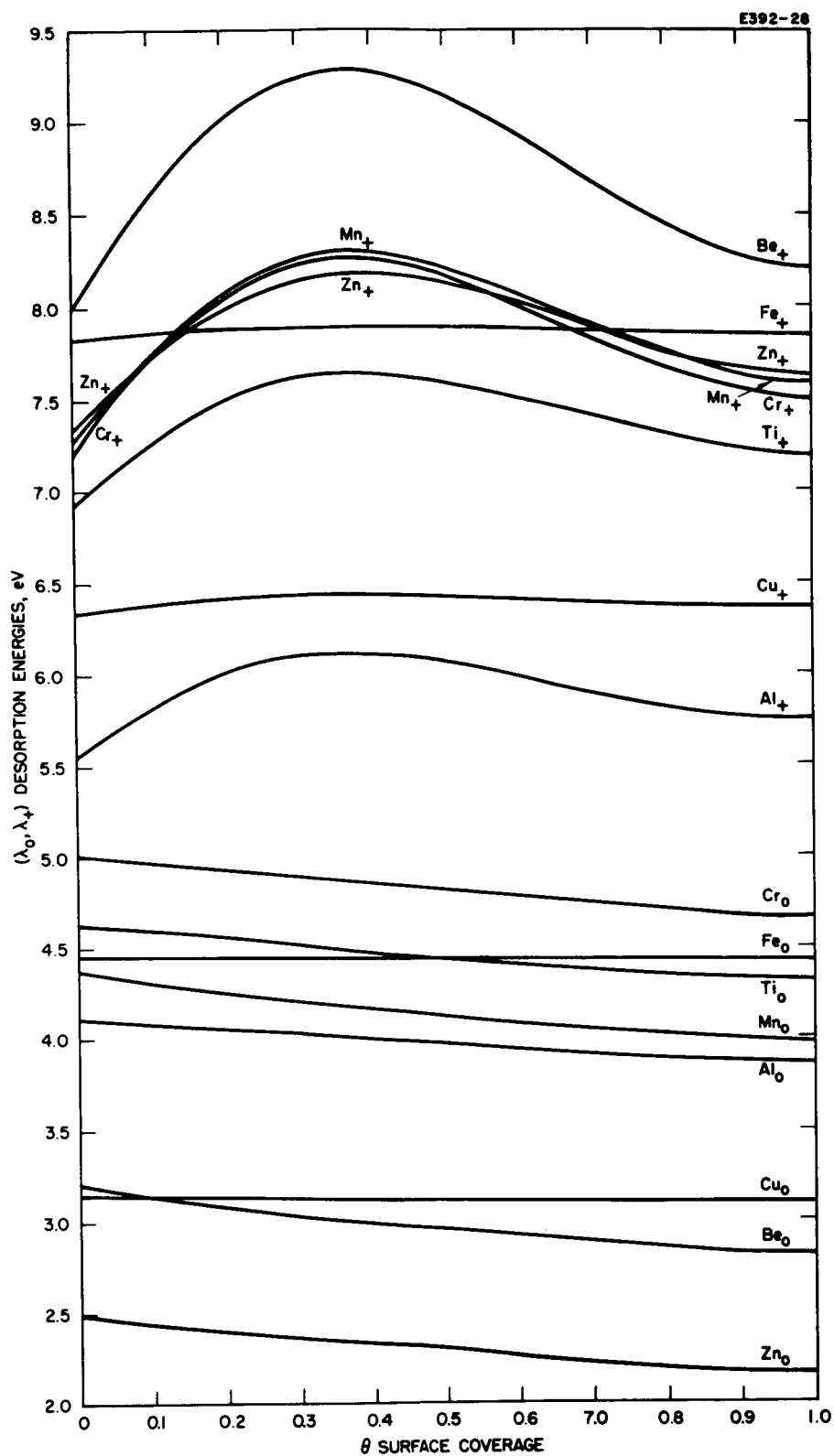
144

Fig. A-16. Computer calculated atom and ion desorption energies versus surface coverage for some metals on tungsten.

TABLE A-II

Atom and Ion Desorption Energies for Cesium on Various Substrates

Substrate	$\lambda_o(0)$, eV	$\lambda_o(1)$, eV	$\lambda_+(0)$, eV	$\lambda_+(1)$, eV	Substrate	$\lambda_o(0)$, eV	$\lambda_o(1)$, eV	$\lambda_+(0)$, eV	$\lambda_+(1)$, eV
Beryllium	2.22	1.58	2.18	3.65	Ruthenium	2.48	1.58	1.84	3.65
Boron	2.84	1.94	2.22	4.01	Rhodium	2.56	1.52	1.64	3.59
Carbon	2.93	1.97	2.21	4.04	Palladium	2.32	1.17	1.22	3.24
Magnesium	1.56	1.03	1.76	3.10	Silver	2.30	1.49	1.83	3.56
Aluminum	2.25	1.56	2.05	3.63	Cadmium	1.58	0.89	1.39	2.96
Silicon	2.27	1.54	2.00	3.61	Indium	1.96	1.23	1.64	3.30
Scandium	1.96	1.48	2.24	3.55	Tin	1.94	1.11	1.44	3.18
Titanium	1.91	1.28	1.84	3.35	Lead	1.76	1.04	1.49	3.11
Vanadium	2.05	1.33	1.81	3.40	Lanthanum	1.99	1.63	2.57	3.70
Chromium	1.91	1.28	1.89	3.35	Hafnium	2.02	1.56	2.37	3.63
Manganese	1.58	0.98	1.63	3.05	Tantalum	2.38	1.65	2.07	3.72
Iron	2.10	1.20	1.50	3.27	Tungsten	2.60	1.71	1.94	3.78
Cobalt	2.07	1.21	1.55	3.28	Rhenium	2.84	1.64	1.62	3.71
Nickel	2.40	1.21	1.25	3.28	Osmium	2.44	1.53	1.77	3.60
Copper	2.45	1.57	1.87	3.64	Iridium	2.80	1.48	1.38	3.55
Zinc	1.59	0.96	1.57	3.03	Platinum	2.86	1.53	1.42	3.60
Yttrium	2.14	1.65	2.37	3.72	Gold	2.31	1.50	1.84	3.57
Zirconium	2.19	1.46	1.86	3.53	Mercury	1.59	0.67	0.93	2.74
Niobium	2.26	1.61	2.13	3.68	Lead	1.79	0.89	1.14	2.96
Molybdenum	2.40	1.66	2.08	3.73	Thorium	1.74	1.36	2.27	3.43
Technetium	2.48	1.64	1.96	3.71					

ION CRITICAL TEMPERATURES

Because the measurement of critical temperatures for saturated cesium ion emission from a variety of metal substrates is one of the major goals of this contract, a theoretical investigation of the subject is in order so that the experimental data may be related to a satisfactory theory. A theoretical expression for all surfaces relating T_c to J_+ or μ which gives good agreement with the experimental data for cesium on solid and porous tungsten is developed below. Combination of the expression with a form of the Saha-Langmuir equation shows the theoretical relationship between β_c and J_+ or μ which is in good agreement with experimental data.

The ionization efficiency and ion current density are shown to be slightly dependent on the applied electric field. The expressions originally expressed are simplified forms of more complex ones (e.g., involving the explicit forms for patchy surfaces). For this application, the range of E is taken as 10^4 to 10^5 V/cm. θ is not assumed to be zero but rather a small value θ_c, the value of the coverage at the critical point. The explicit dependences of the desorption energies on θ are used. The analysis is made specifically for cesium but can be extended to other adsorbates.

$$J_+ = e\mu\beta \tag{A-23}$$

$$\beta = \frac{\nu_+}{\mu} \tag{A-24}$$

The ratio of desorbing ion flux to the total incident flux

$$\nu_+ = \frac{\sigma}{\tau_+} = \left(\frac{\theta\,\sigma\,(1)}{2}\right)\left(\frac{kT}{h}\right)\left[1 - e^{-\left(\frac{h\omega}{kT}\right)}\right]e^{\left(\frac{\Delta S}{k}\right)}e^{-\left[\frac{\lambda_+(\theta) - e\sqrt{eE}}{kT}\right]} \tag{A-25}$$
$$\text{(for small }\theta)$$

where τ_+ is discussed in a previous section.

For the critical temperature condition, $T = T_c$, $\beta = \beta_c$, $\theta = \theta_c$ and E is greater than the magnitude required to extract the saturated ion current density. Because θ is small (less than 0.05) in the critical region, $\exp(\Delta S/k)$ may be replaced by unity. Thus

$$\beta_c = \left(\frac{\theta_c \, \sigma(1)}{2\mu}\right)\left(\frac{kT_c}{h}\right)\left[1 - e^{-\left(\frac{h\omega}{kT_c}\right)}\right] e^{-\left[\frac{\lambda_+(\theta_c) - e\sqrt{eE}}{kT_c}\right]}$$

(A-26)

and

$$J_+ = \left(\frac{e\theta_c \, \sigma(1)}{2}\right)\left(\frac{kT_c}{h}\right)\left[1 - e^{-\left(\frac{h\omega}{kT}\right)}\right] e^{-\left[\frac{\lambda_+(\theta_c) - e\sqrt{eE}}{kT_c}\right]} .$$

(A-27)

It will be seen that β (and J_+) vary with certain parameters above the critical point.

The [ ] term, the statistical mechanics vibration partition function, can have two extreme values, 1 and $(h\omega/kT_c)$; for the conditions described, and as shown experimentally by the measurement of Scheer and Fine[A-4] for cesium, it has the value $(h\omega/kT_c)$ where ω is the vibrational frequency of the adsorbate which is 0.88×10^{12} sec^{-1} for cesium. Therefore, the two adjacent pre-exponential terms in (A-26) and (A-27) become simply ω, and

$$\beta_c = \left(\frac{\theta_c \, \sigma(1) \, \omega}{2\mu}\right) e^{-\left[\frac{\lambda_+(\theta_c) - e\sqrt{eE}}{kT_c}\right]}$$

(A-28)

$$J_+ = \left(\frac{e\theta_c \, \sigma(1)\omega}{2} \right) e^{-\left[\frac{\lambda_+(\theta_c) - e\sqrt{eE}}{kT_c} \right]} . \qquad (A-29)$$

For saturated ion current density extraction, E must be greater than the space-charge-limited — emission-limited value. For $J_+ > \sim 10^{-4}$ A/cm^2, the term $e\sqrt{eE}$ is not negligible. For $E = 1.3 \times 10^4$ and 1.0×10^5 V/cm, the corresponding values of $e\sqrt{eE}$ are 0.04 and 0.12 eV.

Equation (A-29) can be written

$$\ln J_+ = \ln \left(\frac{e\theta_c \, \sigma(1)\omega}{2} \right) - \left[\frac{\lambda_+(\theta_c) - e\sqrt{eE}}{kT_c} \right] \qquad (A-30)$$

or

$$\ln J_+ = A - \frac{B}{T_c} . \qquad (A-31)$$

An empirical value for θ_c is obtained by setting the value of A equal to an experimentally determined intercept and solving for θ_c. The data of Zandberg, et al.,[A-5] for J_+ versus T_c for cesium on solid tungsten measured over five orders of magnitude from $J_+ = 10^{-7}$ to 10^{-2} A/cm^2 are shown in Fig. A-17 together with those of Stavisskii and Lebedev[A-6] for porous tungsten measured over a smaller range of higher J_+, and those of Taylor and Langmuir[A-7] measured over a small range of lower J_+. The slope and intercept of the curve through the data of Ref. A-5 are 2.47×10^4 K and 12.52, respectively, as shown in Fig. A-17. The value of E used in Ref. A-5 was 1.3×10^4 V/cm; this gives the theoretical value of the slope from (A-28 of
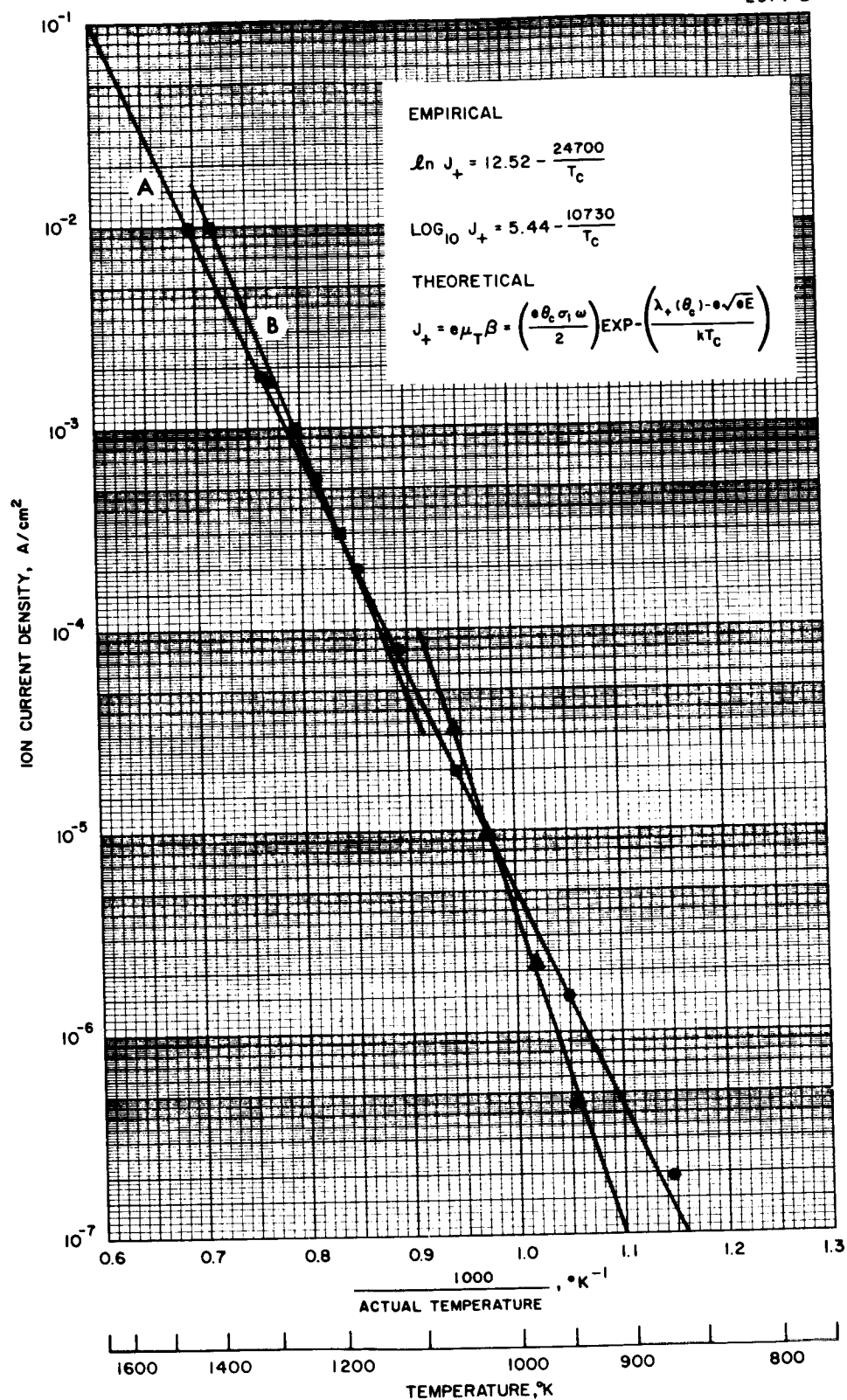
Fig. A-17. Experimental data for cesium ion current density versus critical temperature on tungsten.

2.45 x 10^{4}K, which is in excellent agreement with the experimental value 2.47 x 10^{4}K. The experimental value of the intercept when equated to A in (A-30) and (A-31) and solved for θ_c gives 0.026, which is probably an upper limit from other considerations. It seems reasonable to state that (A-27) and (A-30) are valid expressions and that θ_c for the cesium-tungsten system is equal to or less than 0.026.

In Fig. A-18, the straight lines of Fig. A-17 are replotted as $\ell n J_+$ versus T_c. Two theoretical curves are plotted showing the effect of electric field. One value of E is chosen as 1 x 10^5 V/cm to correspond to the thrustor electrode conditions. It is significant to note that increasing the electric field by an order of magnitude at a surface where cesium may ionize reduces the critical temperature by approximately 60C. Furthermore, it is significant to note that the theoretical straight lines ($\ell n\, J_+$ versus $1/T_c$) are strictly obtainable experimentally only by using a constant electric field. If the value of applied voltage corresponding to the emission-limited knee is used for each value of J_+, a curve will result which is not a straight line when plotted as in Fig. A-17. Such a curve cuts across theoretical curves for constant E as J_+ increases.

We can write a theoretical expression

$$\beta_c = \left(\frac{\theta_c \sigma(1)\omega}{2\mu}\right) e^{-\left[\frac{\lambda_+(\theta_c) - e\sqrt{eE}}{kT_c}\right]}$$

(A-32)

which we know is valid for cesium or tungsten, and may be valid for other adatom-substrate combinations. For other combinations, an appropriate value of $\lambda_+(\theta_c)$ must be calculated or measured, the appropriate value of ω for the adsorbate must be substituted, and the value of $\sigma(1)$ for the particular adsorbate-substrate combination must be used, resulting in different values of A for each system. For cesium on other substrates, the value of $\lambda_+(\theta_c)$ may be obtained from the curves presented earlier in this Appendix. The value of

E374-3

THEORETICAL CURVE FOR
$E = 1 \times 10^5$ V/cm

$\ln J_+ = 12.52 - \dfrac{23550}{T_c}$

$\text{LOG}_{10} J_+ = 5.44 - \dfrac{10220}{T_c}$

EXPERIMENTAL DATA FROM
ZANDBERG ET AL AND
THEORETICAL CURVE FOR
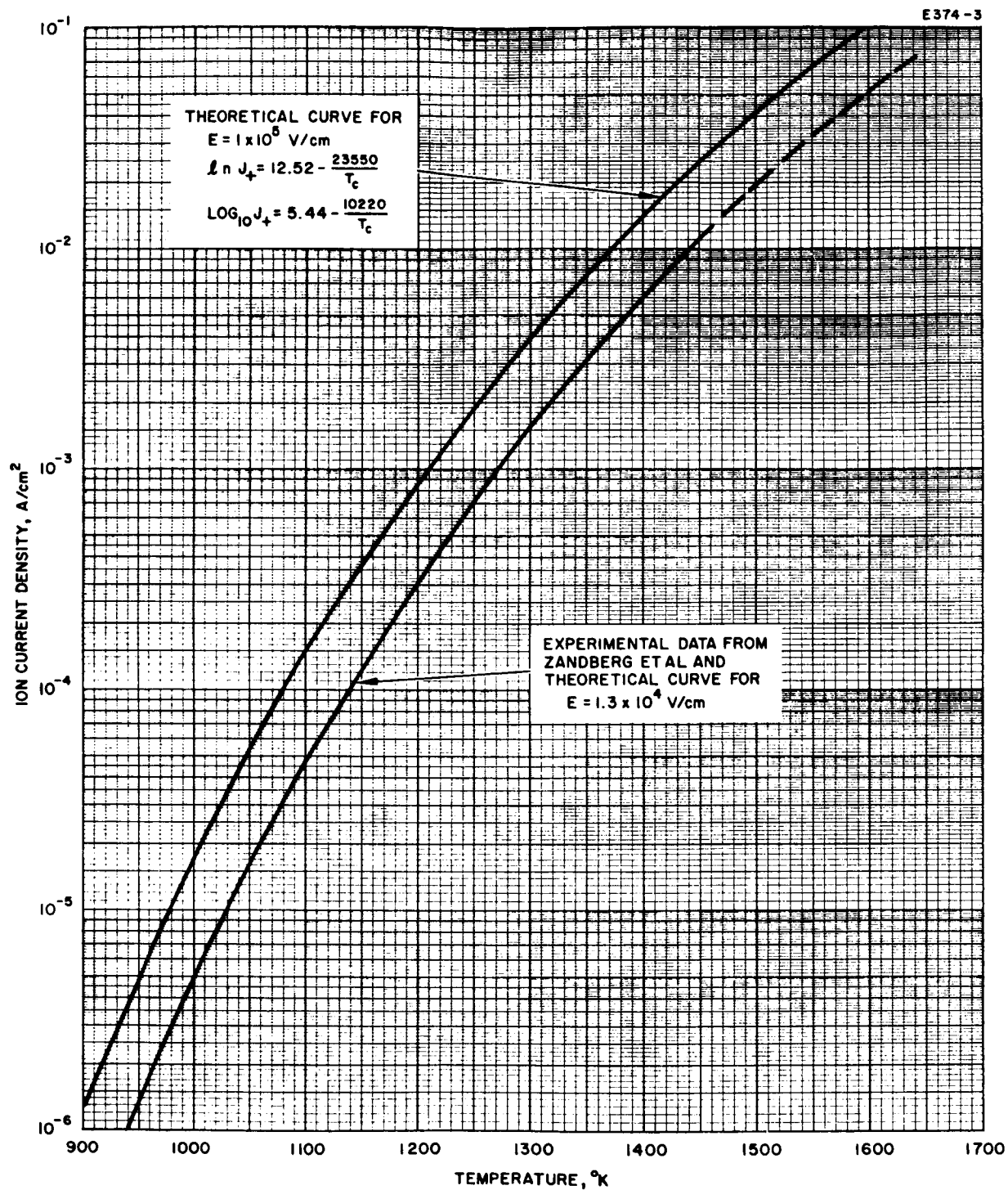$E = 1.3 \times 10^4$ V/cm

Fig. A-18. Cesium ion critical temperature curves showing influence of electric field.

152

$\sigma(1)$ depends on the crystallographic structure of both cesium and the substrate. This involves matching structures, lattice constants, and ionic diameters. θ_c may conceivably differ for other systems, but the difference will certainly be only slight.

It is significant in (A-32) that explicit relationships are given among the three quantities β_c, μ, and T_c. For β approaching unity, μ can be replaced approximately by J_+/e and it is seen that $\beta \propto 1/J_+$ in agreement with the experimental evidence[A-8, A-9] (low neutral fraction). As β decreases (neutral fraction increases), the dependence accelerates, in agreement with experimental data. β is seen to increase with T above T_c in agreement with experiments. β is seen to increase with E above the emission-limited knee in agreement with experiment.

NEUTRAL FRACTION

By introducing a simplified form of the Saha-Langmuir equation at the critical point

$$\beta_c = \left\{ 1 + 2 e^{\left[\dfrac{V_i - \phi(\theta_c) - e\sqrt{eE}}{kT_c} \right]} \right\}^{-1} \tag{A-33}$$

and combination of (A-32) and (A-33), T_c can be eliminated and an expression derived which relates β_c and μ:

$$\beta_c = \left(\frac{\theta_c \sigma(1)\omega}{2\mu}\right) \left(\frac{\beta_c^{-1} - 1}{2}\right)^{\left[\frac{\lambda_+(\theta_c) - e\sqrt{eE}}{\phi(\theta_c) + e\sqrt{eE} - V_i}\right]}.$$

(A-34)

β_c cannot be conveniently solved for, but we can solve for μ (and J_+) in terms of β_c, plot the expression, and obtain graphically β_c as a function of μ.

$$\mu = \left(\frac{\theta_c \sigma(1)\omega}{2\beta_c}\right) \left(\frac{\beta_c^{-1} - 1}{2}\right)^{\left[\frac{\lambda_+(\theta_c) - e\sqrt{eE}}{\phi(\theta_c) + e\sqrt{eE} - V_i}\right]}.$$ (A-35)

Substituting $J_+ \equiv e\beta_c\mu$ and $\beta_c = 1 - NF$,

$$J_+ = \left(\frac{e\theta_c \sigma(1)\omega}{2}\right) \left(\frac{NF}{2(1-NF)}\right)^{\left[\frac{\lambda_+(\theta_c) - e\sqrt{eE}}{\phi(\theta_c) + e\sqrt{eE} - V_i}\right]}.$$

(A-36)

Equation (A-36) gives the relationship between ion current density and neutral fraction. Exact critical temperature curves cannot be calculated unless the proper values of $\lambda_+(\theta_c)$, θ_c, ω, and $\sigma(1)$ are known. The analytical calculations of this Appendix can be used to obtain $\lambda_+(\theta_c)$ if θ_c is assumed to be 0.026 for cesium on all substrates. ω is constant for cesium on all substrates. $\sigma(1)$ can vary among substrates and will influence the location of the critical temperature curve, although its slope is determined solely by the value of $\lambda_+(\theta_c)$.

REFERENCES

A-1.　J. D. Levine and E. P. Gyftopoulos, Surface Science $\underline{1}$, 171 (1964).

A-2.　E. P. Gyftopoulos and J. D. Levine, J. Appl. Phys. $\underline{33}$, 67 (1962).

A-3.　J. D. Levine, private communication.

A-4.　M. D. Scheer and J. Fine, J. Chem. Phys. $\underline{37}$, 107 (1962).

A-5.　E. Ya. Zandberg, V. I. Paleev, and A. Ya. Tontegode, Soviet Phys. — Tech. Phys. $\underline{7}$, 147 (1962).

A-6.　Yu. Ya. Stavisskii and S. Ya. Lebedev, Soviet Phys. — Tech. Phys. $\underline{5}$, 1158 (1962).

A-7.　J. B. Taylor and I. Langmuir, Phys. Rev. $\underline{44}$, 423 (1933).

A-8.　R. G. Wilson, G. D. Seele, and J. F. Hon, AIAA Paper No. 63017 (1963).

A-9.　O. K. Husmann, AIAA Paper No. 63019 (1963).

DISTRIBUTION LIST

Recipient	Address
Spacecraft Technology Procurement Section (1)	NASA-Lewis Research Center 21000 Brookpark Road Cleveland, Ohio 44135
Technology Utilization Office Attn: Mr. John Weber (1)	NASA-Lewis Research Center 21000 Brookpark Road Cleveland, Ohio 44135
Office of Reliability and Quality Assurance (1)	NASA-Lewis Research Center 21000 Brookpark Road Cleveland, Ohio 44135
Headquarters Attn: RNT/James Lazar (2)	National Aeronautics and Space Administration FOB-10B 600 Independence Avenue, S.W. Washington, D.C. 20546
Commander Attn: AFAPL (APIE) Robert Supp (1)	Aeronautical Systems Division Wright-Patterson Air Force Base, Ohio
Attn: J. J. Paulson (1)	Jet Propulsion Laboratory 4800 Oak Grove Drive Pasadena, California
Technical Library (1)	NASA-Langley Research Center Langley Field, Virginia
Attn: Dr. A. T. Forrester (1)	Electro-Optical Systems, Inc. 125 North Vinedo Avenue Pasadena, California
New Products Research Attn: Dr. Park French (1)	Bunker-Ramo Wooldridge, Inc. 7209 Platt Avenue Canoga Park, California
Attn: Dr. D. Langmuir (2)	Space Technology Laboratories 8433 Fallbrook Avenue Canoga Park, California
Attn: W. Rayle (1)	NASA-Lewis Research Center 21000 Brookpark Road Cleveland, Ohio 44135

Recipient	Address
Headquarters, USAF Attn: Dr. M. Slawsky (2)	Air Force Office of Scientific Research Washington 25, D.C.
Research Department Attn: Dr. R. G. Meyerand, Jr. (1)	United Aircraft Corporation East Hartford, Connecticut
Attn: Dr. F. Charbonnier (2)	Field Emission Corporation McMinnville, Oregon
Attn: Dr. G. B. Shook (1)	Lockheed Aircraft Corporation Missiles and Space Company Palo Alto, California
Thermonuclear Project Attn: Dr. A. Weinberg (1)	Oak Ridge National Laboratory Oak Ridge, Tennessee
Hansen Microwave Laboratory Attn: Dr. G. S. Kino (1)	Stanford University Stanford, California
General Engineering Laboratories Attn: Dr. Lynn Stauffer (1)	General Electric Company Schenectady, New York
Nucleonics Division Attn: Mr. J. S. Luce	Aerojet-General San Ramon, California
Attn: Dr. E. Stuhlinger (M-RP-DIR) (1)	Marshall Space Flight Center Huntsville, Alabama
Attn: J. W. Meusteller (1)	MSA Research Corporation Caliery, Pennsylvania
Attn: Technical Library Documents Group (1)	Aerospace Corporation P.O. Box 95085 Los Angeles 45, California
Office of Technical Information Extension (1)	U.S. Atomic Energy Commission P. O. Box 62 Oak Ridge, Tennessee
Attn: R. W. Diehl (1)	National Research Corporation 70 Memorial Drive Cambridge, Massachusetts 02142

Recipient	Address
Spacecraft Technology Division Attn: J. H. Childs (2) D. L. Lockwood (2) Y. E. Strausser (5)	NASA-Lewis Research Center 21000 Brookpark Road Cleveland, Ohio 44135
AFPR Attn: RWRAAC-2-D. Fisher (1) RWRAPS-9-Mr. Weldon (1)	Hughes Aircraft Company Florence Avenue and Teale Street Culver City, California
Electromagnetic Propulsion Division Attn: W. Moeckel (1) E. Richley (1)	NASA-Lewis Research Center 21000 Brookpark Road Cleveland, Ohio 44135
Electron Tube Division Attn: Dr. Rajindar Wadhwa (1)	Litton Industries 960 Industrial Road San Carlos, California
Attn: Capt. C. F. Ellis/WLPC (1) AFWL	Kirtland Air Force Base New Mexico
Electrical Propulsion Laboratory Attn: Mr. H. W. Szymanowski, Mgr. (1)	Westinghouse Astronuclear Laboratories Pittsburgh 35, Pennsylvania
Attn: NASA Representative RQT-2448 (6)	NASA-Scientific and Technical Information Facility Box 5700 Bethesda 14, Maryland
Library (2)	NASA-Lewis Research Center 21000 Brookpark Road Cleveland, Ohio 44135
Reports Control Office (1)	NASA-Lewis Research Center 21000 Brookpark Road Cleveland, Ohio 44135
David Sarnoff Research Center Attn: K. G. Hernqvist (1)	Radio Corporation of America Princeton, New Jersey
Attn: H. E. Nastelin (1)	NASA-Lewis Research Center 21000 Brookpark Road Cleveland, Ohio 44135
Prof. Laurence Shaffer Department of Physics (1)	Hiram College Hiram, Ohio